The differential shape of the Z to ee cross-section as a function of Z rapidity

A DISSERTATION
SUBMITTED TO THE FACULTY OF THE GRADUATE SCHOOL
OF THE UNIVERSITY OF MINNESOTA
BY

Jason Anthony Haupt

IN PARTIAL FULFILLMENT OF THE REQUIREMENTS
FOR THE DEGREE OF
Doctor of Philosophy

May, 2011

Acknowledgements

I would like to acknowledge all those who have helped and push me towards my personal goals throughout the years. To all my family members, friend, colleagues and teachers, thank you.

Chronologically I would like to thank Mr. Faber, who first replied to my detailed inquiries about anatomy and physiology with "I do not know, ask a physicist!" That began my desire to enter the fundamental sciences to be one of those who knew the answers to those detailed questions. I am proud to say, I have gone far beyond trying to figure out why red blood in the body looks blue in the veins. Thank you Mr. Keith for making calculus seem as simple as addition—although I still have far more trouble with addition and subtraction than calculus.

Thank you to the men of the American Legion in Bloomington Minnesota for awarding me a scholarship and thereby giving me that extra chance to succeed in college. Additionally to the people of the State of Minnesota for their generous grants during my undergraduate studies.

A special mention to my classmates of the physics undergraduate program at the University of Minnesota School of Physics and Astronomy. All those hours of working on the endless problem sets really provided me with perspective on how to succeed. Specifically to Nicholas Moody for the real in-depth discussion on all topics, physics and otherwise, and to Kristopher Borgart. With the motivation of Kristopher, I learned to work on problem sets the day of the assignment—a skill that has transfered well to many of the accomplishments I have since made.

The first two years of graduate school would not have gone well without the insight and dedication of the other entry-level graduate students. Mostly, to my first year office mates and to those who would discuss the details of supersymmetry or quantum field

theory. Scott, Hannes, Aaron, Matt and Doug we have all emerged from the basement dungeon which was our first office.

Working on the CMS experiment has been rewarding and challenging at the same time. Working with the other CMS graduate students at Minnesota, Seth Cooper, Kevin Klapoetke, Abe DeBenedetti, and Phil Dudero have provided a new insight into the daily life of a Research Physicist studying Experimental Particle Physics. Special mention to Seth for the combined work on many similar topics and the contributions to some of the seemingly endless experimental discussions.

The post-docs at Minnesota have provided some of the more detailed insight into working as a physicist. Without Datao Gong I would have been unable to perform my first matrix calibration. Giovanni Franzoni has always been an open ear and full of positive criticism. Nearly all tasks I have completed as a research physicist have been aided by Giovanni's mentoring, guidance and suggestions. All his hard work is greatly appreciated and it has been an honor to have worked with such a dedicated person.

Without my advisor, Roger Rusack, I would not have had the opportunity to work on the awe inspiring CMS experiment. The opportunities with working with the many aspect of calorimetry have been challenging. The advice of Jeremiah Mans has been critical in finishing this thesis. He has kept me on track and provided me with the knowledge of when to let go of a topic. Together they have provided me with many opportunities to further my physics career and I am grateful for those—especially the nice trip to a conference in Hawaii.

The CMS collaboration was formed more than 12 years prior to my joining. The dedication of the many members will one day cultivate some much desired rewards. I would like to acknowledge each member of CMS, as without them this thesis would not be possible. Specifically I would like to highlight a gratitude to the members of the US-CMS collaboration and those at FNAL. More than a three fruitful months were spent at FNAL. Also, I am grateful to the members of the CMS-ECAL community, for unfaltering guidance. With one year spent near Geneva at CERN, I am grateful for the culture of knowledge that supports such a strong union of collaborating scientists.

I am indebted to my many friends, family, and full extended family for always providing positive support and insight. Thank you all as this thesis would have not been completed without your support.

Dedication

To my lovely wife Krystal. Thank you for enduring the many days and nights where I was either away on travel, or completely engrossed in my work. Your love and devotion is forever appreciated. Thank you for your patience. I would never have been able to complete this thesis without you.

To my daughter Elli. I hope your life is filled with happiness! Being able to write my thesis while watching you grow in the first months of your life has been priceless.

Abstract

Before the LHC discovers new physics and new particles, the detectors needed to undergo commissioning. The detection and measurement of Standard Model processes was one way to validate the detector response. Some benefits of the validation procedure were accurate predictions of signals and backgrounds. The rapidity shape of the Z boson was used as a probe into the Probability Distribution Functions of the proton. This thesis discusses the differential Z cross-section measurement with 36 pb^{-1} of integrated luminosity acquired at the LHC on the CMS detector in 2010 at a center of mass of 7 TeV.

Contents

List of Tables

List of Figures

Chapter 1

Introduction

The goal of particle physics is to understand the laws of nature at their most basic and elementary level. Nearly all of the data on the phenomenon of particle interactions fits well within the current model of particle physics, referred as the Standard Model (SM) of particle physics. The use of the Standard Model has consistently displayed a precise predictive power and many parameters have been precisely determined. However, it is known that the Standard Model is not a complete description of nature as it cannot incorporate all observations, such as the experimental fact that neutrinos have mass [1][2], or an explanation for the observation of dark matter [3], which represents 85% of the mass in the universe. Notwithstanding these discrepancies, an important achievement in high energy physics would be the observation of a yet undetected component of the Standard Model: the Higgs boson—the particle that gives other particles mass by the electro-weak spontaneous symmetry breaking mechanism [4][5].

The LHC experiment and the CMS detector are in excellent positions to begin to answer many of these outstanding questions in particle physics. The LHC is a proton-proton collider constructed straddling the borders of France and Switzerland near Geneva. Each beam was operated at 3.5 TeV for the initial phase of operations, with a center of mass energy of 7 TeV. These collisions allowed the exploration of phenomena at regions of energy hitherto unaccessible. The CMS detector is located near the town of Cessy, France, roughly 100 meters underground, and is one of four independent general purpose detectors at the LHC. The detector was designed with a wide acceptance for electrons, photons, muons, and jets in order to address the unanswered questions

of particle physics. As a preliminary step before searching for new phenomena the parameters of the Standard Model and the performance of the detector needed to be commissioned by verifying known processes. Not only were these verification steps necessary, but they could provide an even deeper understanding of the processes which can provide great insight for both the Standard Model and for physics beyond.

The Z boson is an important tool to study the Standard Model because of its high production rate and relatively clean decay channels into muons and electrons. These high transverse momentum (p_T) particles will be similar to those in many searches, either behaving analogous to the signal signature or contributing to the background process. The differential cross-sections of the Z boson decays are also a probe into the parton structure functions of the proton, called the parton distribution functions (PDFs). Improvement in the knowledge of these structure functions allows for more accurate predictions of Standard Model processes and thus an even greater understanding of backgrounds to new signals.

The focus of the thesis is on the differential decays of the Z boson into electrons. Specifically the differential cross-section with respect to the rapidity (Y) of the Z, as both the Y and p_T of the Z are particularly dependent on the PDFs. An accurate measurement of the $Z/\gamma* \rightarrow e^+e^-$ differential shape as a function of Y leads to tight constraints on the PDFs.

Chapter 2 describes the theoretical backgrounds behind the Standard Model and the measurement. The generators used to build a Monte Carlo representation of the detector are also discussed. The LHC and the CMS detector are described in Chapter 3, with an emphasis on the sub-detectors and technology of electron detection and identification. Chapter 4 describes the detector calibrations and the measurement strategy is discussed in Chapter 5. The event selection is described in Chapter 6 and the method for the determination of electron efficiencies is defined in Chapter 7.

In Chapter 8 the measurement efficiencies and the systematic errors estimations are explained. This includes an explanation of how detector resolutions are determined from data. The results of the measurement are tabulated and displayed in Chapter 9, and their implications are discussed.

Chapter 2

Electroweak Physics

Electroweak physics is one of the crowning achievements in 20th century physics. From Rutherford's first remarks to the developments of the full Standard Model, accurate and precise knowledge of the structure of protons has been critical. The same remains true for investigating physics beyond the Standard Model.

2.1 Before the Standard Model

Insight into the internal structure of the atom began in 1909 when Hans Geiger and Ernest Marsden, under the guidance of Ernest Rutherford, were surprised by the observation of large scattering angles when directing α particles at gold foil[6]. The result indicated that the positive charge of the atom was restricted to a very small region within the atom, since a mass larger than the incoming α particle was required to produce the large angles that were observed, as Rutherford suggested in 1911 [7]. The understanding of the structure of the atom was improved with the model of Neils Bohr in 1913 by quantizing the states of the electron orbits ([8], [9]). The continued investigation into the structure of the atom lead to the first evidence for protons observed by Rutherford in 1919 [10]. Subsequently in 1932 James Chadwick reported the discovery of the neutron [11]. These discoveries were complimented by the idea of a strong nuclear binding force between protons and neutrons, as well as insight into the weak force by the idea of the neutrino [12]. From that point on, additional particles were observed and their properties and interactions studied, leading to a greater understanding of

the forces of interaction, culminating in the discovery of the long-predicted weak gauge bosons–the Z^0([13], [14]) and $W^{\pm}$([15], [16]).

2.1.1 Quantum Mechanics

As discoveries of new particles and phenomena were occurring, the mathematical theories behind their interactions were also being developed. In the early 1900's the Schrödinger equation was shown to perform extremely well in describing atomic interactions. One major problem of the Schrödinger formalization was its lack of any mechanism to explain the observations of creation and decay of particles [17]. An early insight in overcoming this problem was the creation of a quantum field theory of free fermions—which is invariant under Lorentz transformations. The free fermion Lagrangian density ($\mathcal{L}$) is shown in Equation 2.1 includes the fermionic field four vector Ψ and Dirac matrices γ^{μ}.

$$\mathcal{L} = i\bar{\Psi}\gamma_{\mu}\partial^{\mu}\Psi - m\bar{\Psi}\Psi \tag{2.1}$$

The solution yielded the Dirac equation, Equation 2.2. Quantization of the field Ψ predicted the possibility of anti-matter.

$$(i\gamma^{\mu}\partial_{\mu} - m)\Psi(x) \tag{2.2}$$

The next important step in the development of a complete field theory was the inclusion of interactions. The simplest form of interaction is the $U(1)$ gauge symmetry where the field is invariant under a phase transformation as shown in Equation 2.3.

$$\Psi(x) \rightarrow e^{i\alpha(x)}\Psi(x) \tag{2.3}$$

To accomplish this invariance, a vector field A_{μ} had to be introduced and the Lagrangian density became as shown in Equation 2.4, with the electromagnetic field tensor $F_{\mu\nu}$ defined as $F_{\mu\nu} = \partial_{\mu}A_{\nu} - \partial_{\nu}A_{\mu}$. Then A_{μ} is a quantized field, the photon.

$$\mathcal{L} = \bar{\Psi}(i\gamma_{\mu}\partial^{\mu} - m)\Psi + e\bar{\Psi}\gamma_{\mu}A^{\mu}\Psi - \frac{1}{4}F_{\mu\nu}F^{\mu\nu} \tag{2.4}$$

The theory of Quantum Electrodynamics (QED) was greatly advanced by the introduction of renormalization from Dyson, Feynman, Swinger, and Tomanaga [18]. The

field theory contained infrared and ultraviolet divergences. These were combined into experimentally measurable quantities such as mass in the mass renormalization shown in Equation 2.5. In this example the mass of the electron is m and the divergent contribution comes from δm. The normalized quantities such as m_{norm} are those measured in experiments. Even though the theoretical values of δm may be infinite, the fact that the measured values of m_{norm} are finite allows the renormalization schema to work.

$$m_{norm} = m + \delta m \tag{2.5}$$

This procedure then provided a natural explanation of the Lamb shift and the anomalous magnetic moment of the electron. Thus QED solidified the role of quantum field theories in explaining particles and their interactions.

2.1.2 Electroweak Field Theory

The theory of the weak interaction was combined with QED into a single field theory by Sheldon Glashow in 1963[19], and revised by Steven Weinburg and Abdus Salam with the introduction of spontaneous symmetry breaking in 1967([20], [21]). The renormalizability of a variety of field theories, including that of the electro-weak theory, was shown by Gerard t'hooft in 1972 [22]. The electro-weak theory is an abelian gauge theory with $U(1) \times SU(2)$ symmetries. This suggested that in the weak sector there are three vector gauge force bosons. These particles were observed at CERN's UA1([13], [15]) and UA2([14], [16]) experiments and reported in 1983, as the Z^o and $W^{\pm}$.

One problem with the initial theory was that the addition of a simple mass term like $(m^2 X_\mu X^\mu)$ to the Lagrangian broke the renormalizability. One solution to this problem was found by Peter Higgs who introduced a field with a degenerate ground state, now called the Higgs field [4]. The ground state was fixed to the vacuum state, breaking the invariance, and was required to have a non-zero vacuum expectation value. This field could be a complex scalar field. The vacuum expectation values of fermions and vector bosons must be zero if the ground state must also be invariant under translations and Lorentz transformations. The simplest form of the field is a charged doublet which yields one degree of freedom—the Higgs boson—after the mixing due to symmetry breaking. Through Yukawa couplings the Higgs mechanism is also expected to give masses to the

leptons and the quarks. However, the Higgs boson has not been detected yet and its detection is a driving force in particle physics.

2.1.3 Quantum Chromo Dynamics

Throughout the middle of the 20th century, many different hadrons were observed and measured in various experiments. In an attempt to structure the discovery of many hadrons, Murray Gell-Mann proposed what became known as the Eight-fold way [23]. This was essentially a representation of quantum-chromodynamics as a $SU(3)$ symmetry, where groups of hadrons were expressed as shown in Equation 2.6 for the lowest order group.

$$(p,\ n,\ \Delta,\ \Sigma^+,\ \Sigma^-,\ \Sigma^0,\ \Xi^-,\ \Xi^+) \tag{2.6}$$

The success of Gell-Mann's Eight-fold way of predicting and explaining hadrons eventually produced the parton model. This lead to the coining of the term "quark" in 1964. Quantum Chromo Dynamics is a field theory built around the non-abelian gauge $SU(3)$. Each quark is a triplet of the symmetry with three possible color charges, red, blue, and green. There is also an octet of gauge bosons which are called gluons. There is an observational fact that quarks and gluons are not observed individually but only in color neutral states. These states are called mesons—quark-antiquark pairs—and baryons—colorless integral charge combinations of three quarks. This observation is explained by the increasing strength of the coupling constant at small energy scales or large distances—leading to confinement.

One problem with such a large coupling constant α_s is that it prohibits the use of perturbation theory to calculate interaction. Each additional order can be larger then the previous. When the energy transfer is larger than 1 GeV the strong coupling constant is small enough to use perturbation theory to calculate observables.

2.2 Standard Model

The Standard Model of particle physics has been highly successful in producing predictions consistent with the data observed in high energy physics experiments. It describes

the interactions of all discovered fundamental particles which interact via the electro-weak and quantum-chromodynamics theories. The Standard Model is a non-abelian gauge theory with a $U(1) \times SU(2) \times SU(3)$ symmetry with twelve gauge bosons: eight gluons and four electro-weak bosons; Z^o, W^+, W^-, and the photon. The are also twelve fermions separated into quarks and leptons in three generations (Table 2.1). Each lepton also has a corresponding anti-particle with opposite charge.

	Charge	First Generation	Second Generation	Third Generation
Quarks	$+2/3$	Up (u)	Charm (c)	Top (t)
	$-1/3$	Down (d)	Strange (s)	Bottom (b)
Leptons	-1	Electron (e^-)	Muon (μ^-)	Tau (τ^-)
	0	Electron neutrino (ν_e)	Muon neutrino (ν_μ)	Tau neutrino (ν_τ)

Table 2.1: Standard Model Fermions

The measurement of the Standard Model parameters is a requirement before the measurement of new phenomena. Although many properties of these Standard Model particles have been determined, many of the predictions of the Standard Model depend on an extrapolation from lower energies of the parameters and needs to be validated for LHC energy domain.

2.3 Deep Inelastic Scattering

Deep inelastic scattering refers to the process of probing the structure of hadrons with high-energy particles. At the LHC the structure of the proton is probed using the combinations of interacting constituent quarks, sea quarks or gluons.

2.3.1 Kinematics of LHC collisions

Most LHC proton-proton collisions produce final states with small transverse momentum (p_T) with respect to the beam direction. The interacting partons themselves have small p_T compared to the longitudinal momentum. Given these circumstances rapidity (Y, Equation 2.7) is a convenient variable. Where E is the energy of the the particle

and P_z is the momentum component along direction of the beams.

$$Y = \frac{1}{2}\ln\left(\frac{E + P_z}{E - P_z}\right) \tag{2.7}$$

The momentum of each parton (p_1, p_2) can then be expressed as a function of rapidity (Y), the transverse mass m_T (Equation 2.8), the detector polar angle ϕ, and the individual measurable momentum components as defined in Equations 2.9 and 2.10. Given these definitions the Jacobian can be expressed as in Equations 2.11 and 2.12.

$$m_T = \sqrt{m^2 + \mathrm{p_T^2}} \tag{2.8}$$

$$p_1 = (E, \mathrm{p_T}\cos\phi, \mathrm{p_T}\sin\phi, p_z) \tag{2.9}$$

$$p_2 = (m_T\cosh Y, \mathrm{p_T}\cos\phi, \mathrm{p_T}\sin\phi, m_T\sinh Y) \tag{2.10}$$

$$\frac{d^3p}{E} = \mathrm{p_T}d\mathrm{p_T}d\phi dY \tag{2.11}$$

$$= \pi d\mathrm{p_T^2}dY \tag{2.12}$$

2.3.2 Proton-Proton Cross-Section

In deep inelastic scattering (DIS), a parton (p_i) from each proton interacts with a given fraction (x_i) of the total proton momentum (P_i) as in Equation 2.13.

$$p_i = x_i P_i \tag{2.13}$$

The interaction between the two partons can be considered independent of the other constituents of the protons somce the interaction happens on a timescale that is short compared to the size of the proton. This leads to introduction of a factorization scale (μ^2)—a scale at which physical processes can be separated between long distance and short distance processes. The proton scattering cross-section (σ), shown in Figure 2.1, is then defined as a function of the individual parton's momentum (x_i), the fractional distribution functions of the different partons' momenta $f_i(x_i;\mu^2)$, the scattering cross-section between the individual partons $(\sigma_{ab\to cd})$, and by integrating over the distribution functions and summing over all the possible combinations of partons, the cross-section is expressed mathematically in Equation 2.14. The terms δ_{had} are the corrections that account for the hadronization of the scattered partons. The process where a quark or

a gluon becomes a hadron or jet of hadrons. These are required if the process's final state includes quarks or gluons.

$$d\sigma(P_A, P_B, Q^2) = \sum_{ab} \int dx_a dx_b f_{a/A}(x_a; \mu^2) f_{b/B}(x_b; \mu^2) \times d\sigma_{ab\to cd}(\alpha_s(\mu^2), Q^2/m^2)(1 + \delta_{had}) \tag{2.14}$$

The hard scattering process ($\sigma_{ab\to cd}$) happens at the scale Q^2 which is defined as either the jet transverse energy (E_T Equation 2.15) or the lepton invariant mass. The hard interaction scale is set to the factorization scale ($\mu^2 = Q^2$).

$$E_T = E \sin\theta_{jet\ to\ beam\ direction} \tag{2.15}$$

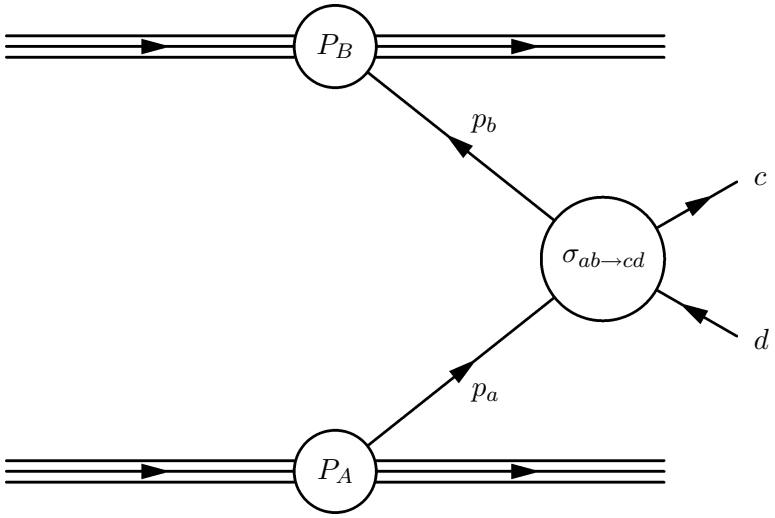

Figure 2.1: Proton-Proton (P_A, P_B) interaction diagram including the two interacting partons (p_A, p_B), the hard cross-section $\sigma_{ab\to cd}$, and the final states particles (c, d). The parton and final state particles are shown with fermionic lines just for illustrative purposes as gluons are allowed.

Knowledge of the internal structure of the proton is a prerequisite to calculations of cross-sections at the LHC. They enter into the calculations as the probability distributions of a parton's momentum within the proton $f_i(x_i; \mu^2)$. These distributions are called the Parton Distribution Functions (PDFs). In Equation 2.14 it is assumed that the PDFs are independent of the process under study. Since these cannot be calculated using perturbative QCD, they need to be experimentally determined, and

many measurements have been conducted to determine the PDFs. Perturbative QCD is used to extrapolate from one interaction scale to another $f_i(x_i;\mu_0^2) \rightarrow f_i(x_i;\mu^2)$ using the DGLAP equations ([24], [25], [26], [27]), with the starting PDFs were determined primarily from global fits to low-energy DIS experiments as described in Section 2.4. Since the LHC is a search machine, to optimize the sensitivity to new physics which are dominated by rare processes, the best possible precision of the PDFs are required. One way to probe the PDFs is in the measurement of the cross-section of Drell-Yan production of Z bosons as a function of rapidity.

2.3.3 Drell-Yan Cross-Section

The process where opposite charged lepton pairs are produced from the annihilation of a quark from one parton and an anti-quark from another proton is known as Drell-Yan production [**?**]. Although the largest contribution at LHC energies comes from the interaction of a quark and a gluon, it is traditional to consider the quark–anti-quark annihilation process as leading order in the strong coupling constant (α_s).

For LHC collisions with a fixed center of mass energy ($\sqrt{s}$), the invariant mass (M), rapidity (Y), and $\mathrm{p_T}$, of the production of Z bosons can be expressed as a function of the momentum fraction of each parton (x_a, x_b). Assuming that the parton masses and transverse momenta are negligiblee, the four momenta of the partons are represented in Equations 2.16 and 2.17 and the Z invariant mass and rapidity as in Equations 2.18 and 2.19.

$$p_a = \frac{\sqrt{s}}{2}(x_a, 0, 0, x_a) \tag{2.16}$$

$$p_b = \frac{\sqrt{s}}{2}(x_b, 0, 0, x_b) \tag{2.17}$$

$$M^2 = x_a x_b s \tag{2.18}$$

$$Y = \frac{1}{2}\ln(x_a/x_b) \tag{2.19}$$

When the parton species are summed over and using the variable $\tau = x_a x_b$, the leading order differential crosssection in Figure 2.2 can be expressed as a function of the individual parton densities $f_{i/I}(x_i)$.

$$s\frac{d^2\sigma}{d\tau dY} = \frac{4\pi\alpha^2}{9\tau}\sum_a Q_a^2[f_{a/A}(x_a)f_{\bar{a}/B}(x_b) + f_{\bar{a}/A}(x_a)f_{a/B}(x_b)] \tag{2.20}$$

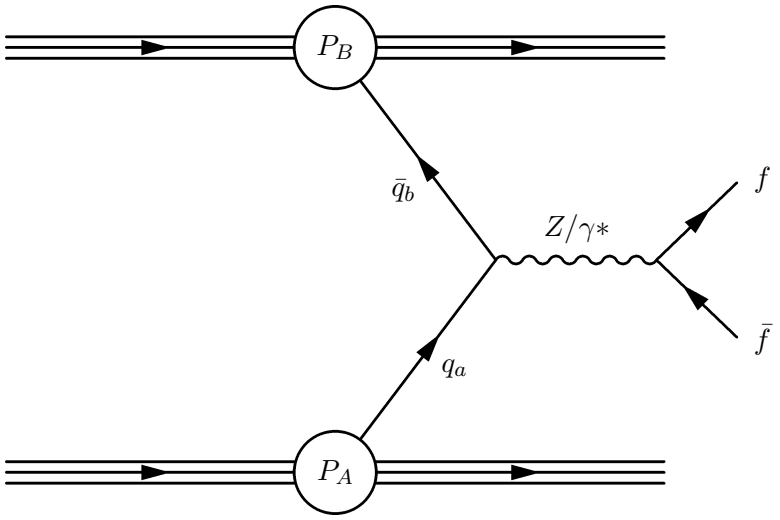

Figure 2.2: Proton-proton (P_A, P_B) interaction diagram for the leading order Drell-Yan production of two interacting quarks $(q, \bar{q})$, with the production of two fermions.

In leading order, the rapidity is correlated with the momentum fraction of the partons as in Equation 2.19. These values can be compared to the proton PDFs at Next-to-Next-to-Leading Order (NNLO) derived from the global PDF fits as shown in Figure 2.3. These include the PDFs for the MSTW 2008 global fits [28] for 10 GeV and 10 TeV energy scales with 68% confidence intervals.

2.3.4 Next-to-Leading Order Cross-Section

The contributions at next-to-leading order (NLO) in the strong coupling constant (α_s) are shown in Figure 2.4. The top two diagrams include loop divergences between the quarks, or on either the incoming quark or anti-quark. The middle two diagrams include the initial state gluon (infra-red parton) emission. The bottom two diagrams are the quark-gluon interactions that lead to the production of a Z boson. These last two contributions are associated with a quark in the final state and are larger than the LO term, due to the large contribution of gluons.

With the additional contributions from Figure 2.4, and setting $\mu^2 = M^2$ in the $\overline{MS}$ schema ([29], [30]), the cross-section is given as in Equation 2.21. The $\overline{MS}$ schema defines the renormlization method and factorization scale discussed both below and in

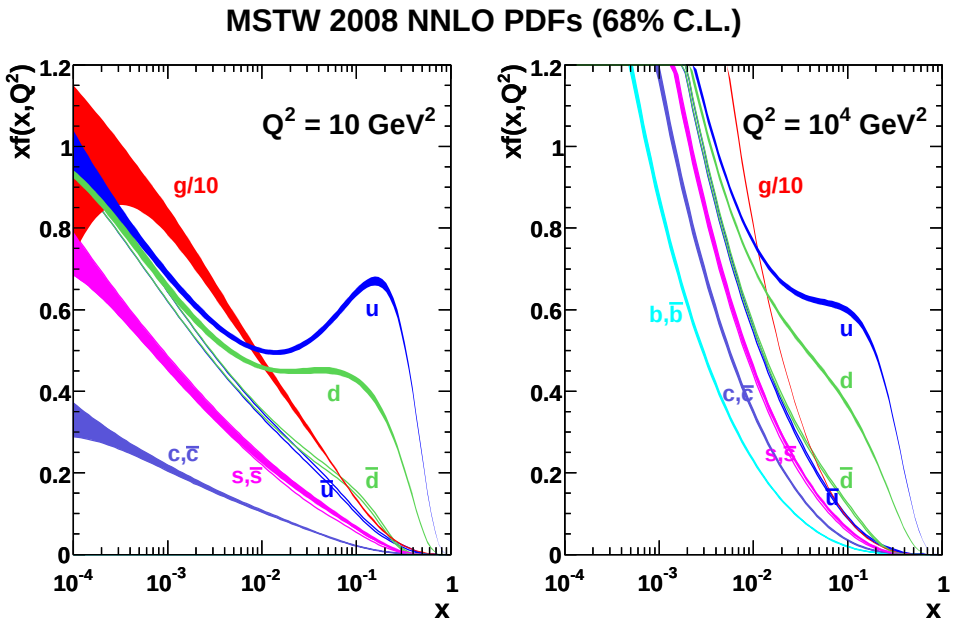

Figure 2.3: Parton PDFs and confidence levels produced by the MSTW collaboration [28].

Section 2.3.2.

$$M^4 \frac{d\sigma}{dM^2} = \frac{4\pi\alpha^2}{9}\tau\left[F_1(\tau, M^2) + G_1(\tau, M^2)\right] \tag{2.21}$$

Where the definitions F_1 and G_1 are given in Equations 2.22 and 2.23. The parameter $D_q(z)$ is a standard functional parameter—a function taking an input value from 0 to 1.

$$F_1(\tau, M^2) = \int_0^1 dx_a dx_b dz \delta(x_a x_b z - \tau)\left(\delta(1-z) + \frac{\alpha_s(M^2)}{2\pi} D_q(z)\right) \times \sum_a Q_a^2 \left[f_{a/A}(x_a, M^2) f_{\bar{a}/B}(x_b, M^2) + (a \leftrightarrow \bar{a})\right] \tag{2.22}$$

$$G_1(\tau, M^2) = \int_0^1 dx_a dx_b dz \delta(x_a x_b z - \tau)\frac{\alpha_s(M^2)}{2\pi} D_g(z) \times \sum_a Q_a^2 \left[f_{a/A}(x_a, M^2)\left[f_{\bar{a}/B}(x_b, M^2) + f_{a/B}(x_b, M^2)\right] + (a, \bar{a} \leftrightarrow g)\right] \tag{2.23}$$

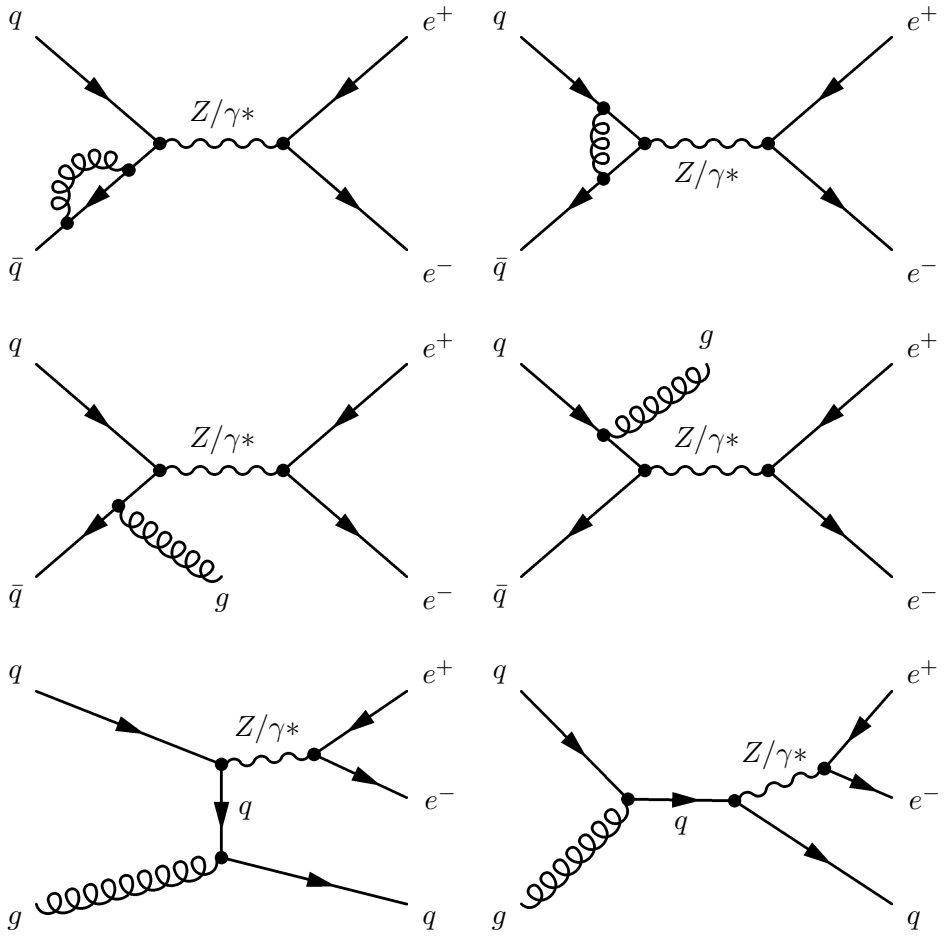

Figure 2.4: Feynman Diagrams for the order α_s corrections.

In both the LO and NLO in α_s the PDF dependence on the cross-section is evident. As can be seen in the definition of Y in Equation 2.19, the different values of rapidity sample different values of parton momenta x_i. The process has currently been calculated to NNLO in α_s at LHC energies.

2.4 Collision Simulation

Simulation, or modeling, of the LHC collision environment is essential when comparing theoretical predictions with observations. Detector simulation is needed for the data analysis and background estimation. It was used to model the geometrical acceptance of the detector, and to ensure the robustness of the analysis and the reconstruction algorithms with the fully simulated data.

There are several Monte Carlo event generators that make different assumptions in the simulations of the collision. They all separate the event into what is known as a factorization schema, where event generation is factorized into the parton distributions, the hard scattering processes, and decays, as shown in Figure 2.5. The generators also take into account the presence of other quarks or gluons, parton shower propagation, parton hadronization, and hadron decay. The differences between the Monte Carlo generators lies in the different parametrization of these factors. Specifically the differences are:

- PYTHIA[31]: PYTHIA models the Hard scattering process at LO. Parton shower approximations are included for the interacting partons, and thus it partially corrects for some higher order calculations.
- POWHEG ([32],[33],[34],[35],[36]): Implements NLO calculations which are then used as inputs to shower Monte Carlo programs. POWHEG BOX NLO calculations were used as an input to PYTHIA.

The simulation of particles within the CMS detector was performed using GEANT4([37], [38]). This simulation tool describes the passage of particles through matter with their interactions.

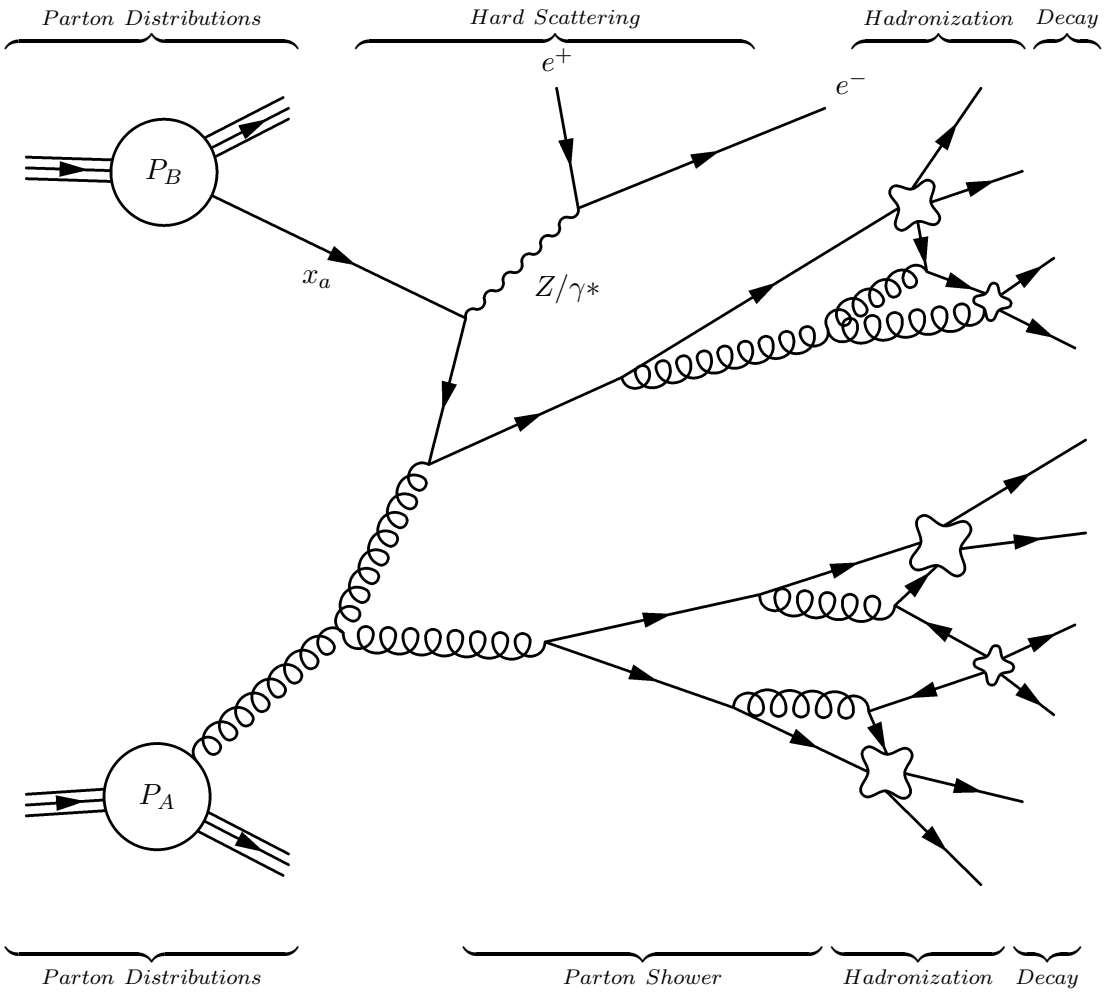

Figure 2.5: Factorization schema for Monte Carlo generators. Each generator makes specific approximations in the calculations of each factor, as well as assumptions in the final multiplication of factors. Any free parton, either before or after the hard scattering, goes through the parton shower simulation, subsequent hadronization–shown as blobs, and hadron decay.

2.5 Summary of the Theory Section

The development and validation of the Standard Model of particle physics is one of the crowning achievements of physics. In order to further explore the phenomena beyond the Standard Model, precision theoretical cross-section calculations are a necessity. The Drell-Yan process is one way to probe the structure of the proton at the LHC and the CMS detector is in an excellent position to perform these measurements.

Chapter 3

Detector Description

The Large Hadron Collider (LHC)[41] is a high luminosity proton-proton collider where two proton beams with energies up to 7 TeV are collided. It is located 100 meters underground just west of Geneva, Switzerland. It is 27 kilometers in circumference four main ALICE, ATLAS, CMS, and LHCb are located at points around the ring where the beams collide. After nearly twenty years, the designing, constructing, and commissioning contributions of almost 10,000 physicists culminated in the first detected proton-proton collisions 2009.

One of the detectors built to study collisions at the LHC was the Compact Muon Solenoid (CMS)([39],[40]). It was designed to explore a new energy regime with a high sensitivity for detection of, and precision measurement of electrons, photons, jets, and muons over a wide range of energies. The detector is depicted in Figure 3.1. The sub-detector closest to the collision point was a silicon tracker. This was built to precisely determine the momenta of the charged particles produced in the collisions. Moving radially outward the next detector was the electro-magnetic calorimeter (ECAL). This was a lead crystal scintillator designed to determine the energies of electro-magnetic showers, and thus identifying photons and electrons. Outside of that was a brass-plastic scintillator sampling hadronic calorimeter (HCAL), whose primary purpose was to detect hadronic showers and to identify hadronic particles. These inner detectors were all placed within a solenoid with a magnetic field of 3.8T. Outside of the magnet, interspersed within an iron return yoke, different types of muon detectors; there were drift tubes (DT's), resistive plate chambers (RPC's), and cathode strip chambers (CSC's).

Collectively they provided accurate charge and momentum measurements for the muons in the field outside of the magnet over a wide angular range.

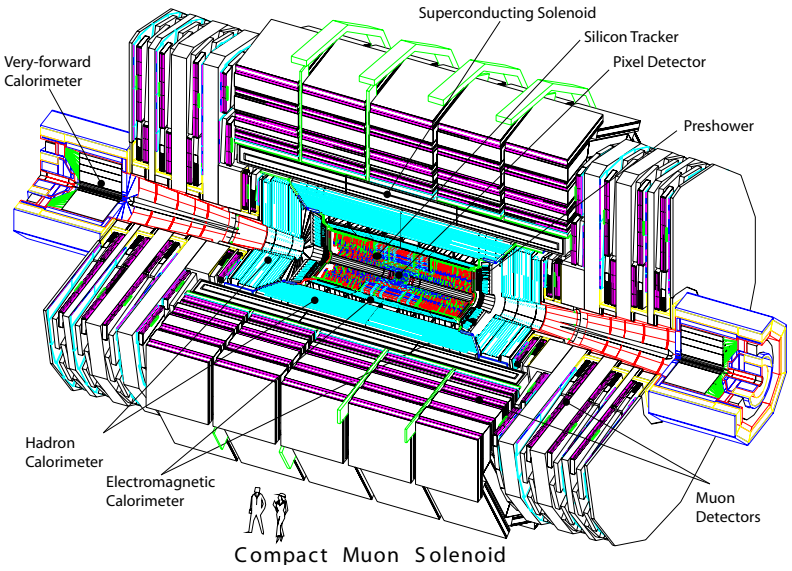

Figure 3.1: Diagram of the full CMS detector. Included are the major sub-detectors: tracker, ECAL, HCAL, and Muon Chambers.

3.1 CMS Geometry

The sub-detectors of CMS were centered around the nominal proton-proton interaction point as in Figure 3.1. The coordinate system was defined such that the z direction was along the beam direction and the x and y coordinates represented the horizontal and vertical directions respectively. The positive direction was defined to be to the right in Figure 3.1 where the exposed face is toward the center of the ring. The angle θ was defined with respect to the z axis, the polar angle ϕ and distance r were defined in the x, y plane. A commonly used unit is pseudorapidity (η_{d}) which was defined with respect to the angle θ as in Equation 3.1. Pseudorapidity is zero when $\theta = 90^{\circ}$ and approaches infinity as the angle approaches zero.

$$\eta = -ln\big[\tan(\theta/2)\big] \tag{3.1}$$

3.2 Tracker

The central design concept of the tracker was to have the highest precision closest to the collision point and many redundant measurements of the same track. The tracker was designed with two main components, both silicon detectors where reversed-bias silicon diodes were placed to detect particles. The inner one had many small pixels approximately 100 square microns and the outer one had longer strip (10 cm) detectors. The tracker was used to measure the momentum and position of charged particles and identify displaced verticies. The detection efficiency was maximized by extending the tracker as close as possible to the interaction point. In addition to providing the ability to identify secondary verticies of long-lived particles like b quarks, an additional two pixel layers of the inner detector were pivotal in measuring with high precision the location of the primary interaction point. The Silicon Strip Tracker (SST) surrounded the Pixel detector, and contained multiple layers of silicon strip detectors used for track reconstruction, momentum measurements, and pattern recognition for tracks with greater than 2 GeV/c of transverse momentum.

3.2.1 Tracker Design

The CMS pixel detector was built with three layers in the barrel at radii of 4.4, 7.4, and 10.2 cm, with an overall length of 53 cm. There were also two forward disks on both sides of the barrel, one at $z = \pm 34.5$ cm with a radius of 6 cm and another at $z = \pm 46.5$ cm with a radius of 15 cm. In all, the detectors had 48 million pixels installed in the barrel and 18 million in the endcaps.

Each module of the silicon strip detector consisted of one or two silicon strip sensors mounted on a tile divided into inner and outer sub-detectors as shown in Figure 3.2. In order to achieve maximal geometrical coverage, the layers were staggered, providing about 10 layers within the rapidity coverage. The silicon strip detector was also divided into barrel and endcap disk regions. The inner part of the barrel detector was built with 4 layers and there were 6 layers in the outer barrel. The inner detector's endcap was built with 3 disk shaped layers and 9 layers in the outer endcap. Some layers, like the first two in the barrel, had double-sided modules with one titled 100 mrad with respect to the beam axis, in order to provide stereo information.

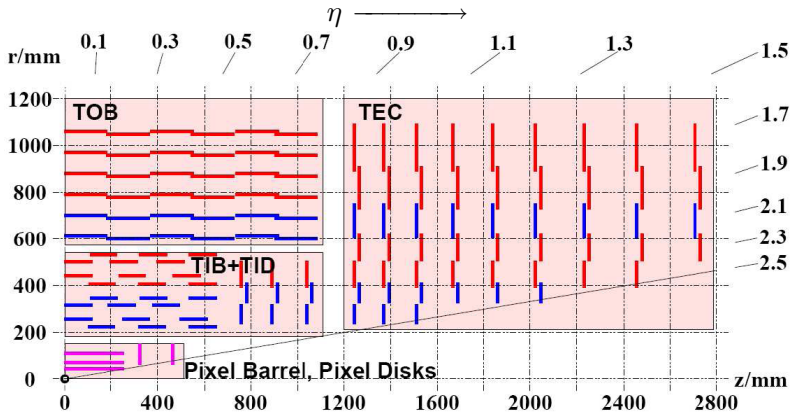

Figure 3.2: One quarter (r, z) cross-section of tracker with η coverage indicator lines on the top and right. The blue lines represent the layers and modules that have read out on both sides. For naming, B=barrel, T=tracker, I=inner, O=outer, D=disk, and EC=endcap. From [42].

3.3 ECAL

The ECAL detector was designed to have a high granularity and an excellent energy resolution to measure electrons and photons. The primary design goal was the ability to detect photons from Higgs$\rightarrow \gamma\gamma$. This set the scale for position and energy resolutions. Of the various detectors considered, scintillating crystals offered the best energy resolution. To fit within the volume of the magnetic field, a high density crystal with a small Moliére radius was required. Furthermore, due to the LHC's small bunch spacing the detector required a fast response and needed to be able to tolerate a harsh radiation environment. To meet these requirements lead tungstate crystals ($PbWO_4$) were chosen as the active medium. These crystals were chosen because they had large density (8.28 g/cm^3) and a small Moliére radius (2.19 cm)[43] and thus allowed for a highly granular detector in a relatively small volume. Compared to crystals used in other experiments (BGO, CSI, *etc.*) [44], the lead tungstate crystals had lower light yields, but were more radiation hard and had a fast scintillation decay times (15 ns for 60% of light) [45].

Due to the relatively low light output of lead tungstate crystals a photodetector with

internal gain and a high quantum efficiency was required. The high magnetic perpendicular to the crystal's field prevented the use of vacuum devices in the central region and restricted the number of gain steps available in the more forward regions, where they would be parallel to the magnetic field. To meet these requirements, avalanche photodiodes (APDs [45]) were selected for the ECAL barrel and vacuum phototriodes (VPTs [45]) were selected for the ECAL endcap.

The APDs used in ECAL were silicon photodiodes with reverse-biased p-n junctions with high internal electric fields where a photoelectron incident on the junction underwent avalanche multiplication. Variations in the avalanche gain could be caused by changes in voltage and temperature—and this needed to be closely monitored. The gain of the VPTs were less sensitive to temperature and voltage fluctuations and where able to sustain the higher levels of radiation in the forward region.

In the barrel detector two 25 mm^2 APDs were glued to the rear crystal surface of each crystal and each APD had a quantum efficiency at 510 nm, where $PbWO_4$ scintillation light peaks, of greater than 80%. The gain was maintained at 50. The VPTs had a lower gain, 10, and had a quantum efficiency that was about 15%. The reduced quantum efficiency was compensated by the larger sensitive area of 1800 mm^2.

3.3.1 ECAL Detector Layout

As in the tracker the ECAL detector was divided into a barrel, two endcap components with the goal of providing full angular coverage up to $\eta = 3.0$. The barrel, which had 61,200 crystals, was mad up with 36 supermodules each half the barrel length and subtended 20° in ϕ. Thus 18 formed a cylinder on each side of the z axis (see Figure 3.3). Each 1,700 crystal supermodule was identical in design with crystals in ϕ and 85 crystals in η. The crystals were placed quasi-pointing geometry toward the nominal interaction point with an offset of 3° in both η and ϕ to maximize the hermeticity of the detector (see Figure 3.4). The crystals were tapered and had an average size of a barrel crystal is approximately $22 \times 23 \times 230 mm^3$. The crystals were assembled in 2×5 crystal sub-modules, which were assembled into modules with either 40 or 50 of the 2×5 sub-modules and four modules were combined to make one supermodule. There was a small fiberglass structure placed around each 2×5 sub-module and a slighter larger structure around each module.

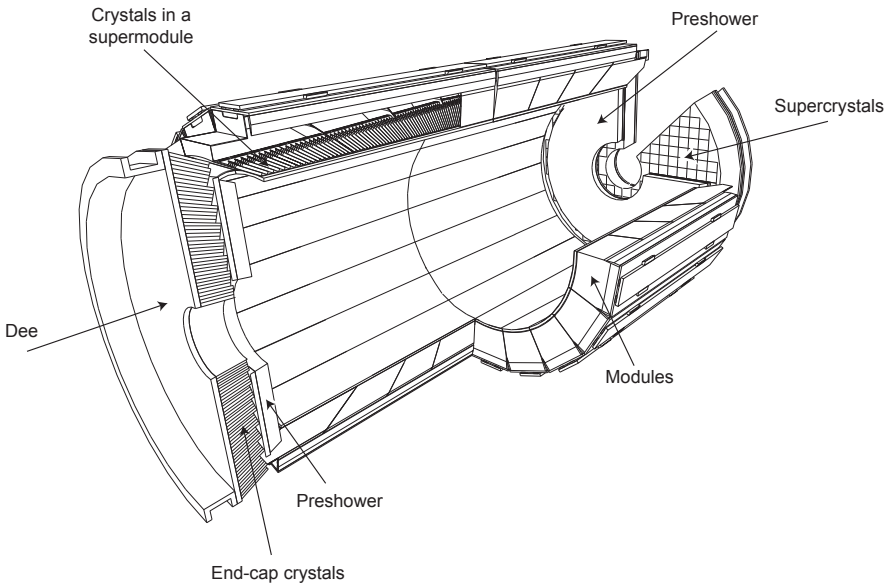

Figure 3.3: Full ECAL diagram showing the module structure. From [45].

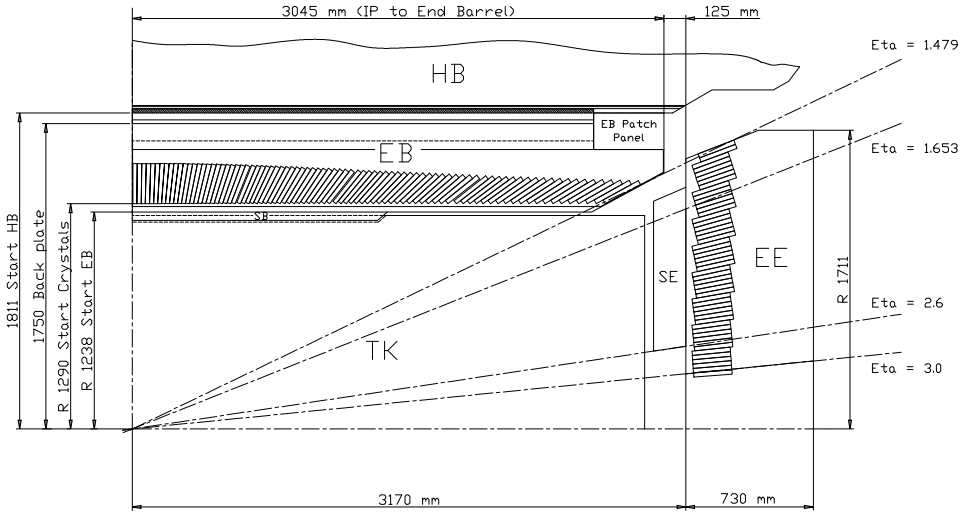

Figure 3.4: One quarter r, z cross-section of ECAL. The crystal quasi-pointing geometry can be seen. For naming: EB=barrel, EE=endcap. The optional high luminosity $|\eta| < 0.9$ barrel preshower detector is shown. From [45].

The ECAL endcaps were built in 4 module structures called DEEs—a semicircular structure. Two DEEs combined to form an endcap. Each DEE was constructed of 4996 crystals arranged in a quasi-pointing projective (x, y) grid geometry extending from η of 1.5 to η of 3.0. The average size of an endcap crystal is $30 \times 30 \times 220\text{mm}^3$, slightly larger than the barrel crystals. A preshower detector was placed in front of the ECAL endcaps to provide enhanced π^o/γ separation. They were organized in two planes, with a total of 4300 silicon detectors, one plane had 0.9 radiation lengths of lead absorber in front of it and a second, deeper, with 1.9. The preshower measured the position of a particle with a precision of 300 μm (see Figure 3.5).

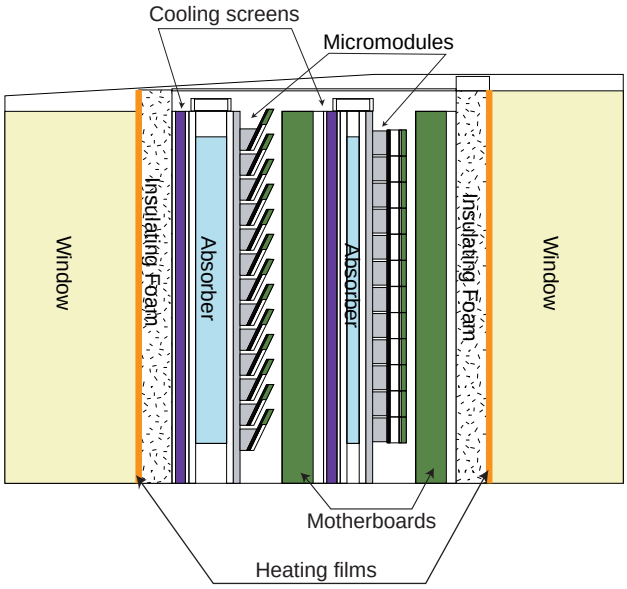

Figure 3.5: A detailed diagram of the ECAL Preshower. From [46].

3.3.2 ECAL Energy Resolution

The ECAL energy resolution was characterized by a stochastic term (a), a noise term (b), and a constant term (c) (Equation 3.2).

$$\left(\frac{\sigma_E}{E}\right)^2 = \left(\frac{a}{\sqrt{E}}\right)^2 + \left(\frac{b}{E}\right)^2 + (c)^2 \tag{3.2}$$

The stochastic term (a) represents contributions from the photostatisics of the energy deposition and lateral shower containment fluctuations. The energy scales linearly with the number of photons in the $PbWO_4$ crystals, and the resolution for the number of photons follows Poisson statistics ($\sqrt{N_{photons}}$); therefore, the photostatistics term had a $\sqrt{E}$ dependence. As the energy is proportional to the track length of a shower and the shower development process is stochastic with a resolution of $\sqrt{\text{shower track length}}$, the variance in electromagnetic shower size was responsible for the $\sqrt{E}$ dependence on the shower containment fluctuations.

Contributions to the noise term (b) included pileup noise—signal mixing from earlier and later events—and electronics noise. Pileup noise increases with increasing luminosity as the frequency of collisions goes up and thus the probability of signal contamination from a nearby events heightens. Electronics noise grows with time as irradiation of the APDs will lead to a rise in the dark current over time.

The constant term (c) accounts for a combination of the inter-calibration errors, temperature dependence, crystal non-uniformities in the longitudinal direction, shower leakage through the back face of the crystals, and geometry effects like gaps and module boundaries. The constant term dominated the energy resolution at high energies. Each component was either tracked or understood in Monte Carlo; temperature was tracked with thermistors to high accuracy, radiation damage and crystal non-uniformity were tracked with a laser monitoring system, back face leakage and geometry corrections had been shown to have less than a 0.3% contribution from GEANT4 Monte Carlo studies, and inter-calibration errors–the largest contributor–were tracked with physics events.

3.4 HCAL

The hadronic calorimeter system (HCAL) was designed to measure quarks, gluons and neutrinos by measuring the direction of particle jets and missing transverse energy. An accurate determination of the missing transverse energy in an event is essential for signatures of new particles such as in supersymetric partner searches. Signals from the hadronic calorimeter were used to identify electrons, photons, and muons in partnership with the other sub-detectors.

The barrel and endcap hadronic calorimeters covered an angular region of $|\eta| < 3$,

as is shown in Figure 3.6. The detector was built with alternating layers of brass absorbing plates and plastic scintillator. The 4mm thick plastic scintillators were read out with wavelength-shifting plastic fibers coupled to detectors. Fibers were used to bring the light to the photodetctors. Hybrid photodiodes (HPD) were selected because the photodetectors were required to [47]:

- Be able to survive 10 years of LHC radiation environment at the nominal particle luminosity $10^{34} cm^{-2} s^{-1}$.
- Be stable in the solenoid 4T magnetic field.
- Be able to detect a minimum ionizing particle (MIP) in a single readout channel.
- Have linear dynamic range of 10^5.
- Able to measure with 1% precision the signal generated by a DC radioactive source.

These requirements were all met with HPDs. The HPD was designed to be an electron bombardment device where an electric field accelerated photoelectrons from the photocathode to a silicon diode target producing a current of electron-hole pairs. In CMS they were operated with a 10 kV electric potential across a 1.5mm acceleration gap [47].

The forward hadronic calorimeter (HF) covered a pseudorapidity range of $3.0 < |\eta| < 5.0$ as shown in Figure 3.7. Due to the much larger fluence of particles in this region, a detector with a high radiation tolerance was required. The HF used quartz readout fibers as the active medium, which were placed within a steel absorber matrix about 10 nuclear interaction lengths (165 cm) in length. Since quartz fiber does not significantly scintillate, only Cerenkov light from electrons in electromagnetic and hadronic showers was detected. This resulted in much narrower and shorter showers than a similar calorimeter based on scintillation light. The HF also had a unique feature of having fibers of two different lengths distributed as in Figure 3.8. Half of the fibers began where the steel absorber matrix started, and thus sampled the full shower; the other half of the fibers began 22 cm after the front face of the steel absorber and sampled primarily the hadronic fraction of a shower. With two samplings of the depths

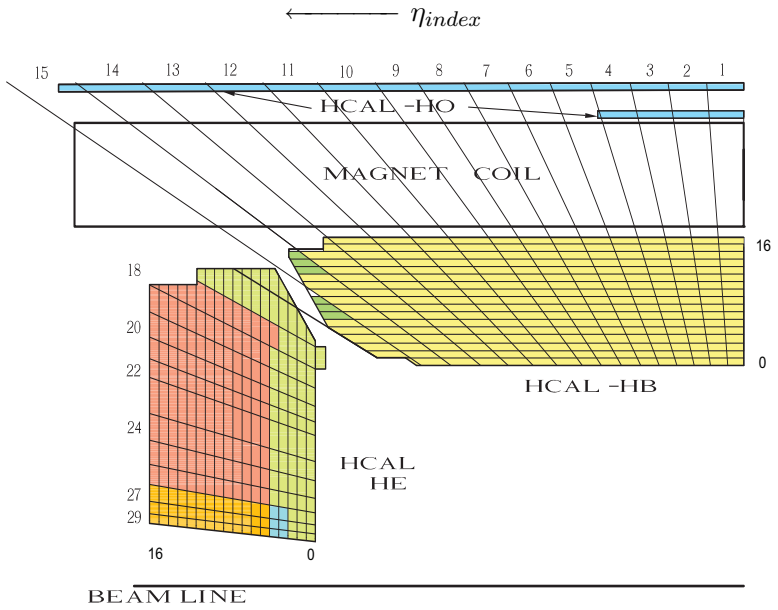

Figure 3.6: One quarter r, z cross-section of the HCAL barrel (HB) and HCAL endcap (HE) calorimeters. The tower segmentation is shown and different colors correspond to independent longitudinal readout regions within a tower. From [48]

of localized showers, the HF detector extended the coverage for electrons, photons, jets, and $\not\!\!E_T$ to $|\eta|$ of 5 [49].

3.4.1 HF Energy Resolution

HF energy resolution as described in Equation 3/2 with statistical components and a constant term.

- Photoelectron statistics: $a/\sqrt{E}$ from sampling fraction
- Sampling fluctuations: $\sigma/E = a/\sqrt{E}$ with $a = b\sqrt{d/f}$ given the diameter d, and sampling fraction f of the fiber.
- Constant term: Due to lateral shower dimension on the same order of magnitude of fiber pitch.

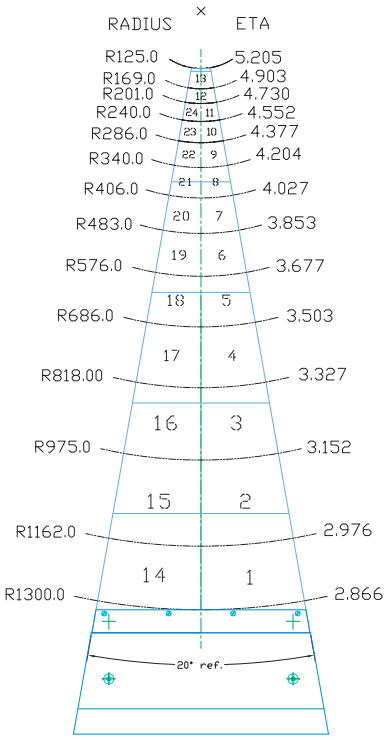

Figure 3.7: A 20° slice of HF showing the transverse module segmentation of 0.175×0.175 in $\Delta\eta \times \Delta\phi$. Only modules 12 and 13 have larger segmentation. From [49]

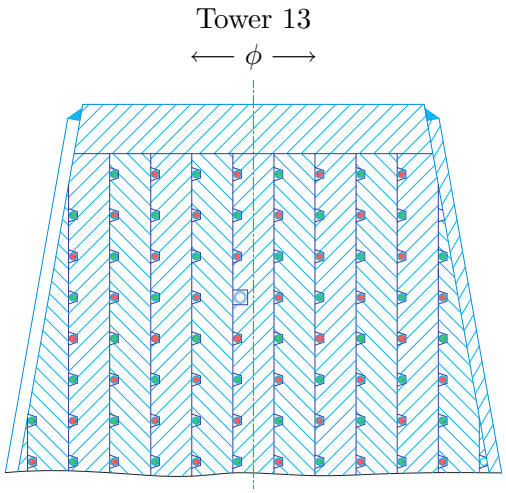

Figure 3.8: Detailed layout of HF tower 13. The central square region represents the radioactive source tube. The alternating red and green colors indicate the layout of the alternating long and short fibers. From [49]

Since the Cerenkov light of hadronic showers in HF sampled the electromagnetic shower core, which was dominated by neutral pions, the fluctuations in the neutral pion production dominated the hadronic energy resolution. For electromagnetic particles the energy resolution was smaller, as seen in Figure 3.9.

- HF Hadronic: a=280% and b = 11%.
- HF EM: a=198% and b = 9%.

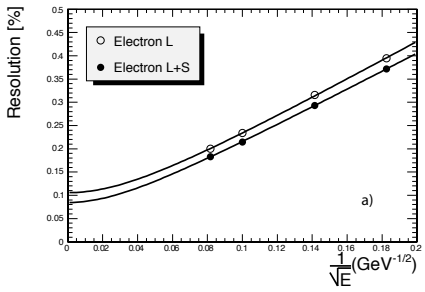

Figure 3.9: The electromagnetic energy resolution for HF determined with electron test-beam. They fit to a=198% and b=9%[49].

3.5 Muon Chambers

The CMS muon system covered a region of $|\eta| < 2.4$ and was composed of three types of detectors. Drift tubes in the barrel section out to $|\eta| < 1.3$, cathode strip chambers in the endcaps, and resistive plate chambers in both. Drift tubes operated in the barrel as most of the magnetic flux was contained within the iron return yoke. CSCs were selected in the endcaps where they were large varying magnetic fields. They also have a faster response and a finer segmentation necessary in the high rate environment. RPCs were installed throughout the muon system in order to provide accurate timing information with a highly segmented trigger.

The muon system was designed to optimize the muon identification, trigger, charge, and momentum measurements. To meet the muon identification criterion, the detector

was built with 16 interaction lengths (λ) of material without acceptance losses. The muon trigger was designed to be fast and with the ability to assign the muon to the correct bunch crossing for a p_T range of 3 GeV to 100 GeV. The muon charge identification was designed to have an efficiency of greater than 99%. Global momentum measurements were expected to have an error of 1% for the low energy threshold to between 6% and 17% for 1 TeV.

3.5.1 Muon Detector Layout

The barrel muon chambers were separated into four stations for each of the five rings. Each ring was 2.5 m thick in the z direction. The endcaps were arranged in trapezoid shaped modules arranged in a series of concentric rings which combined into one of the four stations. The entire CMS cross-section view can be seen in Figure 3.10, with highlights on the muon system.

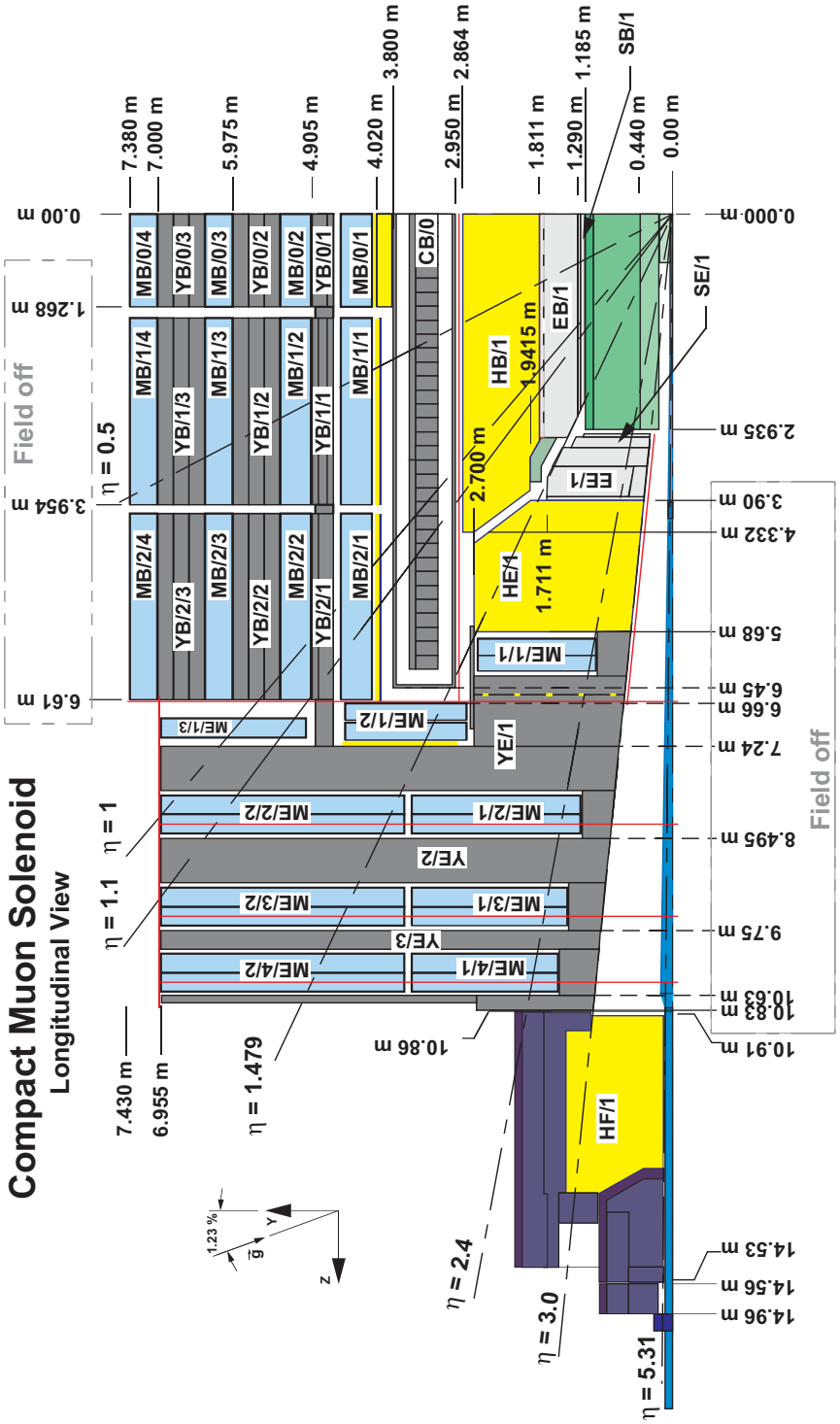

Figure 3.10: Full one quarter r, z cross-section of CMS. The muon modules are labeled in light blue with MB=Muon Barrel, and ME=Muon Endcap. From [50]

Chapter 4

Calibration

The validation of the response of each detector was necessary prior to publishing the first physics results. It was also important that the detector began data taking as close to design parameters as possible. These validation and performance requirements not only maximized the usefulness of the first data, but also served as a first step in detector certification.

4.1 ECAL Calibration

For photons and electrons with energies above a few GeV, the ECAL played the crucial role for energy measurement. As discussed in Section 3.3.2 the high energy resolution in ECAL was dominated by the intercalibration errors. Therefore, the start-up performance of the calorimeter was affected by large inaccuracies in intercalibrations. It was then necessary to determine their values prior to detector start-up. During the acquisition of data multiple methods based on physical processes were used to track the intercalibrations.

4.2 ECAL PreCalibration

For the precalibration of ECAL four different methods were utilized: a direct light yield measurement the of crystals, cosmic rays, charged beam, and beam splash. The light

yield measurements were the result of quality assurance checks performed on all crystals prior to electronics installation. A cosmic ray intercalibration was performed on all barrel supermodules with varying statistics. No cosmic ray intercalibrations were available for the endcaps given construction delays and crystal orientation. Due to limited test beam availability, only 10 barrel supermodules and 1 endcap supermodule were exposed to high precision electron beams—the best available intercalibration method. In 2008 and 2009 beam splashes containing order ten million synchronous muons provided relatively accurate startup intercalibrations for the ECAL endcap detector.

4.2.1 Light Yield Intercalibration

A ^{60}Co source was placed in front of each crystal and a PMT was affixed to the rear of the crystal where the APDs were to be located. The light yield value was found from a measurement of the the transmission of the signal from a value obtained with a low energy 1 MeV photon from the source. These data were recorded as the number of photoelectrons detected by the PMT per MeV of energy incident on the crystal. The precision of this measurement was limited by crystal uniformities, linearity of the extrapolation to GeV energies, statistics, and lack of APD with final readout electronics. An additional precision was gained by combining the measurement of the transverse transmission with the longitudinal transmission.

In order to determine the accuracy of the light transmission measurements, the final combined values were compared to 50 GeV and 120 GeV electron test-beam. The precision of the method can be seen in Figure 4.1, and was determined to be 4.5% for 100 crystals. Since the electron test-beam constants were far more accurate, the RMS could be extrapolated as an estimate on the precision of the light yield measurements on supermodules without test-beam.

4.2.2 Cosmic Ray Intercalibration

Due to test beam availability and CMS construction constraints, high precision test beam intercalibration was performed on only 10 of the 36 barrel supermodules. To make up for the lack of high quality data an intercalibration was performed with cosmic rays. A special setup was built to hold an individual supermodule. The supermodule

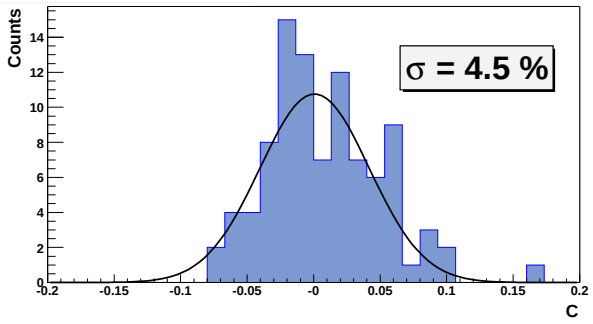

Figure 4.1: Light Yield PreCalibration Accuracy by comparison of the Light Yield transmission value to test-beam determined values [51].

was inclined 10° to maximize the cosmic flux on the far end as the angle of the crystals changes by 60° from one η end to another. It was not inclined any more than 10° for safety concerns. Scintillator paddles were placed to completely cover the bottom of the supermodule, and to form a ring around the top. A final paddle was placed near the nominal position of the interaction point as shown in Figure 4.2. The trigger was a coincidence of hits from the scintillator near the interaction point position and one below the supermodule. This resulted in a trigger which preferentially selected cosmic rays that directly traverse a single crystal. Due to the length of the interaction point scintillator counter, the configuration also had a high acceptance at selecting many of the cosmic rays which go through two adjacent crystals.

When these data were collected the supermodules were equipped with the full production electronics. A single through-going cosmic muon would deposit an average about 250 MeV in a 23 cm long crystal. The electronics noise was determined to be 40 MeV at the nominal operating APD gain of 50. In this test the APD gain was increased by a roughly a factor of four in order to increase the signal-to-noise ratio and the resulting electronics noise for the cosmic ray intercalibration was 10 MeV. An additional benefit of the increased APD gain and signal-to-noise ratio was that an independent particle tracking system was unnecessary. The triggering rate was manageable and neighboring crystals could be used as a veto for muons that were not through-going. One limiting factor to this calibration was the difference in operational APD gains. The ratio of the

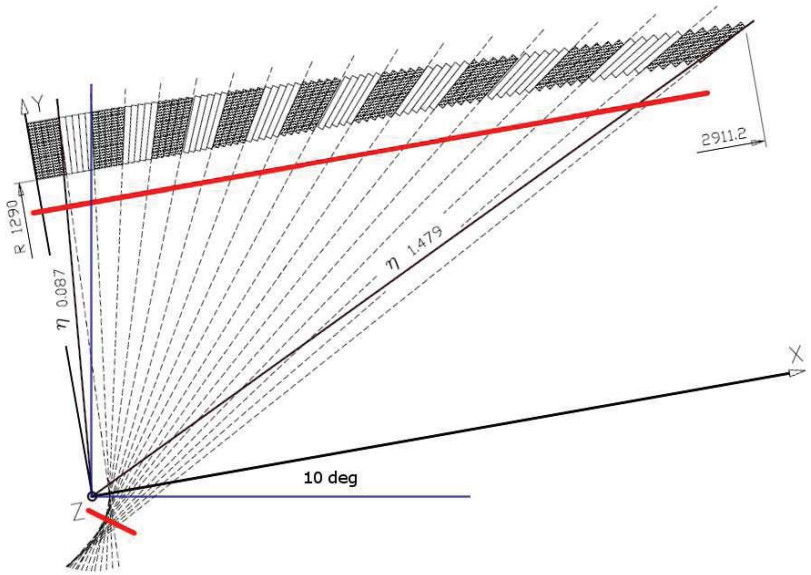

Figure 4.2: Cosmic ray trigger and setup. Red lines indicate the positions of the triggering scintillators. Projective lines are shown to represent the paths of cosmic rays that traversed single crystals. From [52].

APD gains of 200 and 50 were not identically equal to four, because the HV distribution in ECAL did not operate the HV for APDs individually, a single HV channel was used to power 100 APDs mounted on 50 crystals. The readout of the individual APDs were grouped such that they required a similar HV value to produce a gain of roughly 50. The true APD gain-200 to gain-50 ratio was measured with the ECAL laser monitoring system, with each crystal receiving a laser pulse at both gains and the ratio was found. The average value was 4.1 with an RMS of 2.6%. The error on the determination individual APD gain ratios was only 0.1%.

Cosmic Calibration Selection

Two independent analyses were performed on mutually exclusive datasets. The selection for each analysis required either a crystal, or a crystal pair above a defined threshold, while rejecting an event if any of the neighboring crystals had measurable activity. All

crystals around the active crystals were required to have less than 3 ADC (27 MeV) of activity as shown in Figure 4.3 and all selections were greater than 3 ADC. Therefore, rejecting the neighbor crystals made the datasets completely independent.

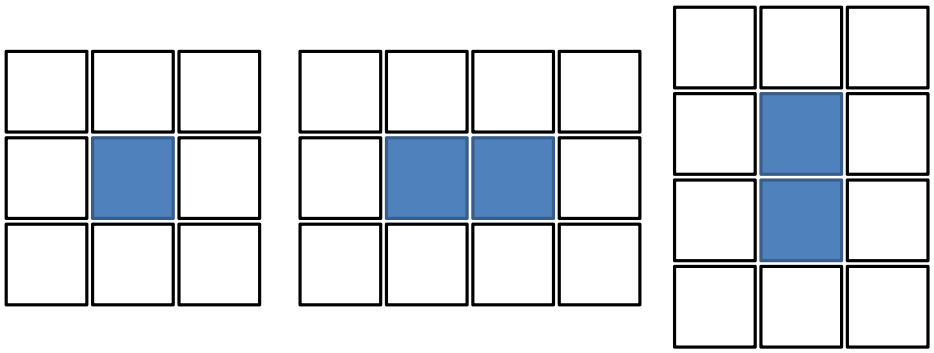

(a) Single crystal selection (b) Same η pairs (c) Same ϕ pairs

Figure 4.3: Cosmic Ray Selection. All white crystals were required to have less than 3 ADC and all blue crystals were required to have more as shown in Table 4.1. E_A is the highest energy crystal, and E_B is the second highest energy crystal.

Intercalibration Method	Selection
Single Crystal	$E_A > 10ADC$ and $E_B < 3ADC$
Crystal Pairs	$E_A > 5ADC$ and $E_B > 5ADC$ or $E_A > 9ADC$ and $E_B > 3ADC$

Table 4.1: ECAL Cosmic intercalibration selection. E_A is the highest energy crystal. E_B is the second highest energy crystal. All others must be less then 3 ADC (27MeV). The Crystal Pairs represent the Same η pairs and the Same ϕ pairs shown in Figure 4.3.

The selection efficiency was verified using a Monte Carlo simulation package H4SIM [53] which was based on GEANT4 ([37], [38]). For both the single crystal and crystal pair methods the selections remained robust against electronics noise. The default distributions were verified using the seven electron test beam inter-calibrated supermodules. Then reference pulse-height distributions were constructed for these supermodules. The

selection in the two dimensional energy space of Figure 4.4 shows the dataset separation and noise rejection.

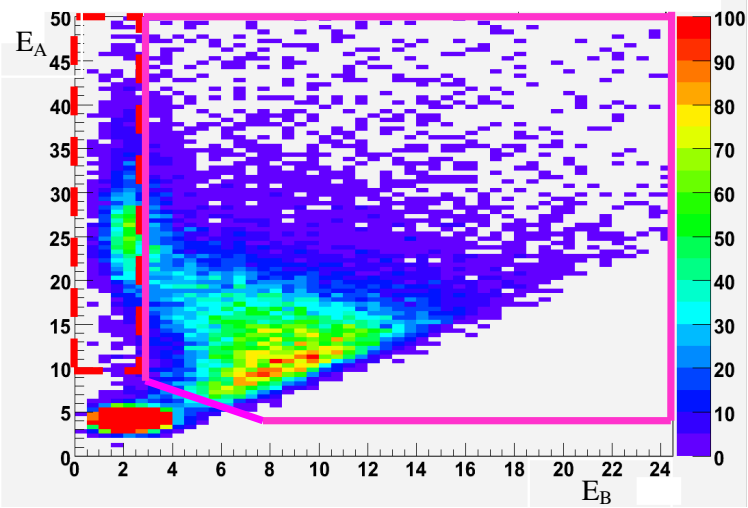

Figure 4.4: ECAL Cosmic Energy Selection. Pink dashed boxed selection is Single crystal; Red solid lined selection is for crystal pairs.

Single Crystal Method

The single crystal intercalibration procedure utilized a maximum likelihood fit. Maximum pulse height distributions (E_A) were made for each crystal and then fit to a set of 17 reference distributions (Figure 4.5). The distribution with the maximum likelihood was selected, and the relative scale factor from the fit was the intercalibration constant for the crystal. The reference distributions were generated based on cosmics data. Test-beam determined intercalibration constants were applied to cosmics data and pulse height reference distributions were created by averaging the distributions over all crystals in seven supermodules within each of the 17 regions. The use of test-beam intercalibrations automatically normalized the cosmic energy regions to the 50 GeV electron test-beam equivalent values and eliminated the need for a Monte Carlo to correct the energy depositions. Averaging over many crystals and supermodules eliminated any significant bias introduced by using the test-beam intercalibrations. The mean scale factor

between the seven supermodules had an RMS of 0.3%. This was a direct measurement of the systematic error of the method when the reference distributions were applied to supermodules that did not have electron test-beam intercalibration.

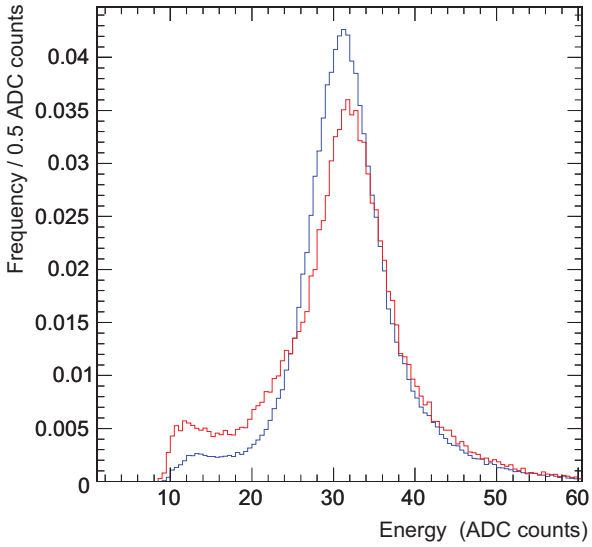

Figure 4.5: Single crystal cosmic energy distribution. Blue line for a low η distribution, red line for a higher η distribution. From [52].

For crystals near module boundaries and those near the edges of a supermodule the neighboring selection was less efficient. They were treated separately and assigned a larger error as the signal-to-noise was much smaller. Different pulse height reference distributions were then used in the supermodule edge regions.

Crystal Pair Method

A standard matrix inversion method was used for the crystal pair events. The total energy was defined as the sum energy of each crystal. The energy in a crystal was defined as the multiplication of the intercalibration constant and the raw readout value (Equation 4.1).

$$E_{Total} = c_1 E_1 + c_2 E_2 \tag{4.1}$$

A χ^2 goodness was defined as the difference between the measured energy and the expected energy taken from a reference region (Equation 4.2).

$$\chi^2 = \sum_{Events} \frac{(E_{expected} - E_{measured})^2}{\sigma_E^2} \tag{4.2}$$

The χ^2 was minimized for each constant and the two elements were set equal to each other. As all components were just array elements, they could be summed over all events. Then the final matrix could then be inverted while being characterized by the convergence between iterations (see Appendix A for more details).

As in the single crystal analysis, reference values were also derived from cosmic data. The same seven supermodules with available test-beam intercalibration constants were used to determined the peak positions in the crystal pair summed energy distributions. The benefits of using the test-beam determined constants were the relative accuracy, and using seven minimized a single supermodule bias. As η increased, the width of the energy distribution increased as well. For the pairs with the same ϕ the width increased significantly, and peak value shifted to lower energy (Figure 4.6). The varying distributions were a result of sampling of different angular cosmic spectra convolved with the staggering of ECAL crystals. Combinations which included a crystal near an edge or module border were treated separately (Figure 4.7). The values were averaged over the specified regions, binned in η and over the seven reference supermodules. This method produced a larger expected peak error for those crystals near the edge and module boundaries—due to fewer reference crystals, but the increase was not significant compared to the increased statistical error in those regions.

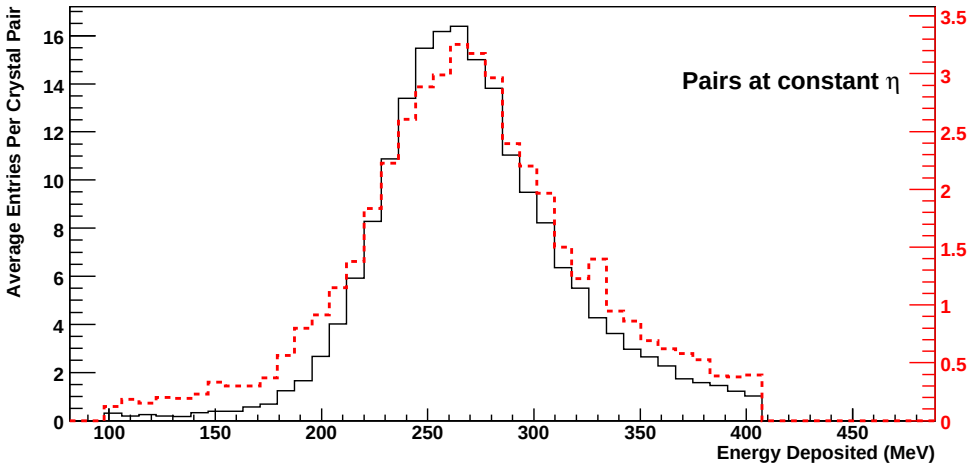

(a) Same η pairs

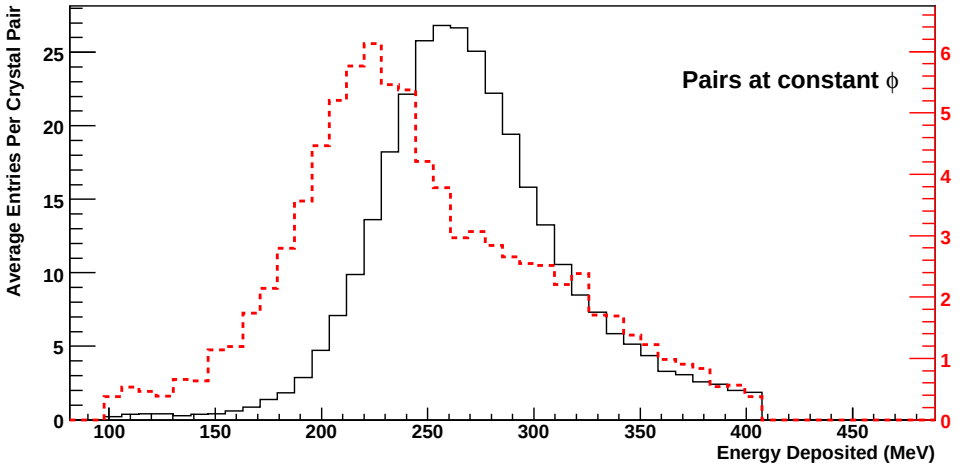

(b) Same ϕ pairs

Figure 4.6: Typical combined energy distributions for crystal pairs for supermodule 16. Black line for pairs are the average for a ring (18 crystals) in the low η region ($i\eta = 17$). Red dashed line for pairs are the average for a ring in the high η region ($i\eta = 72$).

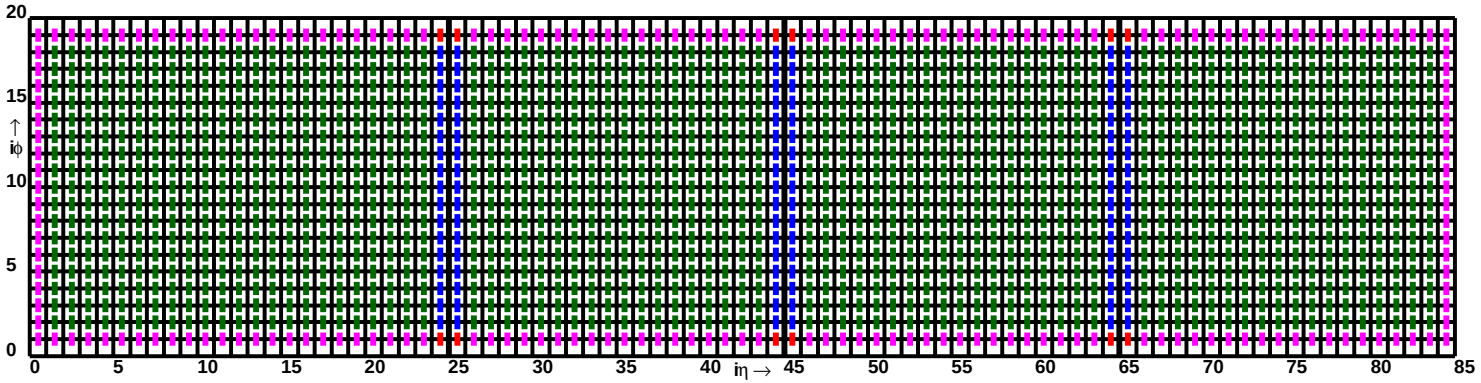

(a) Same η pairs

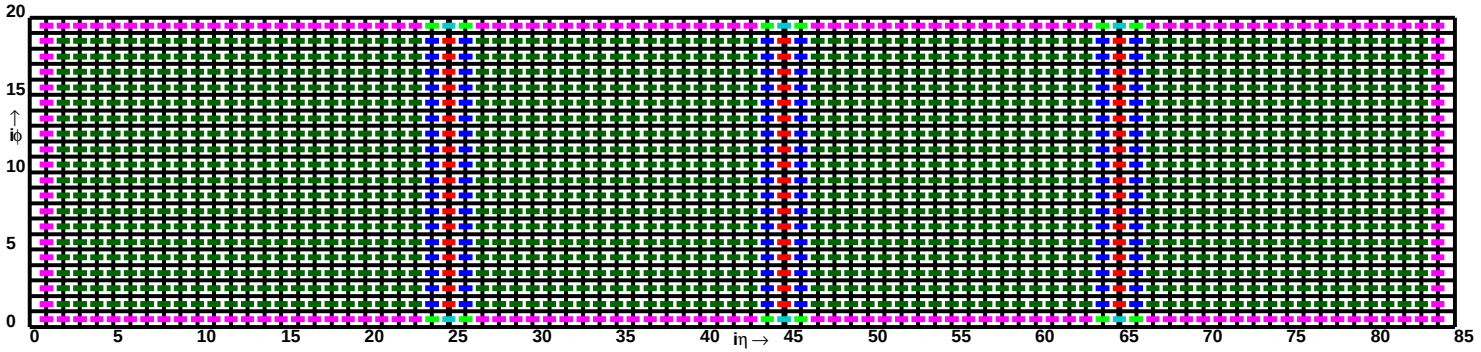

(b) Same ϕ pairs

Figure 4.7: The definitions of the crystal pairs. All 1700 crystals within a supermodule are shown. The lines crossing into two crystals represent the pair combinations. The colors correspond to different pair types. The 18 non-edge crystals were treated as part of one set, mostly in green. The other colors represent module border and edge crystal combinations which required special expected energy deposition values. The boundary pairs are different because of inefficiency in selection and energy loss in gaps.

The means of the resulting reference distributions as a function of η are shown in Figure 4.8. Those means were used as the expected energy in the matrix inversion technique. These values were assigned a systematic error of 0.3% based on the stability of the reference distributions between the supermodules as displayed in Figure 4.9. Here the mean of each of the seven reference supermodules were compared to the average of all seven for each pair type.

Statistical Accuracy

The statistical accuracy was determined for each of the three datasets by splitting each data sample in half. The comparison of even numbered to odd numbered events is related to the total statistical accuracy σ_{Stat} as in Equation 4.3. Where $\sigma_{even-vs-odd}$ represented the width of the distribution of the difference of the two sets of calibration constants as shown in Equation 4.4. The statistical accuracies for the same η and same ϕ pairs as a function of η are shown in Figure 4.10

$$\sigma_{Stat} = \frac{\sigma_{even-vs-odd}}{2} \tag{4.3}$$

$$\sigma_{even-vs-odd} = \sqrt{\frac{\sum_i^N c_i^{odd} - c_i^{even}}{N-1}} \tag{4.4}$$

Comparison with Test-Beam Intercalibration

The systematic uncertainty was estimated by comparing with the test-beam. The comparisons to test-beam allowed for the determination of systematic uncertainty. There were typically 300 events for the single crystal calibration and about 250 events for each of the crystal pair combinations for the low η region. For the high eta region there were typically 100 single crystal events and 50 crystal pair events for each pair combination.

Using the individual statistical and systematic accuracies found from direct comparisons to test-beams, the three cosmic calibration constants were combined using Equation 4.5. The combined cosmic intercalibration constants were compared with the test-beam values. The resulting distribution and the estimated precision versus η are shown in Figure 4.11, where the precision was determined by the η ring averaged values

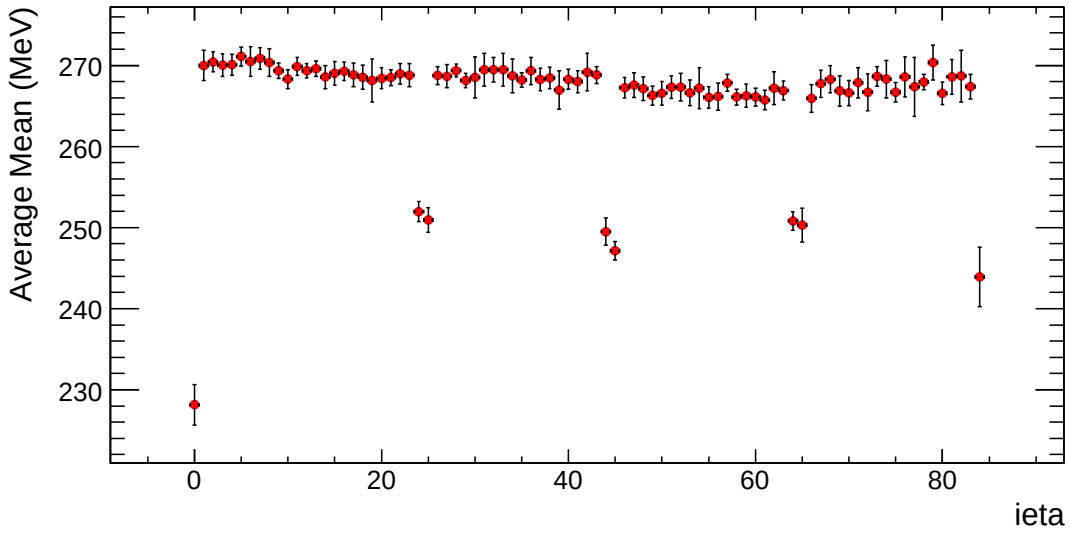

(a) Same η pairs

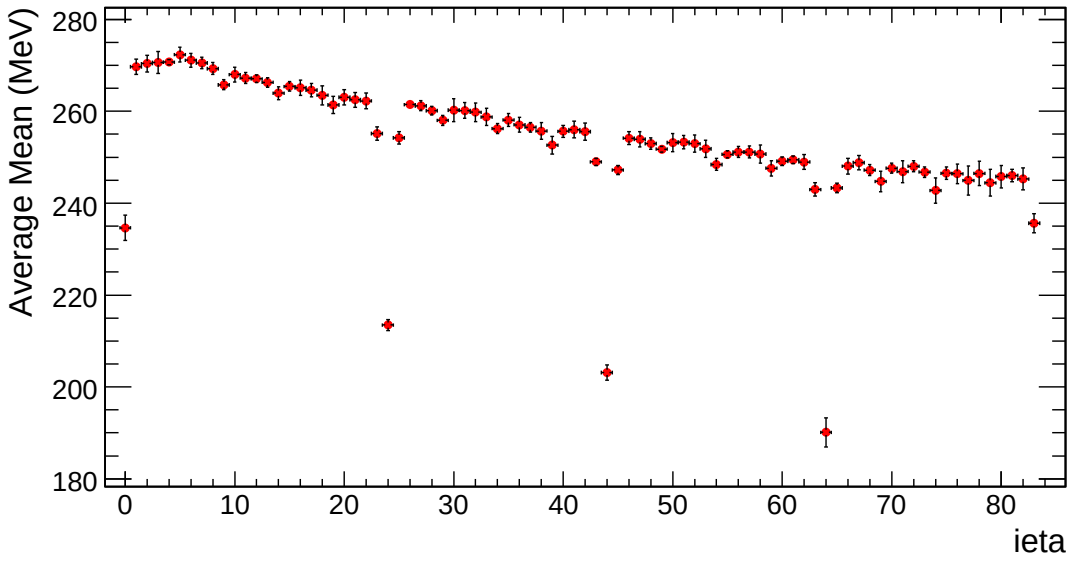

(b) Same ϕ pairs

Figure 4.8: The η distribution of the mean of the reference distributions. Averaged over 18 crystal rings over seven supermodules.

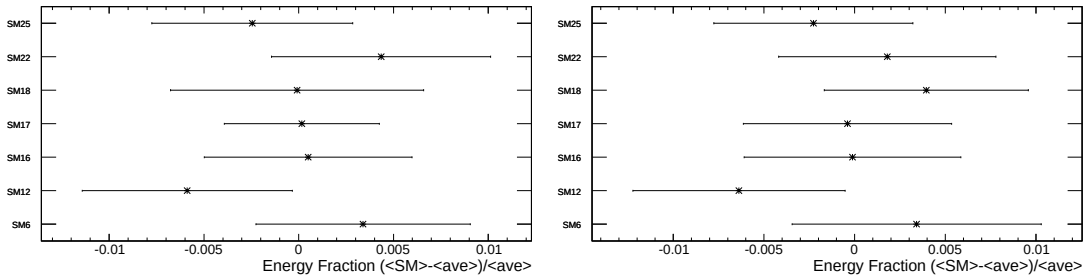

(a) Same η pairs (b) Same ϕ pairs

Figure 4.9: The variance in mean of the reference supermodules for the same η and same ϕ pairs. For both combinations the RMS was determined to be 0.3%.

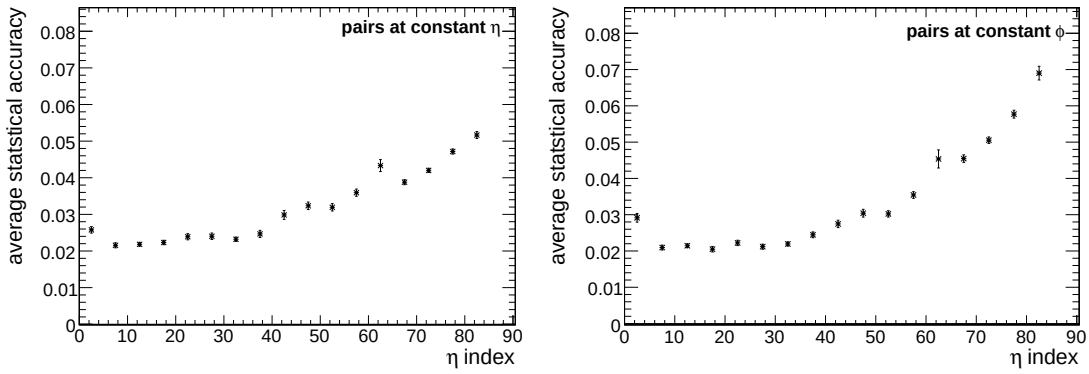

(a) Same η pairs (b) Same ϕ pairs

Figure 4.10: The statistical precision for the same η pairs is shown as a function of η in (a), and for the same ϕ pairs in (b).

of the RMS spread of the crystals in the seven supermodules.

$$\frac{\frac{C_{single}}{\sigma^2_{single}} + \frac{C_{\eta\ pairs}}{\sigma^2_{\eta\ pairs}} + \frac{C_{\phi\ pairs}}{\sigma^2_{\phi\ pairs}}}{\frac{1}{\sigma^2_{single}} + \frac{1}{\sigma^2_{\eta\ pairs}} + \frac{1}{\sigma^2_{\phi\ pairs}}} \tag{4.5}$$

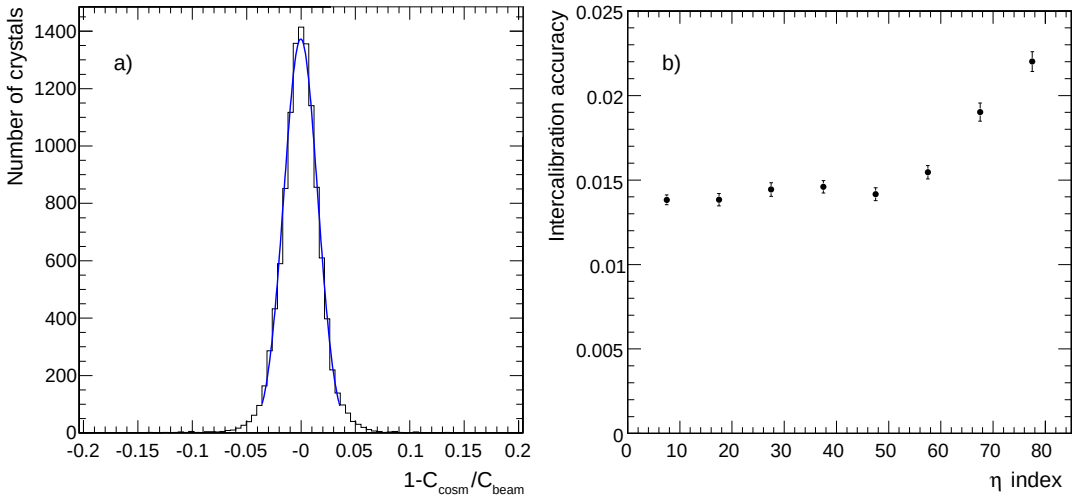

Figure 4.11: The comparison of cosmic ray determined calibration constants and those determined from precision electron test-beam constants are shown in a). The precision as a function of η index as the RMS averaged of η rings shows a calibration of 1.4% for low η and 2.2% for high η are shown in b).

4.2.3 Test-Beam Intercalibration

One quarter of the barrel supermodules were exposed to high energy electron test-beams. Five were exposed to 90 GeV electrons and four were exposed to 120 GeV. Detailed position information was used to determine the location of the impinging electron. This information was used to correct the normalized energy for utilizing a single crystal technique. A separate 5×5 matrix technique was used to verify the constants. The statistical accuracy was determined to be 0.2% by comparing two independent datasets for the same supermodule under the same conditions. Systematic uncertainty was determined from reproducibility and linearity Figure 4.12. The reproducibility was determined to be

0.3% by comparing the constants in an individual supermodule separated by one month. The linearity was determined to be 0.15% by comparing intercalibration constants from 90 GeV to those from 120 GeV [52].

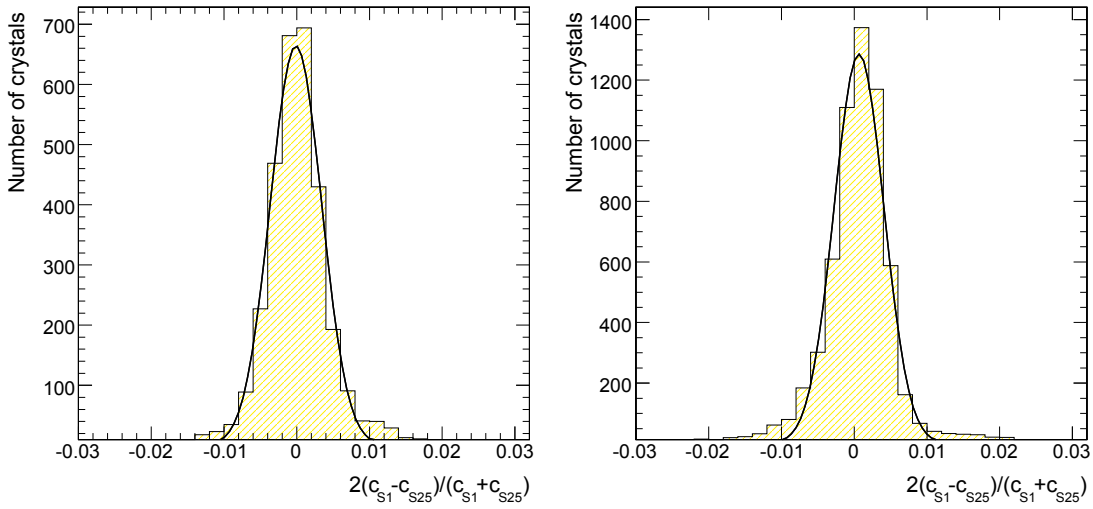

Figure 4.12: The comparison of test-beam determined calibration constants from August to September on the same supermodule is shown on the left. The linearity systematic by comparing 90 GeV to 120 GeV intercalibrations is shown on the right[52].

4.3 ECAL *in situ* Calibration

Multiple methods were used *in situ* to cross-check, track and monitor the intercalibrations. For daily and weekly calibration monitoring and for the low energy order GeV scale π^0's and η's are used. The π^0 rate was sufficient such that with order of one day of nominal startup luminosity to get 1,000 photons per crystal. For the intermediate scale ϕ symmetry is used. For the calibration with the 2010 dataset $Z \rightarrow e^+e^-$ and $W \rightarrow e\nu$ are used. These two calibration methods are best for electrons from 20 to 90 GeV.

4.4 HF Calibration

The HF wedges were tested with 30, 50, 100, and 150 GeV electrons. The linearity of the long fibers was found to be within 2% across the energy range and the short fibers varied by about 15% relative to the long fiber scale. The non-linearity of the short fibers was due to the length of steel in front of the short fibers. This is also shown in Figure 4.13 with the pion response as normalized to the electron response. The pions also show a non-linearity.

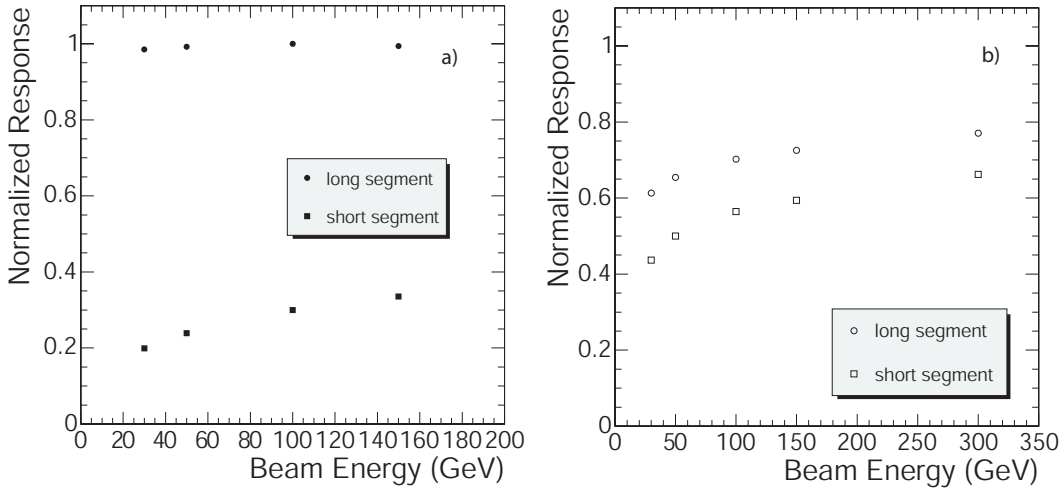

Figure 4.13: The comparison of long and short fiber response for electrons and pions. The pion response was normalized to the electron response. and those determined from precision electron test-beam constants are shown in a). The precision as a function of η index as the RMS averaged of η rings shows a calibration of 1.4% for low η and 2.2% for high η are shown in b)[49].

HF calibration utilized a 100 GeV electron beam. The calibration was such that the sum of all the long fibers in a tower equaled the beam energy. The *in situ* HF calibration was monitored using a ^{60}Co source mounted wire in up to 11 m tubes between HF fibers. The gamma rays create Compton electrons energetic enough to create Cherenkov photons. These calibrations were then normalized to the beam determined calibrations. The HF calibration were normalized in rings of η with 2010 $Z/\gamma* \rightarrow e^+e^-$ data.

Chapter 5

Data Analysis Strategy

The measurement was designed to probe the differential cross-section of the Z as a function of the rapidity (y) of the Z. The full NLO inclusive cross-section was described in Equation 2.21. The rapidity of the Z is defined in Equation 5.1 where p_ℓ is the longitudinal momentum of the Z boson candidate along the z axis of the detector.

$$y = \frac{1}{2} \ln \frac{E + p_\ell}{E - p_\ell} \tag{5.1}$$

This chapter serves as an overview of the analysis strategy. Subsequent chapters will provide further detail on object reconstruction and selection (Chapter 6), efficiency determination (Chapter 7), and the full results from data (Chapter 8).

5.1 Measurement Methodology

This measurement was designed to maximize the use of the data itself to determine resolution and efficiency. Single-electron efficiencies were determined from data and convolved using a fast Monte Carlo method with smearing parameters which were also tuned to the data. Two different versions of the results were tabulated. One version corrected for smeared resolutions and FSR by an average response and another by using an unsmearing matrix. For the result which was corrected for the average expected resolution effects, Equation 5.2 was evaluated.

$$\frac{1}{\sigma} \frac{d\sigma(\mathrm{Z}/\gamma* \to \mathrm{e}^+\mathrm{e}^-)}{dy_i} = \frac{(\epsilon \times A)}{N - B} \cdot \frac{(N_i - B_i)}{\Delta_i (\epsilon \times A)_i^{\mathrm{true}\, y}} \tag{5.2}$$

where $(\epsilon \times A)_i^{\text{true}\,y}$ was defined as the ratio between events finally selected in the bin and events which had a rapidity within the bin at generator level (before smearing).

In the case of the use of the unsmearing matrix, Equation 5.3 was evaluated.

$$\frac{1}{\sigma}\frac{d\sigma(\mathrm{Z}/\gamma* \to \mathrm{e}^+\mathrm{e}^-)}{dy_k} = \frac{(\epsilon \times A)}{N - B} \cdot \left[\sum_i M_k^i \cdot \frac{(N_i - B_i)}{\Delta_i(\epsilon \times A)_i^{\text{meas}}}\right] \tag{5.3}$$

where M_k^i was the unfolding matrix for the full rapidity distribution and $(\epsilon \times A)_i^{\text{meas}}$ was defined as the ratio between events finally selected in the bin and events which had a rapidity within the bin after smearing but before selection.

In both expressions, N_i represented the number of Z candidates observed in data, B_i represented the estimated number of background candidates, and Δ_i represented the bin width.

5.2 Efficiency times Acceptance

To determine the total Z-boson efficiency as a function of Z rapidity the individual electron efficiencies had to be combined. The electron efficiencies were determined as functions of detector space and electron momentum directly from data using a "tag-and-probe" method of exploiting the Z mass constraint—as described in Chapter 7. The $(\epsilon \times A)$ for each bin of rapidity was determined from the measured electron efficiencies by using POWHEG+PYTHIA Monte Carlo generated events. The generator-level quantities were smeared based on measured detector resolutions and positions. This convolution was a Monte Carlo assessment of Equation 5.4.

$$(\epsilon \times A)_{\mathrm{Z}}(y) = \int P\left(\eta_{d+}, \mathrm{p_{T+}}, \eta_{d-}, \mathrm{p_{T-}}; y\right) \epsilon_{e^+}\left(\eta_{d+}, \mathrm{p_{T+}}\right) \epsilon_{e^-}\left(\eta_{d-}, \mathrm{p_{T-}}\right) d\eta_{d+} d\mathrm{p_{T+}} d\eta_{d-} d\mathrm{p_{T-}} \tag{5.4}$$

where $P\left(\eta_{d+}, \mathrm{p_{T+}}, \eta_{d-}, \mathrm{p_{T-}}; y\right)$ was the probability density function for electrons with the given η_{d} and $\mathrm{p_T}$ values for a Z with the given y and included the effect of acceptance. The $\epsilon_e\left(\eta_{\mathrm{d}}, \mathrm{p_T}\right)$ function represented the total efficiency for an electron with the given detector position and momentum.

5.3 Uncertainty Sources

In order to assess the validity of the measurement, different possible sources of uncertainty were explored. Contributions to each of the terms in Equations 5.2 and 5.3 were examined. The largest errors were expected to arise from statistically limited elements of the data. The following sources of measurement uncertainty were considered as part of this analysis:

1. The statistical errors on the individual electron efficiencies used in the $(\epsilon \times A)$ calculation.
2. The correlated systematic errors on the individual electron efficiencies used in the $(\epsilon \times A)$ calculation.
3. The impact of the energy scale uncertainties and of the energy resolutions of the electromagnetic (ECAL) and forward (HF) calorimeters.
4. The impact of the final state radiation and finite detector resolution on rapidity reconstruction.
5. The impact of parton distribution function models.
6. The uncertainty inherent in the background subtraction.

5.4 Sensitivity Analysis

Finally, a sensitivity and power analysis was performed. This was done to highlight some of the orthogonal PDF vectors which could be constrained by this measurement.

Chapter 6

Event Selection

The proper selection of Z events in CMS began with the definition of electron identification parameters in the sub-detectors. The tracker provided charge and momentum coverage for the central electrons and thus one electron was required to be central and associated with a track. Through exploting a windor around the mass of the Z, a second electron was searched for and was allowed to be in either the ECAL or the HF. The central electron was also required to be associated with an electron trigger.

6.1 ECAL Electrons

ECAL electrons were selected if they were found within the η acceptance of the tracker ($|\eta| < 2.5$). The electrons were composed of superclusters of ECAL crystals. Superclusters combined crystal energy and position information into a single object defined by algorithms optimized for electron reconstruction and recovery of bremsstrahlung. A 5×5 matrix of crystals contained 97% of the energy of a typical photon or electron as it impacted the the calorimeter. The effects of bremsstrahlung resulted in a broadening of the energy deposition for an electron as it propagates from the collisions. The strategy for handling this is described below.

6.1.1 Barrel Superclusters

A dynamic hybrid reconstruction algorithm was used to build superclusters in the ECAL barrel. Starting from the highest E_T seed crystal, energy and positions were summed in

narrow strips of η (bars of 3 or 5 crystals) and long rows of ϕ. The longer rows of ϕ were required to recover the energy lost to bremsstrahlung in the tracker material. These photons generally appeared as isolated clusters in ECAL. Energy scale and containment corrections were applied to the superclusters, as a general function of the number of crystals within the cluster to represent the true particle energy.

6.1.2 Endcap Superclusters

In the ECAL Endcap, a 5×5 clustering algorithm was used. Simple 5×5 clusters were added together around seed 5×5 clusters by searching 0.3 rad in both ϕ directions to recover energy lost to bremsstrahlung. Energy scale corrections were applied as done for barrel superclusters. The final step in the superclusters creation was the addition of the ECAL preshower energy to the supercluster energy.

6.1.3 Track Matching

Two approaches were developed to match superclusters to tracks. Either the ECAL supercluster was used as the seed and the algorithm searched for hits in the tracker, or all tracks were used as the seeds which were then propagated and matched to superclusters. Combining both of these methods allowed for a very high tracking efficiency for isolated and jet contained electrons to low $\mathrm{p_T}$. Both tracker and ECAL seeds were used to define a loose tracking criteria where pattern recognition algorithms were used. The loss due to bremsstrahlung was modeled by using a sum of Gaussians in the tracking fitter–a so-called Gaussian sum filter (GSF). The track matching algorithm also calculated the combined electron object momentum and energy from the track and supercluster based on their respective resolutions.

ECAL seeds had a loose preselection of hadronic over electromagnetic energy ($H/E < 0.10$) and supercluster $E_T > 4$GeV to reject background. Further loose quality filters were used such as the minimum number of tracker hits required were 5, and only one hit was allowed to be missing. When the tracker driven electrons were included, there was a minimum $\mathrm{p_T}$ cut of 2 GeV/c. The final step was the removal of duplicate electrons. This included cases where the same supercluster defined more than one electron or the same track was shared. Arbitration was used such that the “best” possible combination

was chosen.

6.1.4 Isolation

Isolation values were calculated separately for tracker, ECAL, and HCAL. Each had an inner cone exclusion region and a hit noise cut. Accepted hits within a cone with a ΔR of 0.3 were added to the isolation sum. The ΔR is a radial value calculated between the two objects as shown in Equation 6.1.

$$\Delta R = \sqrt{(\Delta\phi)^2 + (\Delta\eta)^2} \tag{6.1}$$

Tracker isolation was calculated by summing the p_T of all the tracks above 1 GeV within a ΔR of 0.3 of the electron vertex. The tracks within the inner veto radius of 0.015 were not included in the sum. These cuts are summarized in Table 6.1.

Isolation cone	Inner radius	Threshold
$\Delta R < 0.3$	$\Delta R > 0.015$	track $p_T > 1$ GeV

Table 6.1: This table summarizes the tracker isolation cuts. Only tracks with enough energy to pass the threshold and within the isolation cone but outside the inner radius were included in the sum.

The isolation calculation in the ECAL was very similar. In addition to the inner and outer radii, crystals within a narrow strip of η were removed—called the Jurassic width. Individual crystal hits were used and the cuts were defined separately for the barrel and the endcaps as shown in Table 6.2.

	Isolation cone	Inner radius	Jurassic Width	Threshold
Barrel	$\Delta R < 0.3$	$\Delta R > 0.045$	$\Delta\eta > 0.02$	E > 0.08 GeV
Endcap	$\Delta R < 0.3$	$\Delta R > 0.070$	$\Delta\eta > 0.02$	E > 0.30 GeV

Table 6.2: This table summarizes the ECAL isolation cuts. Only electrons with enough energy to pass the threshold and within the isolation cone but outside the inner radius and Jurassic strip were included in the sum.

The isolation values in the HCAL were calculated from objects called CaloTowers. These objects basically summed the combined depths of the calorimeters into a single object. The reconstructed hit energy threshold cuts were applied to each HCAL depth individually. The HCAL was separated into two effective depths called Depth 1 and Depth 2. These depths were meant to have roughly the same thickness in interaction lengths and relate to the HCAL towers of from Figure 3.6 as shown in Table 6.3. The cut values for the HCAL isolation are shown in Table 6.4.

Effective Depth 1:	All in Towers 1-17, depth 1 Towers 18-29, depth 2 Towers 27-29
Effective Depth 2:	Depth 2 Towers 18-26, depth 3 Towers 27-29.

Table 6.3: This table summarizes the HCAL effective depths used in the HCAL electron isolation. They are a function of η represented by the actual HCAL depths and towers which are displayed in Figure 3.6.

	Isolation cone	Inner radius	Threshold
Barrel	$\Delta R < 0.3$	$\Delta R > 0.15$	E $>$ 0.9 GeV
Endcap	$\Delta R < 0.3$	$\Delta R > 0.15$	E $>$ 1.4 GeV

Table 6.4: This table summarizes the HCAL isolation cuts. Only electrons with enough energy to pass the HCAL reconstructed hit threshold and within the isolation cone but outside the inner radius were included in the sum.

6.1.5 Electron Identification

Four electron identification variables were used for ECAL electrons in this analysis. The first was a longitudinal shower discriminating variable called HoE. This represented the ratio of energy measured by the HCAL over the energy measured in the ECAL Equation 6.2. Only the HCAL towers directly behind the ECAL were considered in the energy measurement. This variable was effective at approximating the hadronic over electromagnetic component of the showers and therefore discriminating between true electrons and hadronic backgrounds—which tended to deposit a significantly larger

fraction of energy in the HCAL.

$$HoE = \frac{E_{HCAL}}{E_{ECAL}} \tag{6.2}$$

Another shower shape variable was used to take advantage of the difference in the transverse shower shapes between electromagnetic and hadronic showers—hadronic showers tended to be much wider. This electron identification variable was labeled $\sigma_{i\eta i\eta}$. This second central moment was chosen because the electrons have a very minimal width in the η direction as the bremsstrahlung in the magnetic field spreads in the ϕ direction. The definition of $\sigma_{i\eta i\eta}$ is shown in Equation 6.3 where $\eta_i^{N,cryst}$ represents the integer number of crystals the ith crystal was away from the seed crystal in the η direction. The log weights w_i were defined as in Equation 6.4 and $\bar{\eta}_{5\times5}$ was the mean weighted η position of the 5×5 using the same weights. The scale factors introduced were such to equate the $\sigma_{i\eta i\eta}$ to the previously studied $\sigma_{\eta\eta}$—which would artificially increase near ECAL cracks. The net result of a 0.01 $\sigma_{i\eta i\eta}$ cut was the requirement that approximately 90% of the electron energy was within two crystals in η from the center of the 5×5 cluster around the seed crystal. This tight electron width restriction rejected the much wider hadronic jets.

$$\sigma_{i\eta i\eta} = \sqrt{\frac{\sum_i^{5\times5}(\eta_i^{N,cryst} \times 0.0175 + \eta^{seed} - \bar{\eta}_{5\times5})^2 \times w_i}{\sum_i^{5\times5} w_i}} \tag{6.3}$$

$$w_i = 4.2 + \ln \frac{E_i}{E_{5\times5}} \tag{6.4}$$

The two final electron identification variables used in this analysis suppressed fake electrons by comparing tracker determined position quantities to ECAL determined values. This approach rejected hadronic backgrounds which tended not to propagate through the tracker as pure electrons would. The $\Delta\phi$ ($\Delta\eta$) are the $\phi(\eta)$ differences between the supercluster and the extrapolated track positions assuming no bremsstrahlung.

$$\Delta\phi = \phi_{supercluster} - \phi_{tracker} \tag{6.5}$$

$$\Delta\eta = \eta_{supercluster} - \eta_{tracker} \tag{6.6}$$

6.1.6 Identification Working Points

The conversion rejection, isolation, and electron identification cuts were combined into different electron definitions which were referred to as Working Points. The Working Point cuts are listed in Table 6.5. The cuts for the Working Points were applied to the GSF Electron object—the supercluster and track combined object.

Cut	WP95 EB	WP95 EE	WP80 EB	WP80 EE
Conversion				
Missing hits $\leq$	1	1	0	0
Dist	N/A	N/A	0.02	0.02
$\Delta cot\theta$	N/A	N/A	0.02	0.02
Isolation				
trackIsolation	0.15	0.08	0.09	0.040
ecalIsolation	2.0	0.06	0.07	0.050
hcalIsolation	0.12	0.05	0.10	0.025
Electron Id				
$\sigma_{i\eta i\eta}$	0.01	0.01	0.01	0.01
$\Delta\phi$	0.8	0.7	0.6	0.3
$\Delta\eta$	0.007	0.01	0.004	0.007
HoE	0.15	0.07	0.04	0.025

Table 6.5: The different electron identification and isolation criteria for the WP definitions. Unless otherwise noted, all objects below these cuts were accepted.

The Working Points were each optimized for an efficiency. For instance, the WP80 cuts were optimized for a electron efficiency of 80% while maximizing the background rejection in EWK and QCD Monte Carlo. This was achieved by incrementing small loses of efficiency against the cut which provided the most background rejection for the incremental lose. The set of cuts remaining after the efficiency was incremented to the desired value defined the Working Point. More than 15 variables were studied but those selected had the most rejection power.

6.2 HF Electrons

The electron acceptance was extended to include the range between ($3.05 < |\eta| < 4.6$) by defining electrons within the forward hadronic calorimeter (HF). As described in Sections 3.4 and 4.4 the HF contained fibers of two lengths. The long fibers extended the full length of the HF and short ones started after 12.5 radiation lengths. The electromagnetic shower depth is proportional to the radiation length (1.76 cm in HF) and the hadronic shower depth is proportional to the interaction length (17 cm in HF). Thus electron identification was achieved as electromagnetic showers tended to have a much shallower shower depth. Therefore, the fraction of energy in the long fibers was much larger than the short fibers for electromagnetic showers compared to hadronic showers. Additional electron identification variables were defined based on the transverse shower shape.

6.2.1 HF Superclustering

HF superclusters were formed as 5×5 clusters around the highest energy seed towers. Only towers with energy above 5 GeV E_T were considered as either seeds and 5 GeV E to contribute energy towards the supercluster. The reconstructed energy of the supercluster was defined as the 3×3 sum of the energies in the long fibers. The supercluster core was defined as the seed energy plus the energy of the next highest tower which had more than 50% of the seed energy. The supercluster position was calculated based on the log energy weighted positions of the included towers.

The reconstructed energy and positions of the supercluster also contained Monte Carlo corrections. The η position was corrected for the fact that the HF was aligned in the z direction rather than with a projective geometry. When the position was close to a cell edge or center, the reconstructed position was corrected with a sinusoidal function to reflect true positional variance. This was due to the fact that electromagnetic showers can have such a narrow width that they fit mostly within single tower. An energy correction factor was used given that the default HF calibrations were scaled for jets with calibration assumption that the long and short fibers are equally weighted in jets.

6.2.2 HF Electron Identification

The guiding principle in HF electron identification was that electromagnetic particle shower depths are shallower and shower widths were narrower than hadronic particles. Three types of cuts were applied.

Isolation: The ratio of the 3×3 energy to the 5×5 energy ($E_{9/25}$).

Longitudinal Shape: The ratio of the 3×3 energies of the short and long fibers ($E_{s/l}$).

Transverse Shape: The ratio of the core energy to the 3×3 energy ($E_{C/9}$).

The isolation variable (Equation 6.7) rejected the very broad signatures which were generally jets. Requiring a high $E_{9/25}$ forced the objects to be relatively isolated. The longitudinal shape variable (Equation 6.8) tended to focus closer to zero as most of the energy was deposited in the long fibers, with a high likelihood to be between 0.2-0.3. Hadronic values tended towards $E_{s/l} = 1.0$ as the long and short fibers shared roughly equal energies. The transverse shape variable (Equation 6.9) tended towards one for electromagnetic particles as most of the energy was deposited in the core due to the narrow shower shape. To greatly increase the significance of the S/B for the shower shape cuts, a 2-dimensional cut was used. This cut (C_{2D} in Equation 6.10) allowed for a high efficiency.

$$E_{9/25} = \frac{\sum_i^{3\times3} L_i}{\sum_i^{5\times5} L_i} \quad (6.7) \qquad E_{s/l} = \frac{\sum_i^{3\times3} S_i}{\sum_i^{3\times3} L_i} \quad (6.8) \qquad E_{C/9} = \frac{\sum_i^{Core} S_i}{\sum_i^{3\times3} L_i} \quad (6.9)$$

$$C_{2D} < E_{C/9} - 1.125 \times E_{s/l} \quad (6.10)$$

The HF electron identification cuts were chosen based on Monte Carlo studies to provide optimal efficiencies. Final efficiencies were measured using data. Isolation was optimized to provide roughly an 85% efficiency for signal while only allowing about 60% of the background to pass. This Monte Carlo study used $Z/\gamma* \rightarrow e^+e^-$ as the signal and an EM enriched QCD as the background (Figures 6.1 and 6.2). The summary of HF Electron identification cuts are in Table 6.6

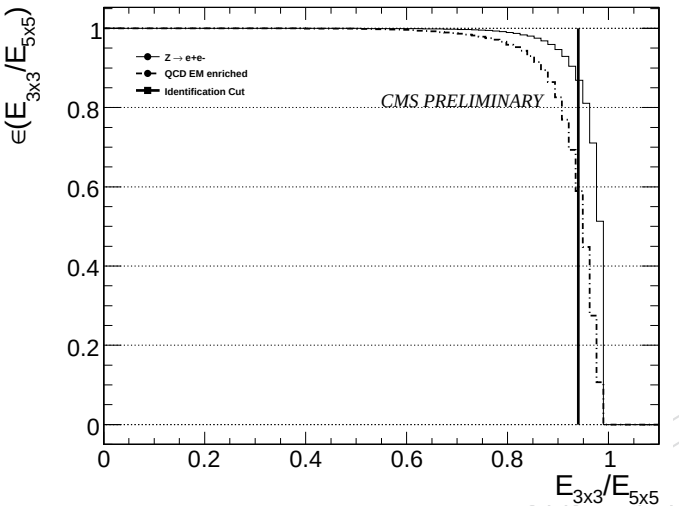

Figure 6.1: HF Isolation Monte Carlo efficiency curve for $E_{9/25}$. Signal as a solid line and background as a dashed line. The Isolation cut is represented by a solid vertical line. From [49].

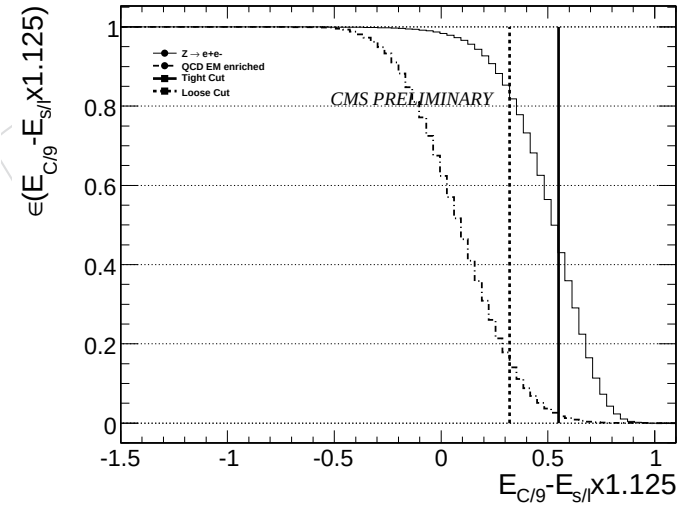

Figure 6.2: HF 2D Monte Carlo efficiency curve for C_{2D}. Signal as a solid line and background as a dashed line. The 2D cuts (loose–dashed, tight–solid) are represented by vertical lines. From [49]

Variable	$E_{9/25}$	C_{2D}
Cut	0.94	0.45

Table 6.6: This table summarizes the HF electron identification cuts used in this measurement.

6.3 Trigger Requirement

Only single electron triggers were considered in this analysis. The electron identification requirements on the online trigger objects were looser than the offline electron identification for the electron that is matched to the trigger object. The use of a single electron trigger also allowed for the selection of Z bosons which only had one electron within the tracking acceptance—with the other electron in the HF region—without having determine the efficiency of a second trigger.

Although the specific single electron trigger varied during the full dataset under consideration, the final offline electron electron identification requirements were tighter than each of the online trigger requirements. The benefit of this approach was only having to consider a single trigger efficiency for the entire time. The time varying triggers and rough integrated luminosity are summarized in Table 6.7. As the efficiencies were determined from data, time varying systematic effects from the HLT path were estimated. The electron supercluster E_T cut of 20 GeV was greater than the energy turn on for each of the triggers used in the measurement.

HLT Path	Luminosity	Electron Identification
HLT_SINGLE_ELE15_L1R	3 pb^{-1}	Type A
HLT_SINGLE_TightEID_ELE15_L1R	3 pb^{-1}	Type B
HLT_SINGLE_TightEID_ELE17_L1R	8 pb^{-1}	Type C
HLT_SINGLE_VeryTightEID_ELE17_L1R	22 pb^{-1}	Type D

Table 6.7: This table summarizes the HLT electron identification cuts used in this measurement. The details of the electron identification types are listed in Appendix B. All the types are looser than the WP80 electron identification cuts.

6.4 Z definitions

Now that the electrons have been defined, the next step was to define the Z bosons used in the measurement. Two different Z definitions were used for the differential rapidity analysis. These were named ECAL-ECAL and ECAL-HF as shown in Table 6.8 which represents the electron Working Points—electron identification cuts, as well as isolation and conversion rejection cuts if appropriate from Tables 6.5 and 6.5. All three definitions were completely independent due to the η selection ranges of the second electrons. Each definition required that the WP80 leg be matched to one of the single electron triggers from Table 6.7. Each electron was required to be have more than 20 GeV of E_T and be within the fiducial range of each Working Point.

Z Name	Electron 1	Electron 2
ECAL-ECAL	WP80 & HLT	WP95
ECAL-HF	WP80 & HLT	HF EID

Table 6.8: The different electron identification and isolation criteria for each type of Z selection. The first electron was always required to have passed the WP80 criteria and must be matched to one of the active single electron trigger objects.

The total geometrical acceptance of the analysis is shown in Figure 6.3. The expected $d\sigma/dy$ distribution is shown for reference as well, indicating that this measurement, including the electrons which impact the HF, covered nearly the full rapidity range for Z bosons produced in pp collisions at $\sqrt{s}$ =7 TeV.

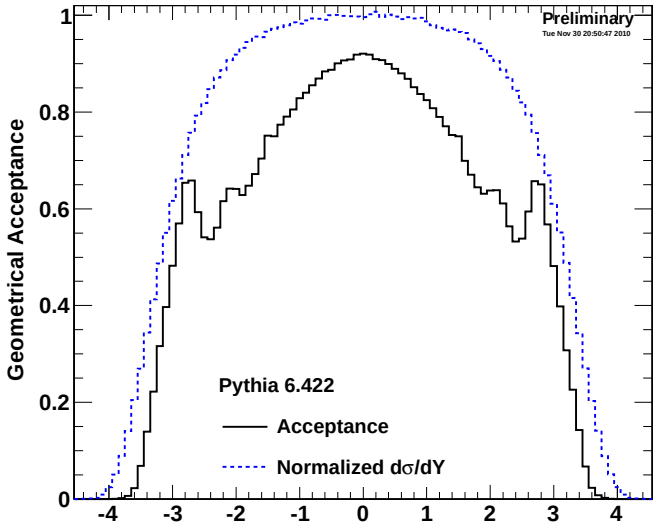

Figure 6.3: Analysis acceptance for $pp \rightarrow \mathrm{Z}+X \rightarrow e^+e^-+X$ as a function of the rapidity of the Z boson. The normalized cross-section distribution is shown for reference.

Chapter 7

Single Electron Efficiencies

An important aspect of the measurement methodology was the measurement of the efficiency of the reconstructed Z bosons. The efficiency of the Z was a convolution of the efficiencies of the individual constituent electrons. The efficiency had to be determined for each rapidity bin as each bin sampled a different sub-set of electrons with different detector positions (η) and energies (p_T). Therefore, to properly understand the total Z efficiency of each rapidity bin, the individual efficiencies for triggering, identification and reconstruction of electrons within the detectors had to be well understood as a function of η and p_T.

7.1 Electron efficiency factorization

The efficiency of electron reconstruction was partitioned into several contributions which were measured in sequence. The sequence was different for each electron type because of different requirements. For the ECAL electrons, the first term was the number of electrons which create superclusters. Next, the number of superclusters matched to tracks, and then those which passed electron identification and isolation requirements as shown in Equation 7.1. For HF electrons the sequence was similar, without any track matching requirements and different identification cuts as shown in Equation 7.2. Each efficiency was measured with respect to the previous step.

$$\epsilon_{\text{offline}} = \frac{\text{N(Superclusters)}}{\text{N(Electrons)}} \times \frac{\text{N(Track matched)}}{\text{N(Superclusters)}} \times \frac{\text{N(Isolated)}}{\text{N(Track matched)}} \times \frac{\text{N(Electron Id)}}{\text{N(Isolated)}} \tag{7.1}$$

$$\epsilon_{\text{hf}} = \frac{\text{N(HF Clusters)}}{\text{N(Electrons)}} \times \frac{\text{N(HF Electron Identification)}}{\text{N(HF Clusters)}} \tag{7.2}$$

The trigger efficiency (online) was determined with respect to to the offline ECAL efficiency as illustrated in Equation 7.3. It combined both the efficiency for for creating a Level 1 object (L1) and the efficiency for that object to pass the higher level trigger (HLT).

$$\epsilon_{\text{full}} = \epsilon_{\text{offline}} \times \frac{\text{N(L1 + HLT)}}{\text{N(offline)}} \tag{7.3}$$

7.2 Efficiency Method From Tag And Probe

The efficiencies of individual electrons were determined via the "tag-and-probe" method. This method has been used in multiple collider experiments [54]. The event selection was the full sample of $Z/\gamma* \rightarrow e^+e^-$ decays. The "tag" electron was selected to have passed the strictest identification requirements, and also to be associated with a single electron trigger. The requirement of an invariant mass of the combined tight "tag" electron and the "probe" electron near the Z mass provided a high purity sample of unbiased electrons for measuring individual efficiencies. Efficiencies were all determined considering the same acceptance as the selection, and the probe definition changed depending on the cut under study.

Each efficiency was determined for the invariant mass range of the selection 60 GeV/c^2 < M_{ee} < 120 GeV/c^2. For each efficiency calculation the dependent variables, invariant mass and if the object passes or fails the cut were stored. Three methods of background subtraction were employed to extract efficiencies as listed below in Sections 7.2.1, 7.2.2 and 7.2.3. Multiple methods were used to determine systematic effects in the data.

7.2.1 Linear Side Side Band Subtraction

For the linear side band subtraction method, one region below the mass range and another region above the mass range were used to extrapolate the background contribution in the signal region. The low mass and high mass regions were chosen such that there was less than 1% of the total signal within each region. To ensure this criteria, the region was defined as the first bin greater than 10 standard deviations of the Z width from the Z pole. Given the Z pole of $91.187\,\mathrm{GeV}/c^2$ and a Z width of $2.0\,\mathrm{GeV}/c^2$ the low mass range (LMR) was $40 - 60\,\mathrm{GeV}/c^2$ and the high mass range (HMR) was $120 - 140\,\mathrm{GeV}/c^2$.

Given a region lower invariant mass edge and a region higher invariant mass edge, and the binned invariant mass distribution m_{ee}, the average invariant mass ($\overline{m}_{ee}$) was defined in Equation 7.4 and the the average number of events ($\overline{n}$) in Equation 7.5.

$$\text{Average Invariant Mass } (\overline{m}_{ee}) = \frac{\sum_{i=region\ low\ edge}^{region\ high\ edge} m_{ee}[i] \times i}{\sum_{i=region\ low\ edge}^{region\ high\ edge} m_{ee}[i]} \tag{7.4}$$

$$\text{Average Number of Events } (\overline{n}) = \frac{\sum_{i=\text{region low edge}}^{region\ high\ edge} m_{ee}[i] \times i}{\sum_{i=region\ low\ edge}^{region\ high\ edge} i} \tag{7.5}$$

Each average was computed for the low mass region and for the high mass region. This resulted in the two points of Equations 7.6 and 7.7 representing a background correction line in slope point form as shown in Equation 7.8. The total number of background events were calculated by integrating this line over the analysis mass range $60\ \mathrm{GeV}/c^2 < M_{ee} < 120\ \mathrm{GeV}/c^2$.

$$P_1(\overline{m}_{ee_1}, \overline{n}_1) = \{\overline{m}_{ee}(\mathrm{LMR}), \overline{n}(\mathrm{LMR})\} \tag{7.6}$$

$$P_2(\overline{m}_{ee_2}, \overline{n}_2) = \{\overline{m}_{ee}(\mathrm{HMR}), \overline{n}(\mathrm{HMR})\} \tag{7.7}$$

$$n_{background} = \frac{\overline{n}_2 - \overline{n}_1}{\overline{m}_{ee_2} - \overline{m}_{ee_1}}(m_{ee} - \overline{m}_{ee_1}) + \overline{n}_1 \tag{7.8}$$

7.2.2 Exponential Side Band Subtraction

This procedure was similar to the linear side band subtraction of Section 7.2.1 but rather than computing a straight line between two points, the points of Equations 7.6 and 7.7 were used to compute an exponential background line. The invariant mass correction function was Equation 7.9 with the two parameters of Equations 7.10 and 7.11.

$$n_{background} = ae^{bm_{ee}} \tag{7.9}$$

$$b = \frac{\ln(\overline{n}_2/\overline{n}_1)}{\overline{m}_{ee_1} - \overline{m}_{ee_2}} \tag{7.10}$$

$$a = \overline{n}_1 e^{b\overline{m}_{ee_1}} \tag{7.11}$$

7.2.3 Maximum Likelihood Fitting

The side band subtraction methods were more robust for the early data conditions than the maximum likelihood fitting method. The regions were well defined and the subtraction was governed by counting and statistics. The maximum likelihood fitting method had more parameters and had a probability for fits to diverge in the very low statistics regime—both in the case of either very few passing and or very few failing events. The maximum likelihood fitting method contained the most accurate signal and background models and thus was used to understand the systematic effects due to background model assumptions especially in first efficiencies in the efficiency chains.

In this analysis the signal and background shapes were parameterized using the RooFit package within the ROOT [55] framework. The use of RooFit allowed automatic simultaneous fitting and PDF normalization. The signal was parameterized as a Voigtian—a resolution Gaussian convolved with the Z lineshape of a Breit-Wigner distribution. The background shape was parameterized as an exponential—to model background decay—and and error function—to model the kinematic turn-on.

Signal $V(x;\sigma,\gamma) = \frac{\mathrm{Re}[w(z)]}{\sigma\sqrt{2\pi}}$ where $z = \frac{x+i\gamma}{\sigma\sqrt{2}}$ and $w(z) = e^{-z^2}\mathrm{erfc}(-iz)$

Background $erfc(\alpha - x)\beta \times \exp^{-\gamma_b(x-\mu)}$ where $erfc(x) = \frac{2}{\sqrt{\pi}}\int_x^\infty e^{-t^2}\,dt$

7.3 Efficiency Binning

As described in the beginning of Chapter 7, the important variables for the binning of the efficiency were η and p_T of the electrons. Single electron efficiencies were measured in bins of these variables.

Most efficiencies were binned using both variables where neither p_T nor detector η was sufficient alone. For example in the supercluster creation and track matching efficiencies two-dimensional binning was performed. The efficiency bins are tabulated in Table 7.1.

Efficiency	Variable	Bins
WP95*	η	-2.5, -1.5, 0, 1.5, 2.5
	p_T	20, 30, 35, 40, 50, 120
HF	p_T	20, 30, 120

Table 7.1: The efficiency bins used in the analysis for all data efficiency steps. (*) represents WP95, WP80, GSF, and HLT efficiencies.

7.4 Single Electron Efficiencies

In order to provide the best estimate of efficiency and background, the background PDFs were determined based on QCD in data. This was achieved by inverting either the WP95 isolation or the WP95 electron identification cuts. Combining two of the selection-inverted objects provided extremely background rich templates. The background function of Section 7.2.3 was fit to each template. This was to provide smooth functions and eliminate any residual signal contamination. For the ECAL-HF electrons, the HF electron identification was also inverted. Then same procedure was performed. Some typical background shapes and the parametric fits are shown in Figures 7.1 and 7.2.

For the final efficiency fitting the signal shape was replaced with binned signal Monte Carlo templates. These were derived from a fast Monte Carlo with smearing parameters tuned to data as will be described in Section 8.1. The differences in efficiencies between

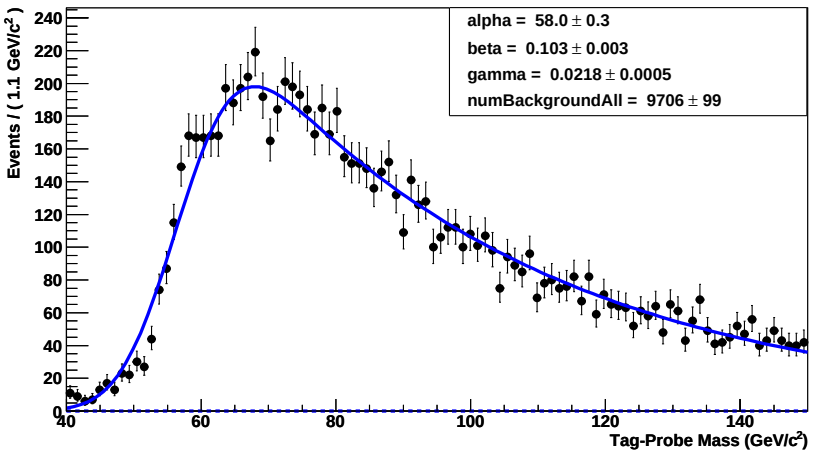

Figure 7.1: Example of the background function extrapolations from inverted templates in ECAL. For second electron energies between 35-40 GeV and (-2.5 > $\eta_{\rm d}$ > -1.5). The solid line represents the fitted function.

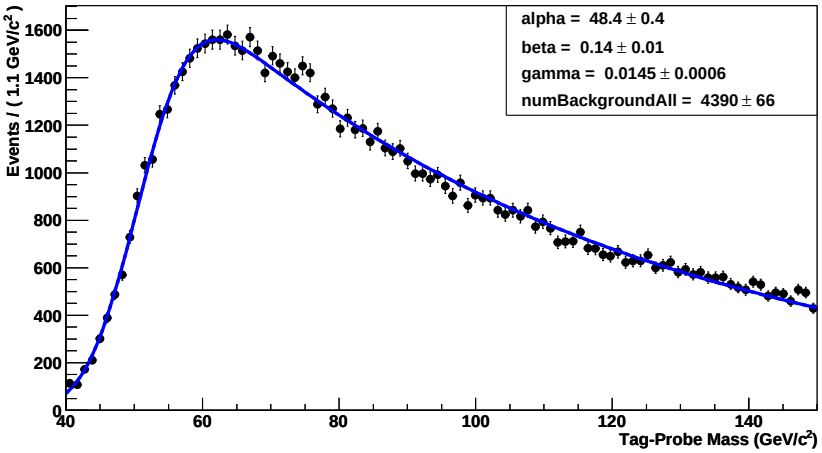

Figure 7.2: Example of the background function extrapolations from inverted templates with one electron in HF- with 20-30 GeV of energy. The solid line represents the fitted function.

the multi-parametric fit and the binned templates were within the systematic error estimates. The templates were used as they were more robust with finer binning. In the final fits there were only four parameters. The total number of signal events, the efficiency, the number of background events that fail the cut and the number of background events which pass the cut as displayed in two typical fits of Figures 7.3 and 7.4.

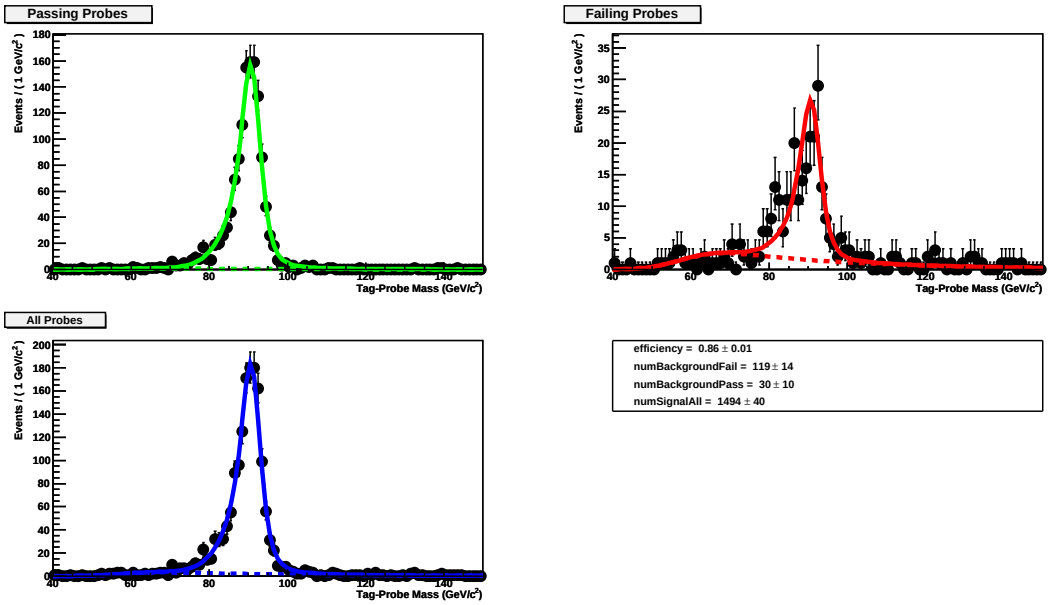

Figure 7.3: Example Tag and Probe efficiency fit for a bin in ECAL. For second electron energies between 35-40 GeV and (-2.5 $>$ $\eta_{\rm d}$ $>$ -1.5). The top left plot represents the probes which passed the cut. The failing probes are in the top right plot. All probes are in the bottom left plot. The fit parameters are in the bottom right frame. Dashed lines represent the background function and solid for the sum of signal and background.

The maximum likelihood fitting method was used to determine the electron efficiencies. The binning defined in Table 7.1 provided at minimum hundreds of events in which to calculate each efficiency. Only the Basyian statistical errors are displayed with the final efficiencies in Figure 7.5. Use of different signal and background shapes provided less variation than the uncertainty of the background estimate. Therefore, the systematic errors for each efficiency were assigned as the maximum efficiency variation possible due to all the background error between 80 GeV and 100 GeV.

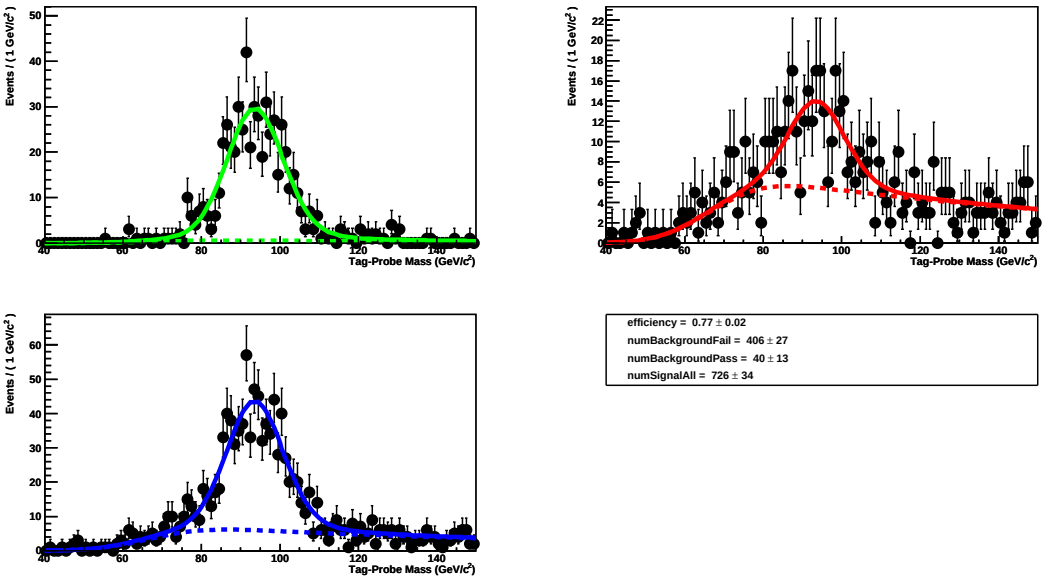

Figure 7.4: Example of the background function extrapolations from inverted templates with one electron in HF- with 30-120 GeV of energy. The top left plot represents the probes which passed the cut. The failing probes are in the top right plot. All probes are in the bottom left plot. The fit parameters are in the bottom right frame. Dashed lines represent the background function and solid for the sum of signal and background.

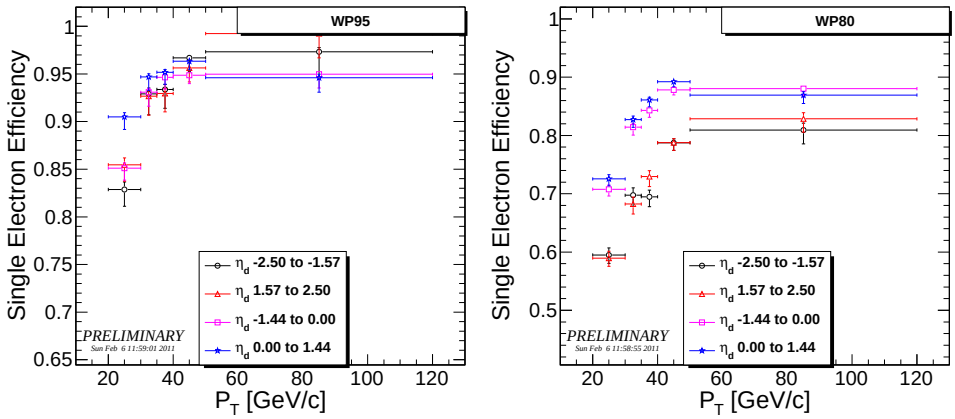

(a) WP95

(b) WP80

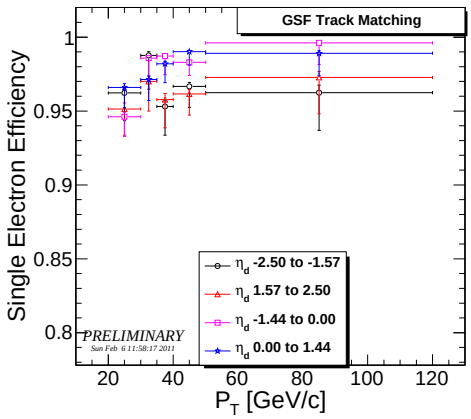

(c) GSF

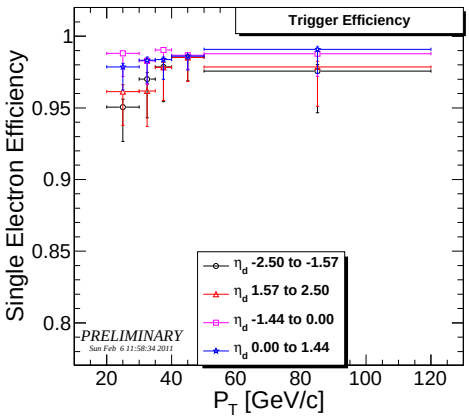

(d) HLT

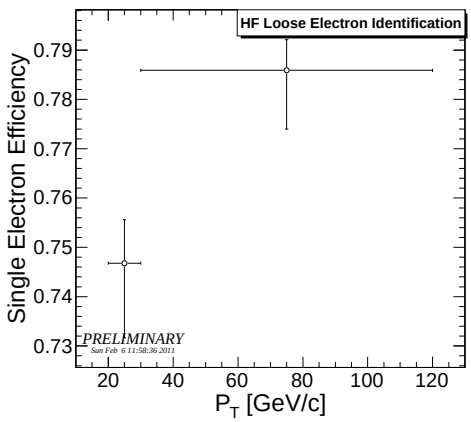

(e) HF EId

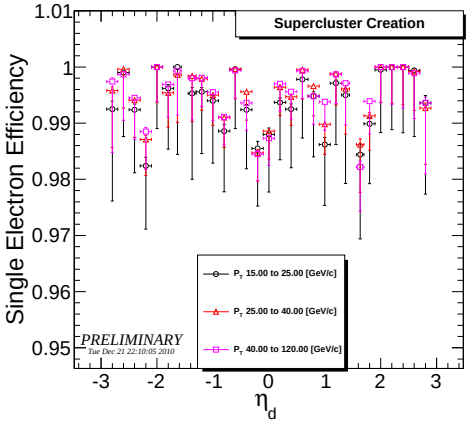

(f) SC

Figure 7.5: The single electron efficiencies given the binning of Section 7.3 and the full maximum likelihood fitting method.

Chapter 8

Analysis

With the single electron efficiencies measured the Z efficiencies could then be calculated. This allowed for a detailed calculation of the $(\epsilon \times A)$ through a convolution of the electrons. Additionally, the background contamination and then the final results were tabulated. Each major contributing systematic error was estimated.

8.1 Fast Monte Carlo

The analysis used a fast detector simulation to smear the Monte Carlo generator-level quantities based on optimization from data. The fast simulation was used to accurately determine the $(\epsilon \times A)$. The electron energy was taken as the Monte Carlo generated energy and a sum of electrons around a ΔR of 0.08 to simulate how the electron reconstruction algorithm collected FSR. The energies and positions were smeared based on expected functions from Monte Carlo studies and physical expectations. The parameters of the functions were determined by a least squares minimization of the resulting fast Monte Carlo mass distribution to the data mass distribution. The energy resolution functions are shown in Equation 8.1 and divided in major detector segments (EB, EE, HCAL).

$$\frac{\sigma_{EB}}{E} = c_{EB} \oplus \frac{a_{EB}}{\sqrt{E}} \cdot f_{EB}(\eta_d) \qquad \frac{\sigma_{EE}}{E} = \frac{a_{EE}}{\sqrt{E_T}} \cdot f_{EE}(\eta_d) \qquad \frac{\sigma_{HF}}{E} = \frac{a_{HF}}{\sqrt{E}} \oplus c_{HF} \quad (8.1)$$

$$\text{Where,} \quad f_i(\eta_d) = 1 - b_{1i}|\eta_d| + b_{2i}\eta_d^2 \quad (8.2)$$

For the HF, σ_{HF} represented the variance of a Gaussian with mean $\bar{x}_{HF}$. In order to model bremsstrahlung energy loss in the tracker material, σ_{EB} and σ_{EE} each represented the σ of a Crystal Ball functions which is defined in Equation 8.3.

$$g(x;\alpha,n,\bar{x},\sigma) = \begin{cases} \exp(-\frac{(x-\bar{x})^2}{2\sigma^2}), & \text{for } \frac{x-\bar{x}}{\sigma} > -\alpha \\ A\cdot(B-\frac{x-\bar{x}}{\sigma})^{-n}, & \text{for } \frac{x-\bar{x}}{\sigma} \leq -\alpha \end{cases} \tag{8.3}$$

$$\text{Where, } \; A = \left(\frac{n}{|\alpha|}\right)^n \cdot \exp\left(-\frac{|\alpha|^2}{2}\right) \qquad B = \frac{n}{|\alpha|} - |\alpha| \tag{8.4}$$

An example of the parameter variations is shown in Figure 8.1. The c parameter of the EB was varied and the resulting fast simulation mass distributions are shown overlaid the data mass distribution. The variation with the least squares compared to data is noted. All a, c, α and $\bar{x}$ parameters were determined using this method.

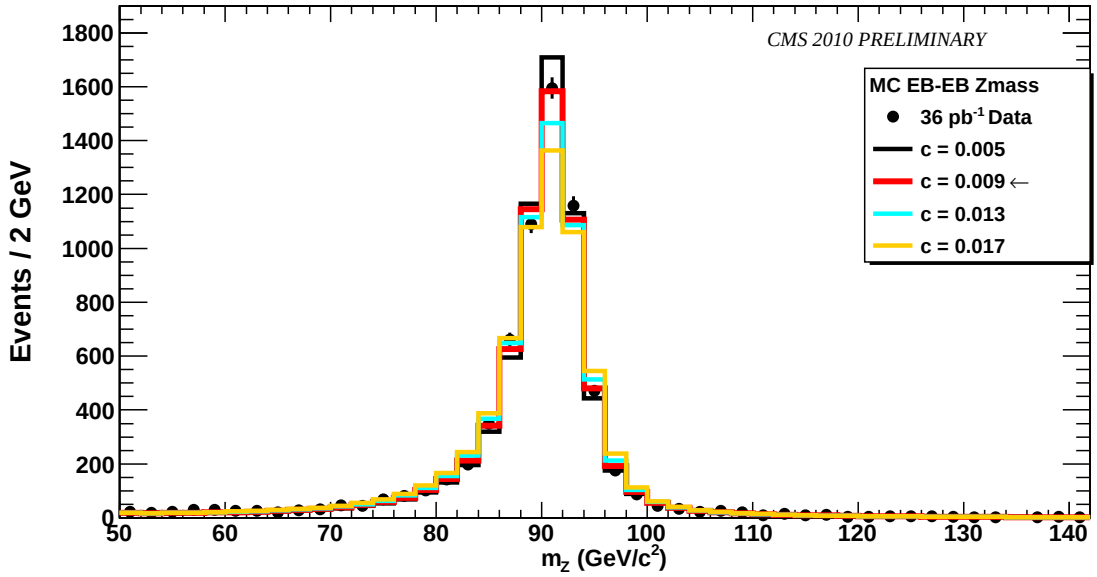

Figure 8.1: Example of smearing parameter variations for c in th barrel. Different colors represent each variation. The one with the least squares is shown with an arrow.

In order to extract a precise parametric value, the least squares versus parameter distributions were fit with a quadratic function using least squares regression in ROOT.

The minimum value was chosen as the optimal input. The fits of the minimization process can be seen in Figures 8.2 and 8.3. A full summary of each parameter and error can be found in Table 8.1.

Detector	$\bar{x}$	a [GeV$^{1/2}$]	α	c [GeV]
EB	1.0000 ± 0.0005	0.0410 ± 0.0019	1.386 ± 0.027	0.009 ± 0.0009
EE	0.9790 ± 0.0011	1.474 ± 0.067	1.635 ± 0.062	N/A
HF+	1.049 ± 0.0072	2.08	N/A	0.179 ± 0.011
HF-	1.0390 ± 0.0068	2.08	N/A	0.139 ± 0.012

Table 8.1: Fast Monte Carlo smearing parameters from least squares fitting for Equations 8.1 and 8.3.

The fast Monte Carlo must generate accurate results for the individual leptons as well as those for the Z. The individual lepton variables and combined variables had the effective efficiency times acceptance applied and were directly comparable to data. The comparisons can be seen in Figures 8.4 and 8.5. This validated the convolution process of Section 5.2.

8.2 Efficiency X Acceptance

The final result of the convolution process of Section 5.2 was the calculation of the final $(\epsilon \times A)$. The final $(\epsilon \times A)$ is displayed in Figure 8.6. The magnitude of each of the various cuts on the analysis can be seen in Figure 8.6a, while the contribution to the final $(\epsilon \times A)$ from the two separate Z definitions (ECAL-ECAL and ECAL-HF) can be seen in Figure 8.6b.

8.2.1 Bin Migration Correction Determination

The reconstructed rapidity of a di-lepton pair was not necessarily the rapidity bin at which the pair was produced originally, due to several physics and detector effects. The rapidity of a reconstructed Z can be changed if a photon from FSR was emitted by an electron at a large angle which then did not enter into the cluster. Several detector effects could have also altered the reconstructed Z rapidity, such as: the emission of

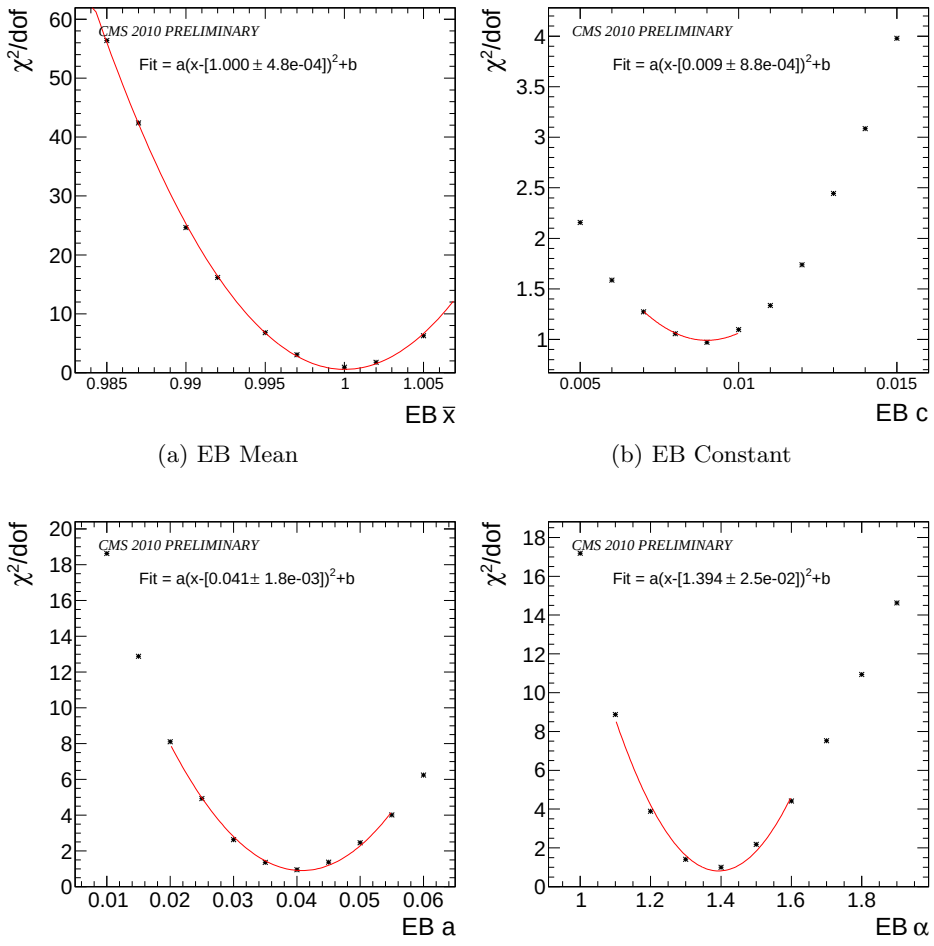

(a) EB Mean (b) EB Constant

(c) EB a (d) EB α

Figure 8.2: EB fits with mass least squares minimization. For the EB mean $\bar{x}$ in (a), the constant term in (b), the a term in (c), and the α parameter in (d). The minimized value and statistical errors from the fits are shown.

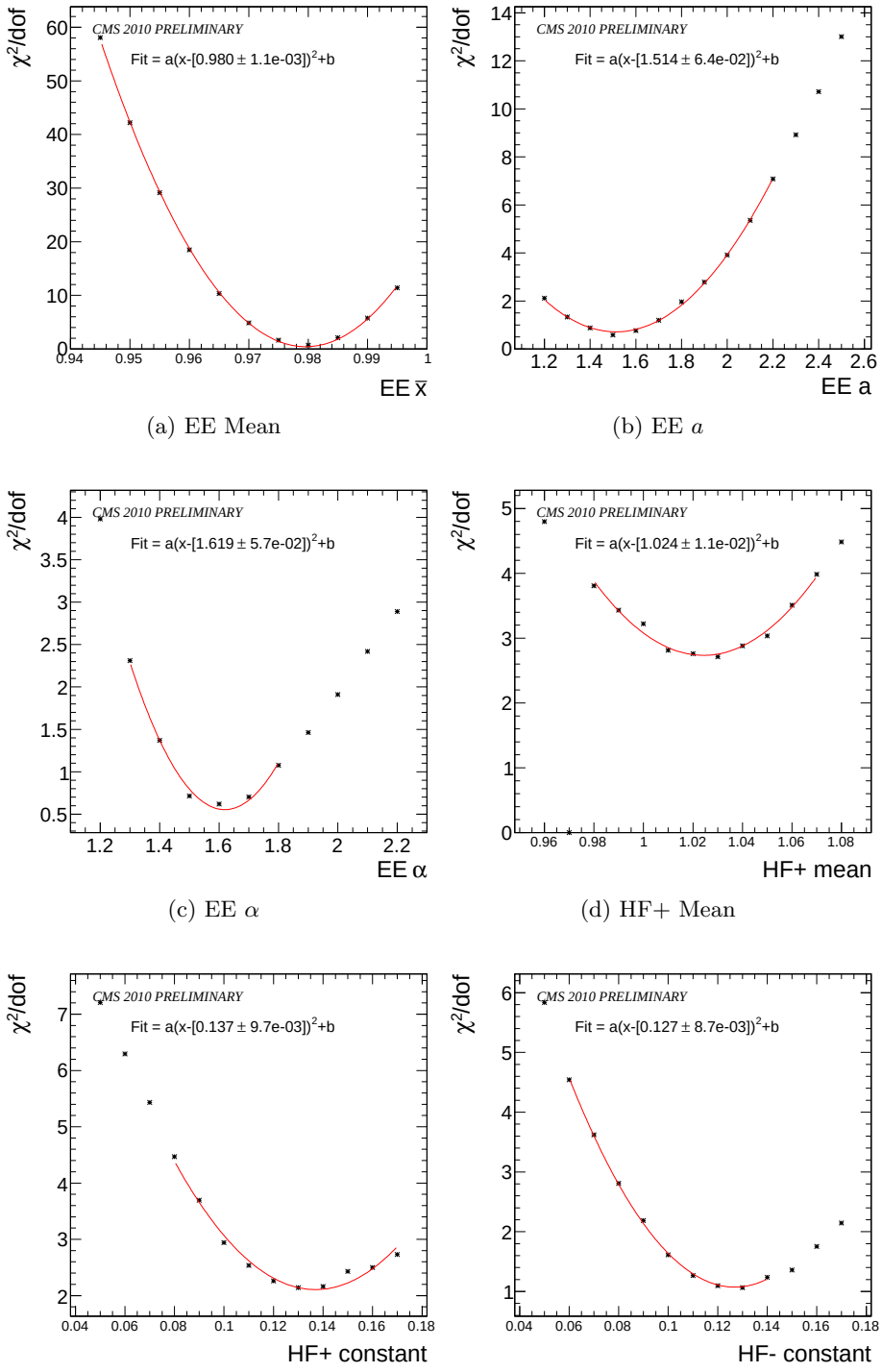

(a) EE Mean

(b) EE a

(c) EE α

(d) HF+ Mean

(e) HF+ Constant

(f) HF- Constant

Figure 8.3: EE and HF fits with mass least squares minimization.

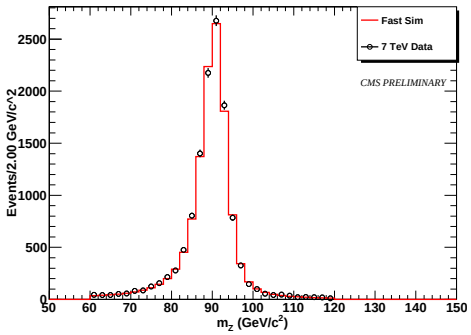

(a) Z Mass

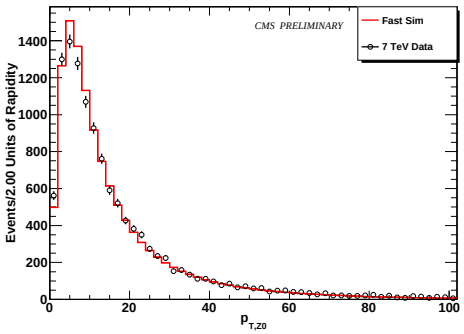

(b) Z p_T

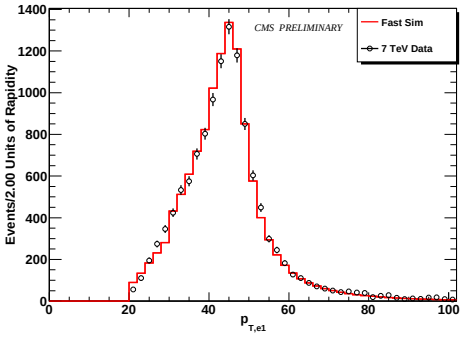

(c) Leading Electron p_T

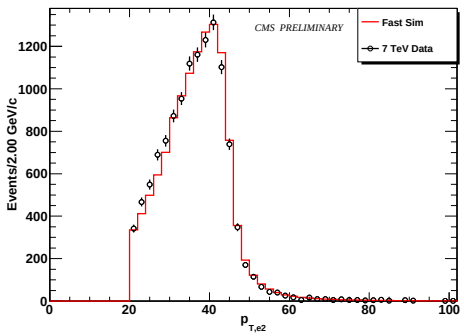

(d) Sub-leading Electron p_T

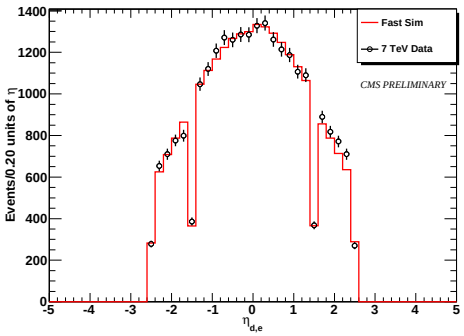

(e) Electron η

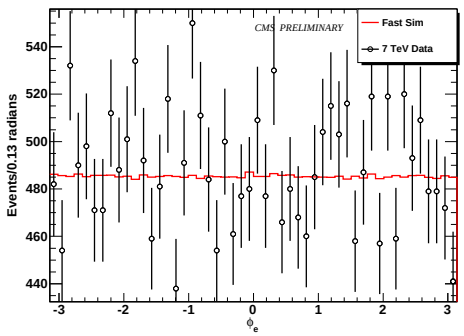

(f) Electron ϕ

Figure 8.4: The fast simulation is shown as a red line and data as black points for the ECAL-ECAL Z definition.

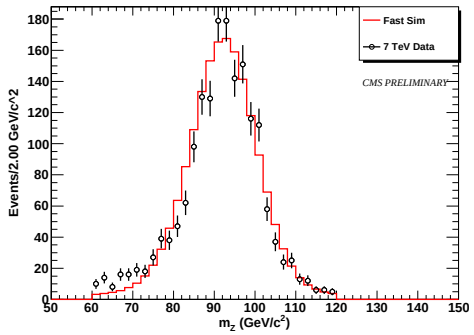

(a) Z Mass

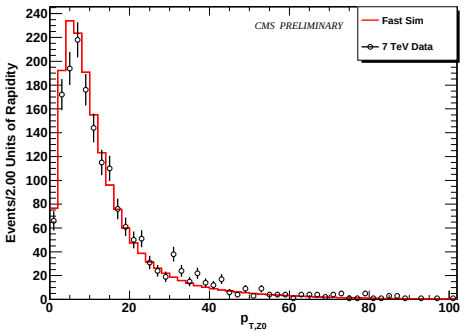

(b) Z p_T

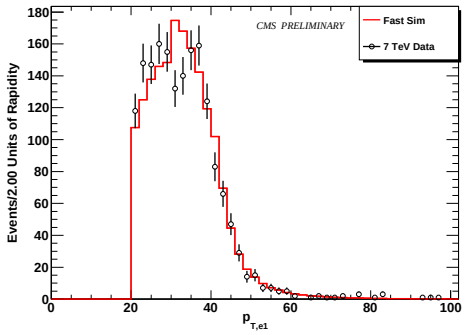

(c) ECAL Electron p_T

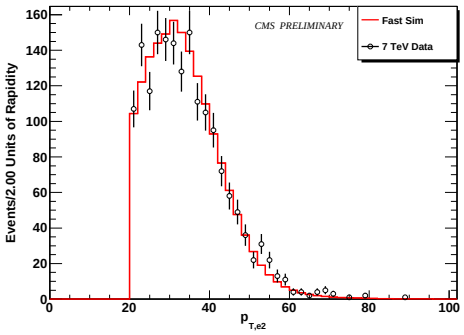

(d) HF Electron p_T

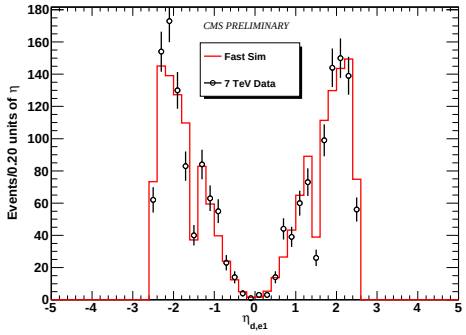

(e) ECAL Electron η

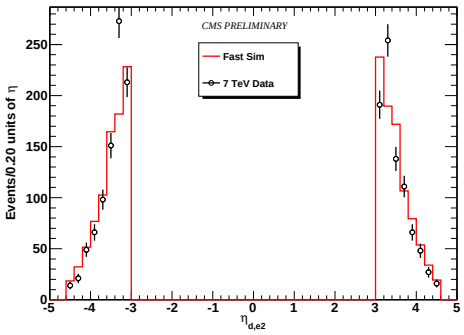

(f) HF Electron η

Figure 8.5: The fast simulation is shown as a red line and data as black points for the ECAL-HF Z definition.

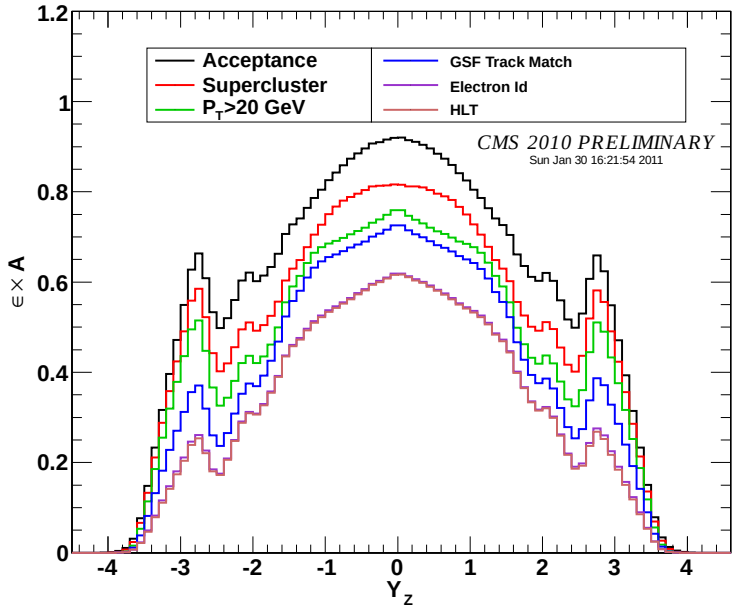

(a) Total ($\epsilon \times A$) after each successive cut in the selection sequence. At each stage, the indicated cut was applied to both electrons (some requirements, such as tracking, are not made on HF electrons).

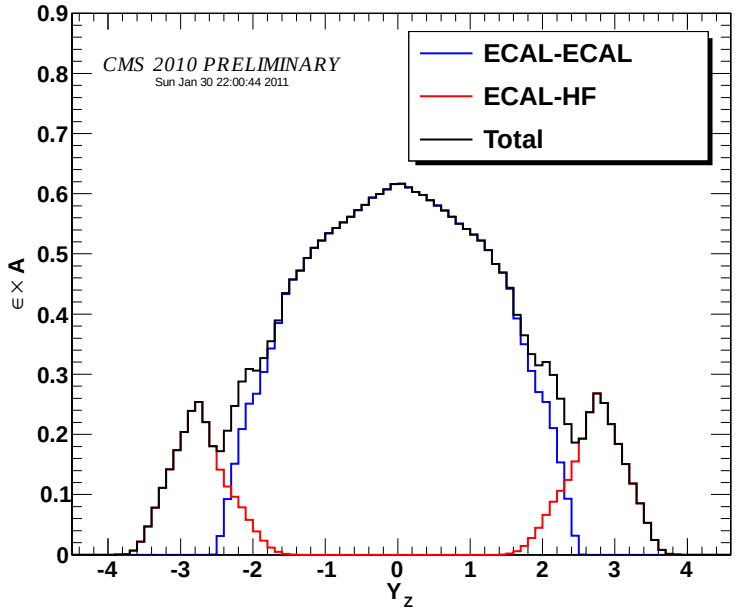

(b) Final ($\epsilon \times A$) showing the individual contributions of the ECAL-ECAL Z definition and the ECAL-HF definition.

Figure 8.6: The ($\epsilon \times A$) for the signal as determined by convolving the single electron efficiencies using the Monte Carlo distributions for Z electrons.

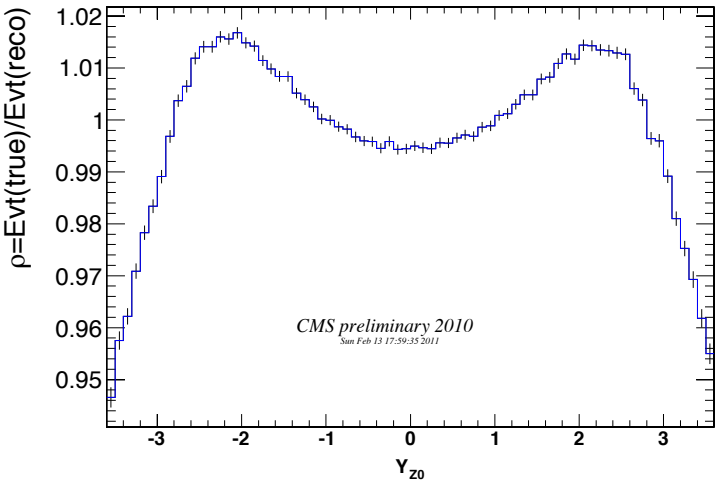

Figure 8.7: Relative effect ρ_i on the bin content due to the net bin migration as a function of rapidity. Statistical Monte Carlo errors only are displayed.

bremsstrahlung photons, the energy loss in the tracker as well as the intrinsic resolution of calorimeter energy and position measurements. If these effects acted unevenly across the the rapidity range covered by the measurement, this could have altered the rapidity spectrum by letting events migrate across the bins which were defined in Equation 5.3. The effect of the bin migration on the measurement was removed via an unfolding procedure which relied on the fast Monte Carlo.

Two different prescriptions were followed to unfold the final result. The one based on the average response, introduced in equation 5.2, relied on the ratios between the content of a rapidity bin before and after the smearing effects. True here means at generator level, prior to final state radiation and detector effects. This substitution effectively corresponded to multiplying the smeared distribution by the ratios:

$$\rho_i = \frac{(\epsilon \times A)_i^{\text{meas}}}{(\epsilon \times A)_i^{\text{true}\,y}} = \frac{\text{events in i-th bin at gen-level}}{\text{events in i-th bin after smearing}} \tag{8.5}$$

where each ratio was the effect of the net bin migration for each bin. The values of ρ_i are shown in Figure 8.7. The maximal variations were between $+2\%$ and -7% in the central-forward region.

The second prescription was based on the construction a migration matrix, defined

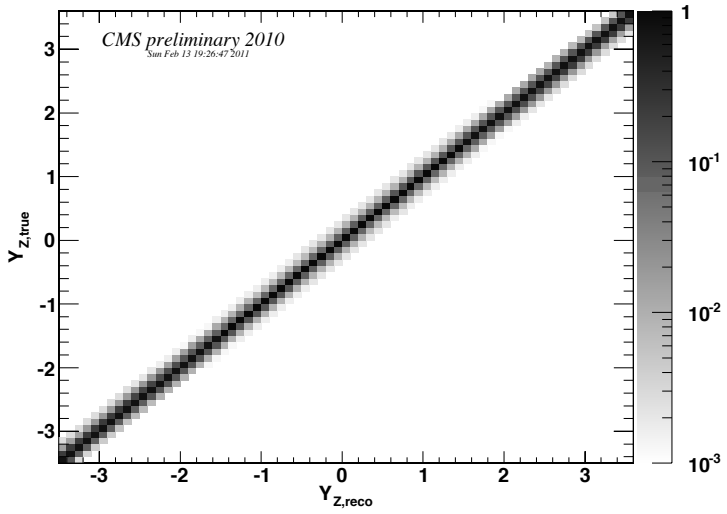

Figure 8.8: Graphical visualization of the migration between bins of the rapidity as a result of detector resolution and FSR effects.

as:

$$\mathrm{M}(i,j) = \mathrm{Prob}(y_{Z,\mathrm{reco}} \in \mathrm{j^{th}\ bin} | y_{Z,\mathrm{true}} \in \mathrm{i^{th}\ bin}) \tag{8.6}$$

This matrix accounted for all possible migrations and their relative importance, not just the net migration. The migration mostly occurred towards the nearest neighbor of each bin, hence the matrix was nearly diagonal. The net migration became more significant in the high $|y|$ region due to the intrinsically poorer resolution of the HF detector and also the larger slope of the distribution. The matrix is shown in graphical form in Figure 8.8 and the primary terms near the diagonal are given in tabular form in Table 8.2. The matrix $\mathrm{M}(i,j)$ was inverted to allow unfolding of the smearing in the full measurement, as per equation 5.3.

8.3 Background Subtraction

For each measurement bin the background had to be determined. The largest contribution was from QCD di-jets which each faked isolated electrons. The QCD contribution was determined directly from fits to each rapidity bin in the data. For background

$min(Y_i^{\text{true}})$	$max(Y_i^{\text{true}})$	Y_{i-2}^{reco}	Y_{i-1}^{reco}	Y_i^{reco}	Y_{i+1}^{reco}	Y_{i+2}^{reco}
-3.50	-3.40	1.26e-02	2.12e-01	6.66e-01	1.04e-01	2.90e-03
-3.40	-3.30	1.34e-02	2.16e-01	6.64e-01	9.94e-02	3.45e-03
-3.30	-3.20	1.46e-02	2.22e-01	6.59e-01	9.70e-02	3.98e-03
-3.20	-3.10	1.50e-02	2.26e-01	6.54e-01	9.70e-02	4.38e-03
-3.10	-3.00	1.56e-02	2.29e-01	6.50e-01	9.71e-02	4.84e-03
-3.00	-2.90	1.61e-02	2.30e-01	6.48e-01	9.70e-02	5.61e-03
-2.90	-2.80	1.69e-02	2.27e-01	6.48e-01	9.79e-02	5.71e-03
-2.80	-2.70	1.77e-02	2.21e-01	6.52e-01	9.83e-02	6.47e-03
-2.70	-2.60	1.78e-02	2.11e-01	6.61e-01	9.88e-02	7.10e-03
-2.60	-2.50	1.84e-02	2.01e-01	6.69e-01	9.96e-02	7.68e-03
-2.50	-2.40	1.85e-02	1.88e-01	6.81e-01	1.01e-01	8.36e-03
-2.40	-2.30	1.87e-02	1.74e-01	6.93e-01	1.01e-01	8.91e-03
-2.30	-2.20	1.79e-02	1.62e-01	7.04e-01	1.02e-01	9.35e-03
-2.20	-2.10	1.76e-02	1.51e-01	7.15e-01	1.03e-01	9.64e-03
-2.10	-2.00	1.65e-02	1.39e-01	7.27e-01	1.04e-01	9.78e-03
-2.00	-1.90	1.55e-02	1.27e-01	7.38e-01	1.05e-01	9.97e-03
-1.90	-1.80	1.45e-02	1.16e-01	7.51e-01	1.05e-01	9.96e-03
-1.80	-1.70	1.38e-02	1.05e-01	7.64e-01	1.04e-01	9.69e-03
-1.70	-1.60	1.26e-02	9.51e-02	7.75e-01	1.04e-01	9.23e-03
-1.60	-1.50	1.20e-02	8.66e-02	7.85e-01	1.03e-01	9.22e-03
-1.50	-1.40	1.11e-02	7.96e-02	7.93e-01	1.04e-01	8.70e-03
-1.40	-1.30	1.03e-02	7.33e-02	8.00e-01	1.03e-01	8.57e-03
-1.30	-1.20	9.50e-03	6.98e-02	8.04e-01	1.04e-01	8.52e-03
-1.20	-1.10	8.79e-03	6.75e-02	8.07e-01	1.04e-01	8.28e-03
-1.10	-1.00	8.23e-03	6.66e-02	8.09e-01	1.04e-01	8.08e-03
-1.00	-0.90	7.93e-03	6.67e-02	8.09e-01	1.03e-01	8.28e-03
-0.90	-0.80	7.66e-03	6.74e-02	8.09e-01	1.02e-01	8.37e-03
-0.80	-0.70	7.41e-03	6.87e-02	8.09e-01	1.01e-01	8.50e-03
-0.70	-0.60	7.11e-03	6.99e-02	8.10e-01	9.93e-02	8.50e-03
-0.60	-0.50	7.35e-03	7.17e-02	8.10e-01	9.67e-02	8.79e-03
-0.50	-0.40	7.33e-03	7.38e-02	8.11e-01	9.44e-02	8.73e-03
-0.40	-0.30	7.30e-03	7.59e-02	8.12e-01	9.05e-02	8.77e-03
-0.30	-0.20	7.68e-03	7.73e-02	8.12e-01	8.86e-02	8.54e-03
-0.20	-0.10	7.88e-03	7.90e-02	8.14e-01	8.55e-02	8.41e-03
-0.10	0.00	8.01e-03	8.12e-02	8.14e-01	8.28e-02	8.09e-03
0.00	0.10	8.32e-03	8.30e-02	8.14e-01	8.13e-02	8.10e-03
0.10	0.20	8.54e-03	8.58e-02	8.13e-01	7.89e-02	7.79e-03
0.20	0.30	8.62e-03	8.87e-02	8.13e-01	7.65e-02	7.59e-03
0.30	0.40	8.79e-03	9.13e-02	8.12e-01	7.53e-02	7.29e-03
0.40	0.50	8.87e-03	9.45e-02	8.11e-01	7.32e-02	7.11e-03
0.50	0.60	8.76e-03	9.67e-02	8.10e-01	7.18e-02	7.23e-03
0.60	0.70	8.65e-03	9.89e-02	8.10e-01	7.07e-02	7.21e-03
0.70	0.80	8.62e-03	1.01e-01	8.10e-01	6.87e-02	7.22e-03
0.80	0.90	8.46e-03	1.02e-01	8.09e-01	6.75e-02	7.35e-03
0.90	1.00	8.52e-03	1.03e-01	8.09e-01	6.64e-02	7.77e-03
1.00	1.10	8.46e-03	1.04e-01	8.08e-01	6.65e-02	8.35e-03
1.10	1.20	8.79e-03	1.04e-01	8.07e-01	6.70e-02	8.60e-03
1.20	1.30	8.77e-03	1.04e-01	8.04e-01	6.92e-02	9.27e-03
1.30	1.40	9.20e-03	1.04e-01	7.99e-01	7.31e-02	9.91e-03
1.40	1.50	9.60e-03	1.04e-01	7.93e-01	7.77e-02	1.09e-02
1.50	1.60	1.02e-02	1.05e-01	7.84e-01	8.50e-02	1.15e-02
1.60	1.70	1.07e-02	1.06e-01	7.74e-01	9.30e-02	1.27e-02
1.70	1.80	1.12e-02	1.07e-01	7.62e-01	1.02e-01	1.36e-02
1.80	1.90	1.18e-02	1.08e-01	7.49e-01	1.13e-01	1.45e-02
1.90	2.00	1.19e-02	1.08e-01	7.36e-01	1.24e-01	1.55e-02
2.00	2.10	1.22e-02	1.10e-01	7.24e-01	1.33e-01	1.66e-02
2.10	2.20	1.24e-02	1.09e-01	7.12e-01	1.45e-01	1.72e-02
2.20	2.30	1.21e-02	1.10e-01	7.00e-01	1.56e-01	1.79e-02
2.30	2.40	1.21e-02	1.09e-01	6.89e-01	1.67e-01	1.82e-02
2.40	2.50	1.14e-02	1.10e-01	6.76e-01	1.79e-01	1.83e-02
2.50	2.60	1.09e-02	1.10e-01	6.64e-01	1.92e-01	1.82e-02
2.60	2.70	1.02e-02	1.10e-01	6.55e-01	2.02e-01	1.79e-02
2.70	2.80	9.39e-03	1.11e-01	6.47e-01	2.11e-01	1.73e-02
2.80	2.90	8.68e-03	1.12e-01	6.42e-01	2.17e-01	1.67e-02
2.90	3.00	7.96e-03	1.13e-01	6.38e-01	2.21e-01	1.61e-02
3.00	3.10	7.54e-03	1.12e-01	6.40e-01	2.21e-01	1.56e-02
3.10	3.20	6.62e-03	1.11e-01	6.47e-01	2.17e-01	1.52e-02
3.20	3.30	6.09e-03	1.11e-01	6.51e-01	2.15e-01	1.41e-02
3.30	3.40	5.27e-03	1.14e-01	6.54e-01	2.10e-01	1.38e-02
3.40	3.50	5.01e-03	1.17e-01	6.57e-01	2.04e-01	1.36e-02

Table 8.2: Fraction of events which migrated from a given true (generator-level) bin to a given reconstructed bin. $y_{\pm 1}^{reco}$ were the nearest neighbor bins, $y_{\pm 2}^{reco}$ were the second nearest neighbor bins.

estimation of top-pair production and electroweak backgrounds, the standard full simulation Monte Carlo was used. The datasets used, with the cross-sections assumed, are given in Table 8.3. A detailed breakdown of each background in each bin is shown in Figure 8.9, with the ECAL-ECAL and ECAL-HF channels shown separately.

Process	Dataset	Events	Cross-section
$t\bar{t}$	/TTJets_TuneZ2_7TeV-madgraph-tauola/Fall10-START38_V12-v3	1164732	167 ± 24 pb
$Z \rightarrow \tau^+\tau^-$	/DYToTauTau_M-20_TuneZ2_7TeV-pythia6-tauola/Fall10-START38_V12-v1	2057446	1300 pb

Table 8.3: Full simulation samples used for background estimation.

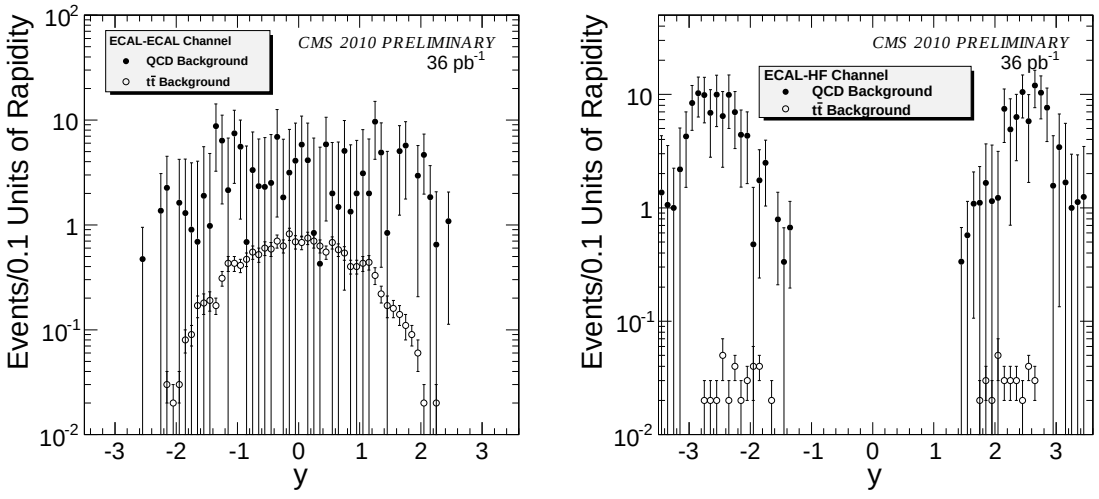

(a) Background in the ECAL-ECAL channel

(b) Background in the ECAL-HF channel

Figure 8.9: Background estimate by bin, broken down by contribution for ECAL-ECAL and ECAL-HF separately.

The QCD background was extracted from a fit to the dielectron mass distribution ($40\ \text{GeV}/c^2 < M_{ee} < 140\ \text{GeV}/c^2$). The estimated B_i was then subtracted from the total number of Z candidates (N_i) in the relevant bin. In order to obtain values for each B_i, the dielectron mass spectrum for each rapidity bin was fit to the sum of signal and background templates. The signal template for each bin was taken from the

parametrized Monte Carlo simulation while the background template, obtained from collision data, was modeled as in Section 7.2.3.

The parameters used for the background lineshape were determined from a QCD-enriched sample of events. As the QCD dielectron mass distribution was expected to be insensitive to electron identification and isolation requirements, the background-rich sample was obtained from data by inverting the selection requirements. The background templates were created using Z candidates formed by "electron" candidates that fail the nominal criteria:

- ECAL candidates that fail either WP95 identification or isolation requirements, or
- HF candidates that fail loose electron identification.

The background parameters were individually determined for each rapidity bin using the cut-inverted background templates. These parameters were then fixed for the background lineshape and combined the with the signal template in the nominal fit to estimate the background contribution in each rapidity bin. The uncertainty in the number of background events determined from each fit was taken as the systematic uncertainty. Example fits for bins with high and low statistics are shown in Figure 8.10 while all the fits are shown in Appendix C.

8.4 Result Systematics

8.4.1 Energy Scale Uncertainties

Systematic effects arising from energy scale uncertainties were greatly suppressed in the process of matching the fast Monte Carlo smearing to the data. However, in order to gauge the magnitude of the effect, the change in the $(\epsilon \times A)_i$ distributions resulting from a ± 1 % scale variation in the barrel ECAL, a ± 3 % scale variation in the ECAL endcap, and a ± 10 % scale variation in the forward calorimeter were computed.

Variations in the local energy scale were likely to correlate to absolute pseudorapidity $|\eta|$. To gauge the magnitude of a appraise the magnitude of systematic uncertainties which could arise from bias due to dose-dependent transparency in the ECAL crystals the following scales were varied:

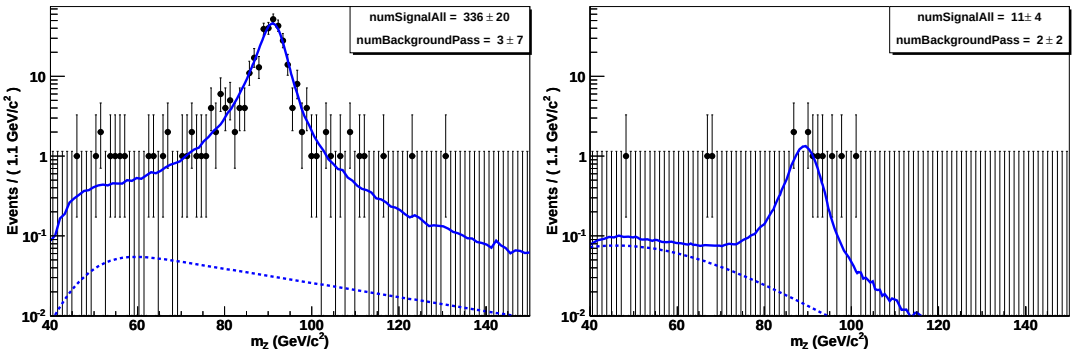

(a) ECAL-ECAL ($-0.3 > y_{Z0} > -0.2$)

(b) ECAL-ECAL ($2.4 > y_{Z0} > 2.5$)

(c) ECAL-HF ($-2.7 > y_{Z0} > -2.6$)

(d) ECAL-HF ($-2.0 > y_{Z0} > -1.9$)

Figure 8.10: Fits to the final binned mass distributions. The dashed line indicates the background template while the solid line indicates the sum of the background and signal templates. The relative scale factors were the only fit parameters. High statistics in the ECAL-ECAL case are shown in (a) and low statistics are shown in (b). Similarly for the ECAL-HF Z's, high statistics are shown in (c) and low statistics are shown in (d).

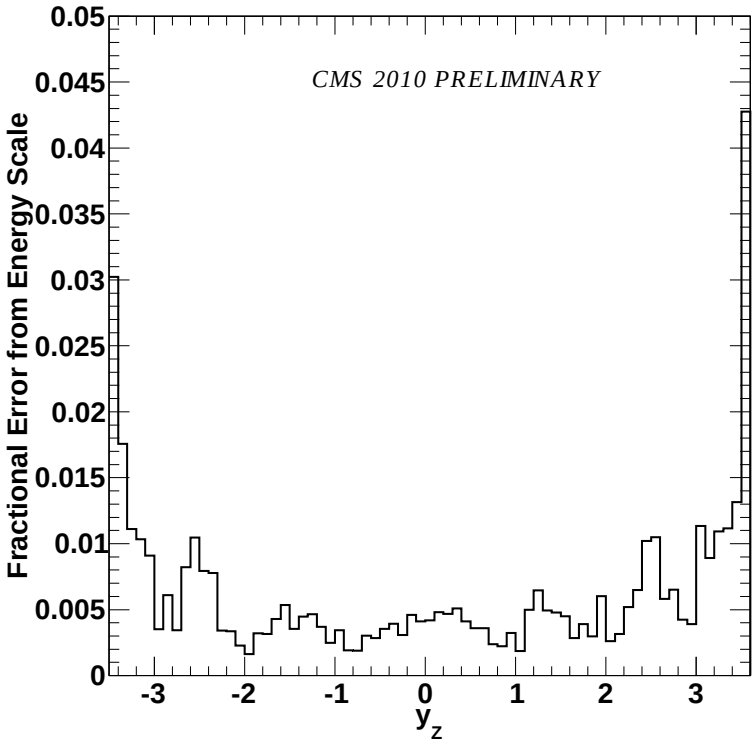

Figure 8.11: Systematic errors on the final distribution which were generated from absolute energy scale uncertainties in the various sub-detectors.

- ECAL barrel energies by $\pm 0.13\% \cdot |\eta|$

- ECAL endcap energies by $\pm(0.2 + 1.5 \cdot (|\eta| - 1.5))\%$

This provided a linear ECAL barrel variation to 0.2% and an additional 1.4% in the endcaps. The total effect of both scale variations summed in quadrature on the final observable are shown in Figure 8.11.

8.4.2 Parton Density Function Systematics

To better understand the behavor of the analysis under changes in the parton density functions, (PDFs), Equation 5.3 was arranged to better illustrate the PDF contributions

in Equation 8.7.

$$\frac{1}{\sigma}\frac{d\sigma(\mathrm{Z}/\gamma* \rightarrow \mathrm{e}^{+}\mathrm{e}^{-})}{dY_k} = \sum_i M_k^i \cdot \left[\frac{N_i - B_i}{N - B}\right] \cdot \left[\frac{(\epsilon \times A)}{\Delta_i(\epsilon \times A)_i}\right] \tag{8.7}$$

The PDF sensitivity was contained in the N_i/N term of Equation 8.7. Uncertainties in $(\epsilon \times A)_i$ and unfolding (M_k^i) terms due to possible PDF uncertainties were treated as systematic errors in the measurement. As changes to each of these terms could have enhanced or diminished the sensitivity, evaluating the systematic uncertainty provided an upper bound.

The lhapdf_5.8.4 [56] package was interfaced with POWHEG − BOXz. The full CT10w set of PDFs from the LHAPDF package were used. In the set, phase space of PDF variations were spanned by the base and twenty-six independent variation vectors, each with separate positive and negative directions.

Ten million $pp \rightarrow \mathrm{Z} + X \rightarrow e^{+}e^{-} + X$ with $\sqrt{s}$ of 7 TeV events were generated for each of four PDF variations. The re-weighting method [57] was used to generate event weights for all the other PDFs in the set, resulting in 40 million events for each PDF variation. Using the fast Monte Carlo of Section 8.1 $(\epsilon \times A)$ and M_k^i were calculated for each of 52 PDF variations.

For each PDF and each bin, a percentage difference of $(\epsilon \times A)$ with respect to the base PDF were obtained for each bin as shown in Figure 8.12. The positive and negative differences were caclulated separetly. The contrinbutions were added in quadrature to define a cumulative fractional difference in both directions.

$$\Delta x^{+} = \sqrt{\sum_{j=1}^{26}\left(\frac{X^{+,j} - X^{base}}{X^{base}}\right)^2}, \Delta x^{-} = \sqrt{\sum_{j=1}^{26}\left(\frac{X^{-,j} - X^{base}}{X^{base}}\right)^2}, \tag{8.8}$$

Here X was $(\epsilon \times A)$ and j was the index of the PDF variation. The base was defined as the median of the variations so there were twenty-six variations with larger and twenty-six variations with smaller values than the base.

For central values the difference was on the order of 0.1%. The effect was slightly larger for the highest $|y|$ values. The statistical error from the simulation sample was nearly identical to the measured PDF uncertainty, as displayed in Figure 8.12.

The definition of $(\epsilon \times A)$ included the bin migration ρ from Equations 8.5 and 8.7. This meant the effects of the PDFs were a combination of $(\epsilon \times A)$ and the fast Monte

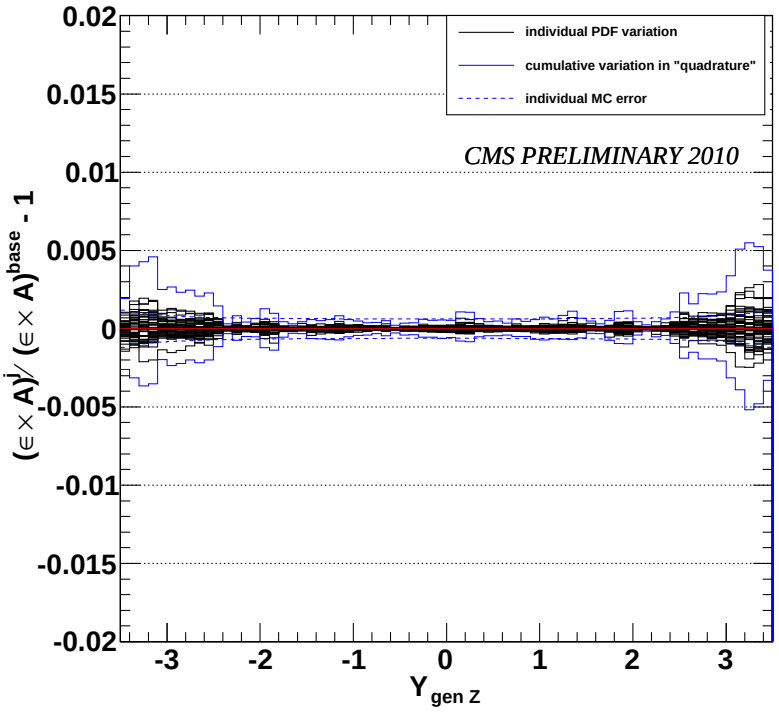

Figure 8.12: Fractional difference in $(\epsilon \times A)$ of CT10w PDFs from base PDF, as a function of Z boson rapidity, individual and combined. Statistical error of Monte Carlo are shown for reference.

Carlo smearing. The effect of PDFs on just ρ, was very small as shown in Figure 8.13. In the central rapidity region the fractional difference was less than 0.1% while only marginally larger than 0.1% at the highest $|Y|$ values.

8.4.3 Unfolding Systematics

The uncertainty associated with both the unfolding prescriptions of section 8.2.1 were estimated by performing alternative unfolding corrections, by varying each of the smearing parameters of Table 8.1. The parameters a (the stochastic term of the calorimeters resolution), α (from the crystal ball) and c (the constant term of the calorimeters resolution) were all varied $\pm\sigma$, where σ are the errors reported in Table 8.1; $\bar{x}$ (energy scale) were not considered here since they were already addressed as part of the energy-scale

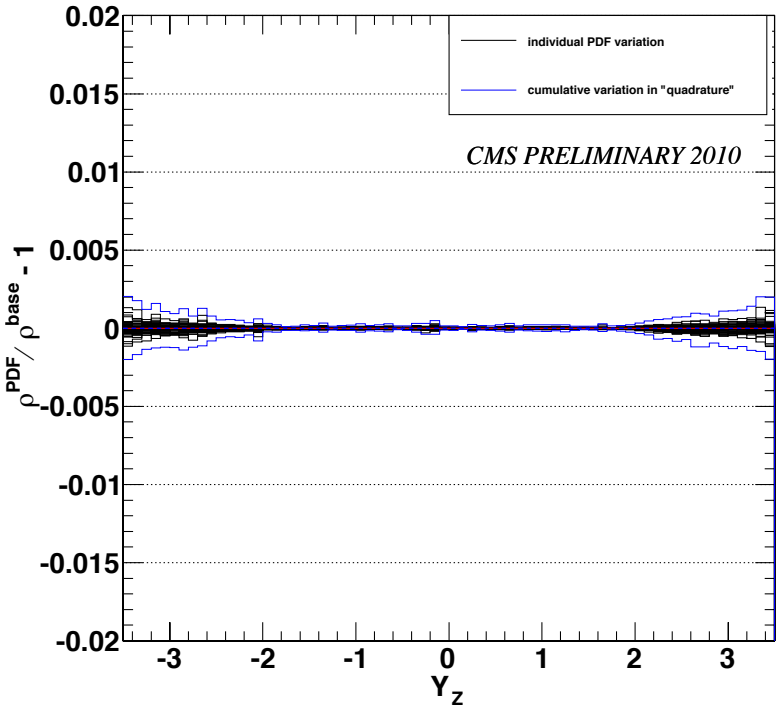

Figure 8.13: Fractional difference in average bin migration ρ of CT10w PDFs from base PDF, as a function of Z boson rapidity, individual and combined.

systematics in Section 8.4.1. For each variation, the relative change of $\frac{1}{\sigma}\frac{d\sigma(\mathrm{Z}/\gamma*\rightarrow \mathrm{e}^+\mathrm{e}^-)}{dy_k}$ with respect to the standard unfolding was calculated for each bin k, as displayed in Figure 8.14b as dashed histograms. The average response prescription is shown on the left and the unsmearing matrix on the right. Fractional differences from all variations were combined to build a cumulative fractional difference, adopting the same definition of systematic uncertainty as in Section 8.4.2: positive and negative relative variations were summed in quadrature to different cumulative distributions, as defined in Equation 8.8. In this case *base* referred to the standard unfolding derived from the central values of the smearing parameters. The cumulative differences are shown in blue in Figure 8.14b and are less than 0.1% in the central region and less than 0.3% for the full range covered by this measurement for both unfolding prescriptions.

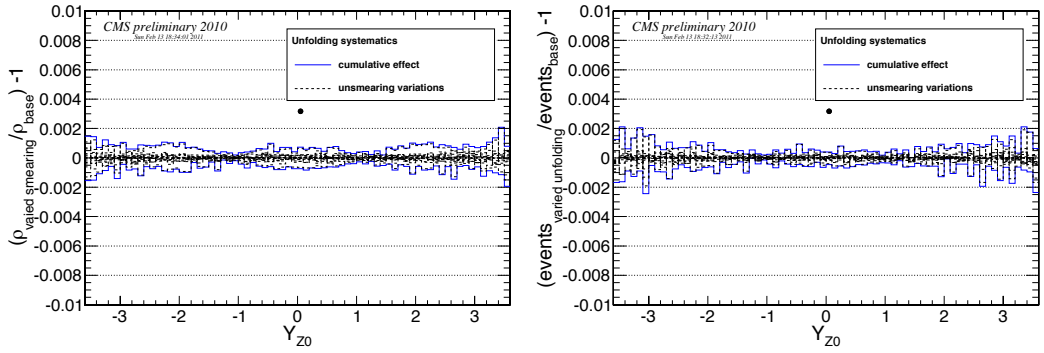

(a) average response

(b) unfolding matrix

Figure 8.14: Variation of $\frac{1}{\sigma}\frac{d\sigma(Z/\gamma* \to e^+e^-)}{dy_k}$ when performing unfolding varying the smearing parameters by their errors, relative to the base unfolding. On the left for the average response prescription, on the right for migration matrix. Dashed are the individual variations, blue is their quadratic combination.

8.4.4 Efficiency Systematics

Contributions to the final error came from both the statistical variations and the bin correlated systematic errors of the single electron efficiencies. For a shape measurement, the effect of the bin correlated systematics were small as they tended to change the overall efficiency instead of the shape. The results were determined by comparing ratios of $(\epsilon \times A)$ distributions.

As described in Section 7.4, each efficiency bin was assigned a bin correlated systematic error. To determine the affect on each bin each $(\epsilon \times A)_i$ was recalculated using the shifted efficiencies. The result was divided by the total new $(\epsilon \times A)$. From Figure 8.15 the affect on the result was shown to be minimal.

The inherent statistical errors in the efficiency determination could result in uncertainty on the final distribution. To estimate this effect, pseudoexperiments of different efficiencies were created based on Bayesian statistics. For each efficiency bin the electron efficiency was defined by a numerator n (number of electrons which passed the identification cut) and denominator d (number of electrons which were considered for the cut). These parameters formed a binomial distribution. Therefore this was a sample

of the the binomial probability function [58] Equation 8.9 for each pseudoexperiment.

$$P(\epsilon) = \frac{(d+1)!}{n!(d-n)!}\epsilon^n(1-\epsilon)^{d-n} \tag{8.9}$$

Then for each experiment, the $(\epsilon \times A)_i$ was recalculated for each bin and divided by the total $(\epsilon \times A)$. This was done for 100 pseudoexperiments for each efficiency. The RMS variation of the values was taken as the estimate of the uncertainty of the $(\epsilon \times A)_i$ as displayed in Figure 8.16.

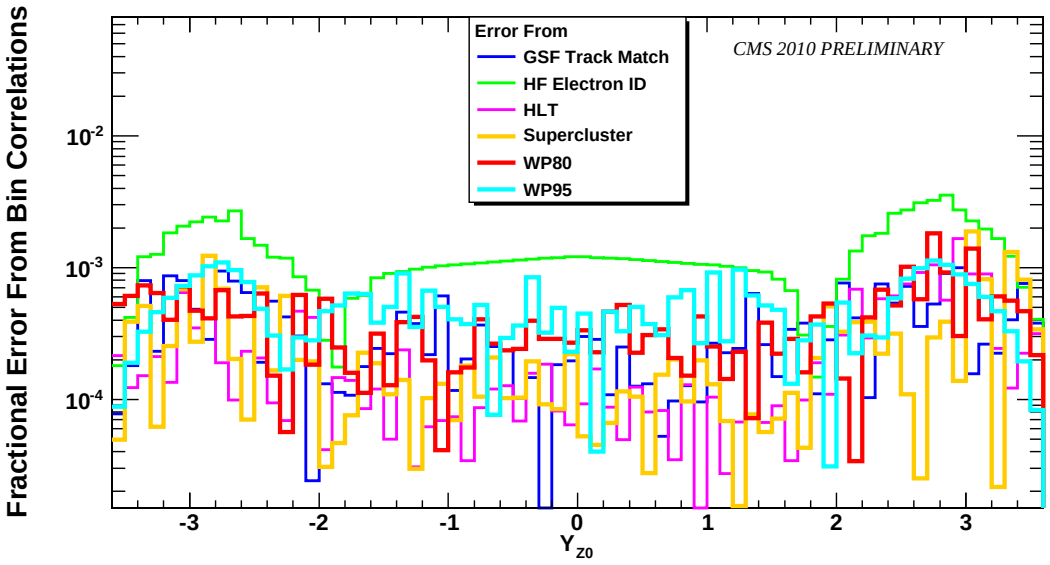

Figure 8.15: Systematic errors on the $(\epsilon \times A)$ which were generated from the bin correlated systematics for each electron efficiency.

8.5 Analysis Result

The final rapidity measurement for 36pb^{-1} is shown in Figure 8.17. The raw data, background-subtracted data, and final distribution after the $(\epsilon \times A)$ and bin migration corrections were included. The inner error bars are statistical and the statistical+systematic errors are the outer error bars. This was for the nominal unsmearing of Equation 5.2. The error distributions were as shown in Figure 8.18.

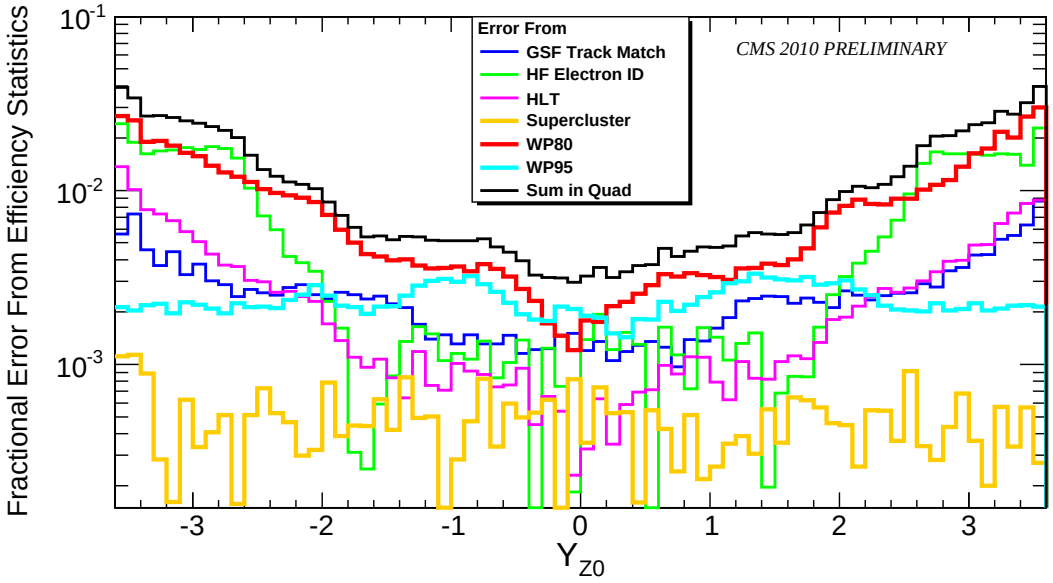

Figure 8.16: Systematic errors on the $(\epsilon \times A)$ which were generated from the statistical uncertainties of the individual electron efficiencies.

For completeness, the rapidity result without unsmearing was calculated and displayed in Figure 8.19. Also, the rapidity result with full matrix based unsmearing from Equation 5.3 was also calculated in Figure 8.20. In this final case, the statistical errors became large due to the statistical combinations of neighboring bins. Because of this large increase in statistical uncertainty, the average unsmearing was reported as the result.

The underlying physics behind the production of Z bosons at the LHC was not expected to depend on the sign of the rapidity the results were folded around $y = 0$. A benefit of this was a reduction of statistical error per bin by about $\sqrt{2}$. The final result including full shape normalization and total cross-section cancellation is shown in Figure 8.21 and tabulated in Table 8.4. Details of the bin by bin systematic errors of the folded distribution are shown in Table 8.5.

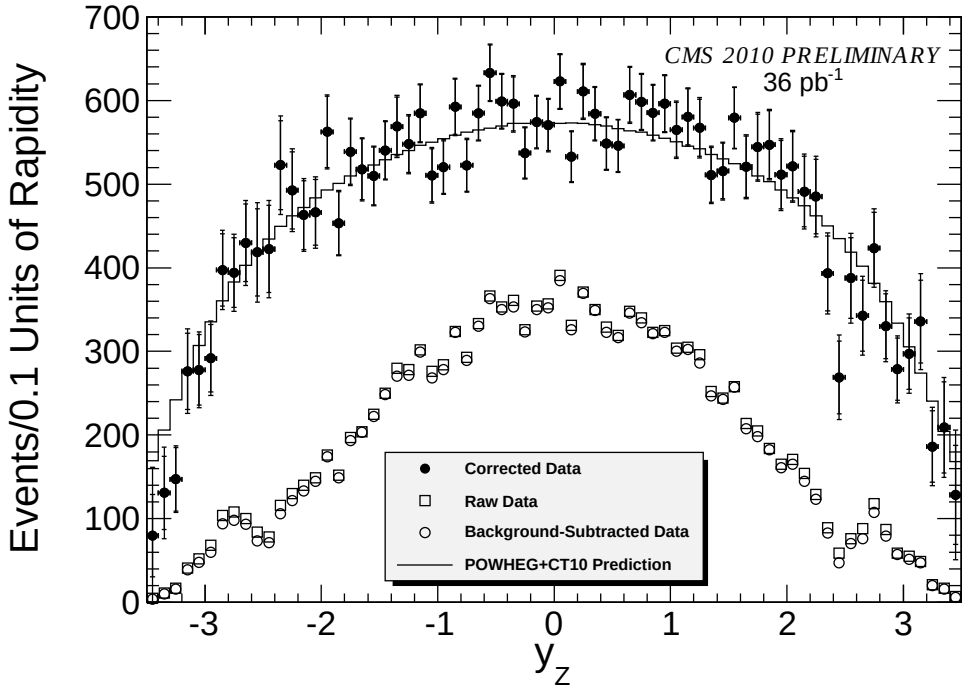

Figure 8.17: The final results for the rapidity measurement with average unsmearing correction. The raw data distribution is shown with empty squares and the distribution after background subtraction by empty circles. The data distribution corrected by $(\epsilon \times A)$ is shown with full circles. The errors on the full circles are shown for statistical uncertainties and statistical+systematic separately. The prediction of POWHEG and CT10w PDF is shown for comparison.

8.6 Final Sensitivity to PDFs

As the primary goal of the measurement was to constrain the PDFs, the sensitivity to PDFs was investigated. The sensitivity of the analysis was defined in Equation 8.7 as the ratio of the number of events observed in the bin over the total number of events. Using the same 26 CT10w positive and negative variations of Section 8.4.2, the bin by bin sensitivity to each eigenvector is shown in Figure 8.22. Here, the individual variations are shown in dashed lines. As a conservative way to measure a total effect, the individual contributions were summed in quadrature and shown as a solid blue line.

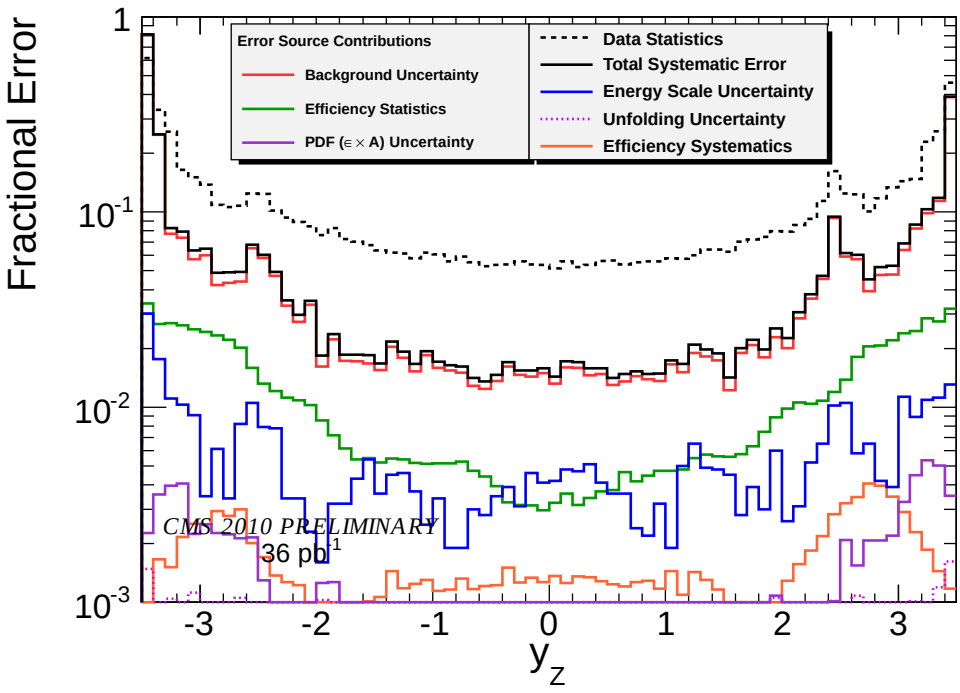

Figure 8.18: Comparison of the various contributions to the uncertainty in the final measurement as a function of the Z rapidity. The data statistical error is shown as a dashed line for comparison.

To estimate the maximum sensitivity of the measurement on the PDF variations, the maximum variation of each PDF in Figure 8.22 was calculated for both the positive and negative PDFs and displayed together in Figure 8.23.

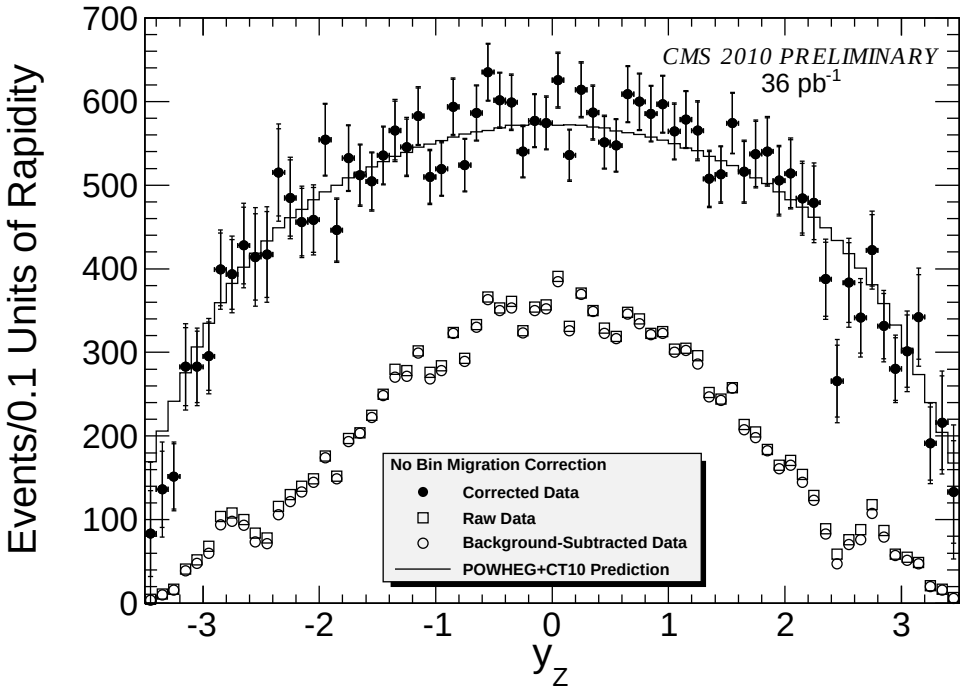

Figure 8.19: The final results for the rapidity measurement without bin-migration corrections applied. The raw data distribution is shown with empty squares and the distribution after background subtraction by empty circles. The data distribution corrected by ($\epsilon \times A$) is shown with full circles. The errors on the full circles are shown for statistical uncertainties and statistical+systematic separately. The prediction of POWHEG and CT10w PDF is shown for comparison.

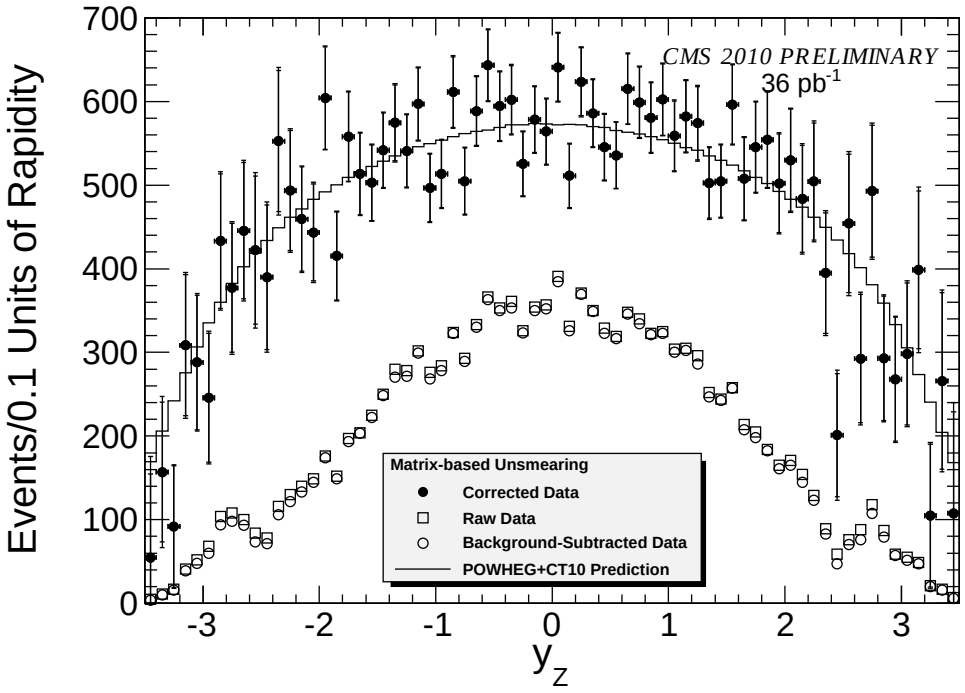

Figure 8.20: The final results for the rapidity measurement with matrix-based unsmearing applied. The raw data distribution is shown with empty squares and the distribution after background subtraction by empty circles. The data distribution corrected by ($\epsilon \times A$) is shown with full circles. The errors on the full circles are shown for statistical uncertainties and statistical+systematic separately. The prediction of POWHEG and CT10w PDF is shown for comparison.

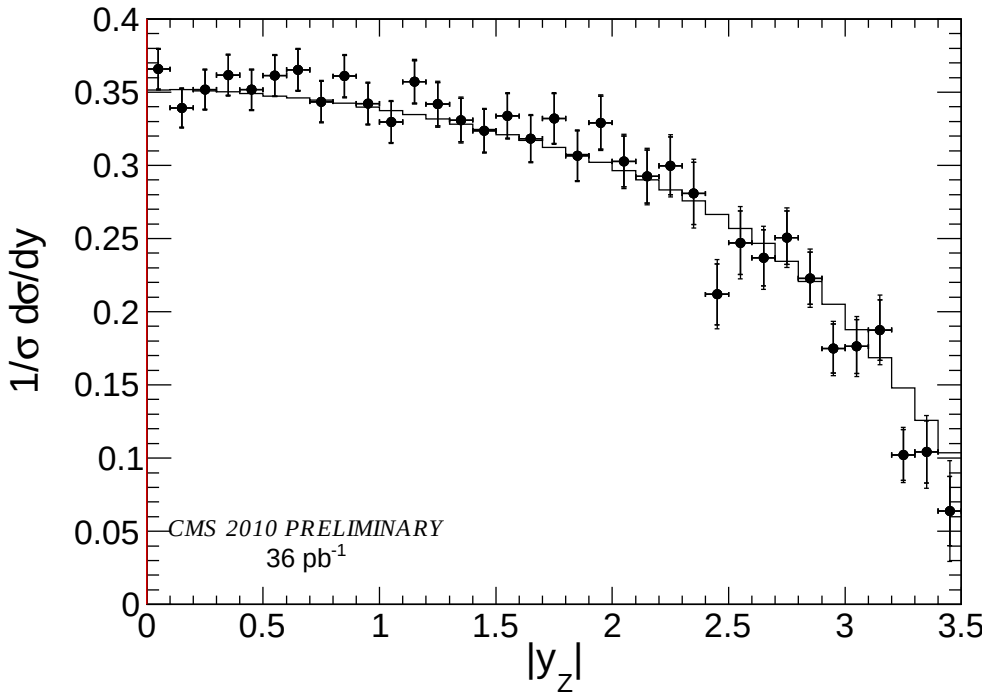

Figure 8.21: The corrected final result distribution for the rapidity measurement as a function of the absolute value of Z rapidity (since the result is not expected to depend on the sign of the rapidity). The errors are for shown statistical uncertainties and statistical+systematic separately.

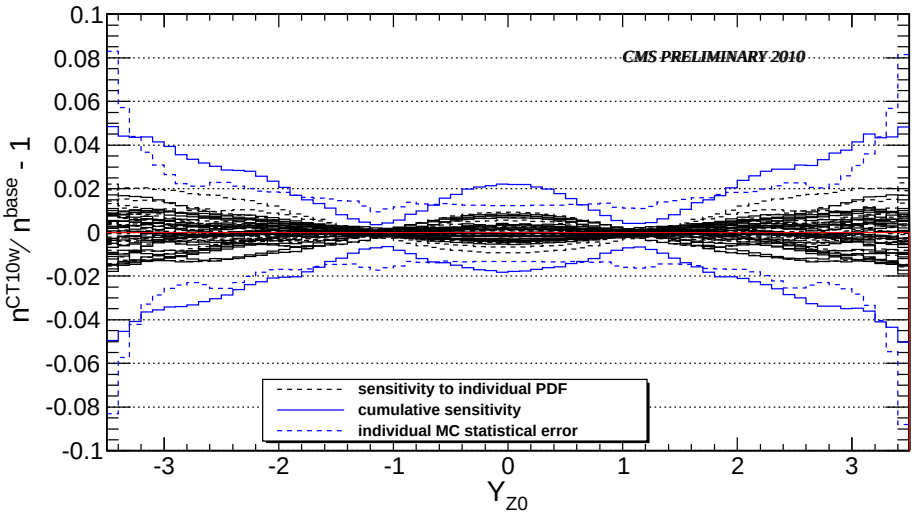

Figure 8.22: Relative sensitivity of each PDF vector is shown as dashed lines. The solid blue linear represents the sum in quadrature of the individual variations.

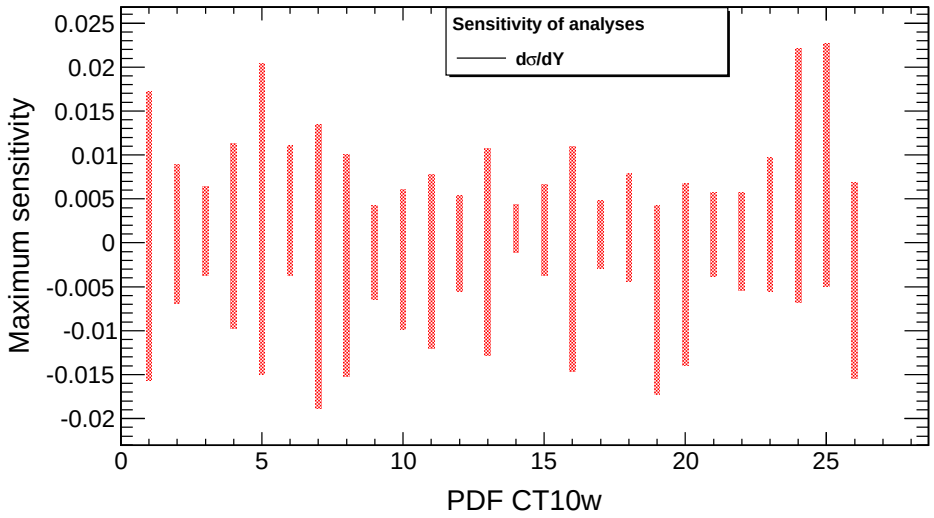

Figure 8.23: Maximum sensitivity of each PDF vector is shown as percentages. For each, the positive and negative veriation are shown separately.

$\|Y_{min}\|$	$\|Y_{max}\|$	Measurement	Statistical Error	Systematic Error
0.00	0.10	0.3657	0.0136	0.0041
0.10	0.20	0.3393	0.0131	0.0042
0.20	0.30	0.3518	0.0134	0.0043
0.30	0.40	0.3617	0.0137	0.0045
0.40	0.50	0.3517	0.0137	0.0040
0.50	0.60	0.3613	0.0139	0.0038
0.60	0.70	0.3652	0.0141	0.0040
0.70	0.80	0.3435	0.0139	0.0040
0.80	0.90	0.3610	0.0143	0.0042
0.90	1.00	0.3422	0.0141	0.0041
1.00	1.10	0.3296	0.0140	0.0045
1.10	1.20	0.3571	0.0146	0.0045
1.20	1.30	0.3418	0.0147	0.0052
1.30	1.40	0.3310	0.0148	0.0052
1.40	1.50	0.3237	0.0146	0.0044
1.50	1.60	0.3338	0.0153	0.0042
1.60	1.70	0.3183	0.0158	0.0046
1.70	1.80	0.3320	0.0170	0.0051
1.80	1.90	0.3066	0.0170	0.0050
1.90	2.00	0.3291	0.0182	0.0055
2.00	2.10	0.3027	0.0175	0.0065
2.10	2.20	0.2924	0.0180	0.0067
2.20	2.30	0.2997	0.0197	0.0081
2.30	2.40	0.2807	0.0212	0.0100
2.40	2.50	0.2119	0.0208	0.0113
2.50	2.60	0.2471	0.0217	0.0118
2.60	2.70	0.2368	0.0192	0.0097
2.70	2.80	0.2506	0.0183	0.0092
2.80	2.90	0.2229	0.0178	0.0087
2.90	3.00	0.1748	0.0168	0.0079
3.00	3.10	0.1763	0.0184	0.0090
3.10	3.20	0.1876	0.0207	0.0117
3.20	3.30	0.1021	0.0175	0.0073
3.30	3.40	0.1042	0.0214	0.0128
3.40	3.50	0.0638	0.0235	0.0252

Table 8.4: The final result of the rapidity distribution measurement as a function of the absolute value of Z rapidity.

$\lvert Y_{min}\rvert$	$\lvert Y_{max}\rvert$	Background Estimation	Efficiency Errors	Energy Scale	PDF ($\epsilon \times A$) Error	Unfolding Error
0.00	0.10	0.0099	0.0034	0.0041	0.0006	0.0007
0.10	0.20	0.0107	0.0036	0.0047	0.0007	0.0007
0.20	0.30	0.0109	0.0034	0.0039	0.0007	0.0007
0.30	0.40	0.0109	0.0036	0.0045	0.0006	0.0006
0.40	0.50	0.0100	0.0040	0.0038	0.0004	0.0007
0.50	0.60	0.0090	0.0043	0.0032	0.0004	0.0006
0.60	0.70	0.0094	0.0048	0.0033	0.0004	0.0006
0.70	0.80	0.0104	0.0049	0.0022	0.0004	0.0004
0.80	0.90	0.0104	0.0050	0.0021	0.0004	0.0005
0.90	1.00	0.0104	0.0051	0.0033	0.0006	0.0004
1.00	1.10	0.0123	0.0051	0.0022	0.0006	0.0003
1.10	1.20	0.0108	0.0051	0.0043	0.0007	0.0004
1.20	1.30	0.0131	0.0056	0.0056	0.0008	0.0003
1.30	1.40	0.0138	0.0058	0.0047	0.0007	0.0006
1.40	1.50	0.0116	0.0055	0.0042	0.0006	0.0004
1.50	1.60	0.0102	0.0056	0.0049	0.0005	0.0006
1.60	1.70	0.0128	0.0056	0.0036	0.0003	0.0007
1.70	1.80	0.0136	0.0063	0.0035	0.0005	0.0006
1.80	1.90	0.0141	0.0074	0.0031	0.0011	0.0007
1.90	2.00	0.0138	0.0087	0.0038	0.0012	0.0010
2.00	2.10	0.0189	0.0101	0.0025	0.0006	0.0008
2.10	2.20	0.0199	0.0108	0.0033	0.0004	0.0009
2.20	2.30	0.0245	0.0109	0.0043	0.0007	0.0010
2.30	2.40	0.0330	0.0116	0.0071	0.0004	0.0007
2.40	2.50	0.0509	0.0128	0.0090	0.0012	0.0009
2.50	2.60	0.0441	0.0151	0.0105	0.0021	0.0007
2.60	2.70	0.0353	0.0194	0.0070	0.0018	0.0011
2.70	2.80	0.0292	0.0216	0.0050	0.0022	0.0006
2.80	2.90	0.0316	0.0223	0.0051	0.0022	0.0007
2.90	3.00	0.0385	0.0234	0.0037	0.0024	0.0008
3.00	3.10	0.0431	0.0247	0.0102	0.0028	0.0009
3.10	3.20	0.0561	0.0255	0.0096	0.0043	0.0009
3.20	3.30	0.0646	0.0278	0.0110	0.0046	0.0010
3.30	3.40	0.1186	0.0272	0.0144	0.0043	0.0010
3.40	3.50	0.3935	0.0330	0.0217	0.0029	0.0015

Table 8.5: The fractional systematic error contributions per bin as a function of the absolute value of Z rapidity.

Chapter 9

Conclusion and Discussion

This thesis presented some of the motivations behind the construction of the LHC and CMS detectors. The physics of the Standard Model and proton-proton collisions were discussed in addition to the physics behind the production of Z bosons at the LHC. The focus of the thesis was on a measurement of a known process to validate and understand the detectors. A discussion of the different components of the CMS detector was presented. This focused on the detectors which were designed to measure electrons. A comprehensive description of the ECAL calibration was given.

A measurement strategy for constraining PDFs from the rapidity shape of the Z bosons decays into electrons was described. The measurement required deriving major components directly from data. Electron efficiencies, calorimeter resolutions, energy scales, and QCD backgrounds were all directly determined from data.

A full analysis of each measurement step was performed. Investigations into multiple possible systematic uncertainties were exhibited. A final impact as to the sensitivity of the measurement towards the PDFs was recounted.

The full $Z/\gamma* \rightarrow e^+e^-$ folded rapidity measurement for $36pb^{-1}$ was shown in Figure 8.21. From the error contributions of Table 8.4, the measurement error was statistically dominated. From Table 8.5 (or more visually prior to folding in Figure 8.18), the dominant systematic errors arose from background subtraction and efficiency statistics. Given that QCD dominated the background events and that the QCD estimate was fit bin-by-bin, those errors were determined by statistics. Therefore, the major systematic errors would be expected to decrease with increased data.

The relative sensitivity and maximum sensitivity were displayed in Figures 8.22 and 8.23. Given the different variations of sensitivity, the measurement does provide input for future PDF generation. This was a novel measurement as it was completed at $\sqrt{s} = 7$ TeV and included a far broader rapidity range than possible to explore at other detectors.

This thesis was an attempt by the auther to describe original work with regards to the CMS experiment at the LHC. The measurement is one of many that can be combined to test Standard Model predictions in data and to eventually probe for new phenomena beyond the Standard Model.

References

[1] Y. Fukuda et al. Evidence for oscillation of atmospheric neutrinos. *Phys. Rev. Lett.*, 81(8):1562–1567, Aug 1998.

[2] G. Karagiorgi, A. Aguilar-Arevalo, J. M. Conrad, M. H. Shaevitz, K. Whisnant, M. Sorel, and V. Barger. Leptonic *cp* violation studies at miniboone in the $(3+2)$ sterile neutrino oscillation hypothesis. *Phys. Rev. D*, 75(1):013011, Jan 2007.

[3] F. Zwicky. Die Rotverschiebung von extragalaktischen Nebeln. *Helvetica Physica Acta*, 6:110–127, 1933.

[4] Peter W. Higgs. Broken symmetries, massless particles and gauge fields. *Phys. Lett.*, 12:132–133, 1964.

[5] T. W. B. Kibble. Symmetry breaking in non-Abelian gauge theories. *Phys. Rev.*, 155:1554–1561, 1967.

[6] H. Geiger and E. Marsden. On a diffuse reflection of the α-particles. *Proc. R. Soc. Lond.*, 84:495–500, 1909.

[7] E. Rutherford. The scattering of α and β particles by matter and the structure of the atom. *Philos. Mag.*, 21:669–688, 1911.

[8] N. Bohr. On the constitution of atoms and molecules, part i. *Philos. Mag.*, 26:1–24, 1913.

[9] N. Bohr. On the constitution of atoms and molecules, part ii. *Philos. Mag.*, 26:476–502, 1913.

[10] E. Rutherford. Collision of a particles with light atoms iv. an anomalous effect in nitrogen. *Philos. Mag.*, 37:581,537,571,562, 1919.

[11] J. Chadwick. Possible existence if a neutron. *Nature*, 129:312, 1932.

[12] W. Pauli. Open letter to the group of radioactive people at the gauverein meeting in tbingen, 1930.

[13] G. Arnison et al. Observation of the Muonic Decay of the Charged Intermediate Vector Boson. *Phys. Lett.*, B134:469, 1984.

[14] P. Bagnaia et al. Evidence for $Z/\gamma* \to e^+e^-$ at the CERN anti-p p collider. *Phys. Lett.*, B129:130–140, 1983.

[15] G. Arnison et al. Experimental observation of isolated large transverse energy electrons with associated missing energy at s**(1/2) = 540-GeV. *Phys. Lett.*, B122:103–116, 1983.

[16] M. Banner et al. Observation of single isolated electrons of high transverse momentum in events with missing transverse energy at the CERN anti-p p collider. *Phys. Lett.*, B122:476–485, 1983.

[17] E. Schrödinger. An undulatory theory of the mechanics of atoms and molecules. *Phys. Rev.*, 28(6):1049–1070, Dec 1926.

[18] Silvan S. Schweber. *QED and the Men Who Made It.* Princeton University Press, April 1994.

[19] Sheldon L. Glashow and Arthur H. Rosenfeld. Eightfold-way assignments for $y_1^*(1660)$ and other baryons. *Phys. Rev. Lett.*, 10(5):192–196, Mar 1963.

[20] Steven Weinberg. A Model of Leptons. *Phys. Rev. Lett.*, 19:1264–1266, 1967.

[21] Abdus Salam. Weak and Electromagnetic Interactions. Originally printed in *Svartholm: Elementary Particle Theory, Proceedings Of The Nobel Symposium Held 1968 At Lerum, Sweden*, Stockholm 1968, 367-377.

[22] G. 't Hooft and M. Veltman. Regularization and renormalization of gauge fields. *Nuclear Physics B*, 44:189–213, July 1972.

[23] Murray Gell-Mann. Symmetries of baryons and mesons. *Phys. Rev.*, 125(3):1067–1084, Feb 1962.

[24] V. N. Gribov and L. N. Lipatov. Deep inelastic e p scattering in perturbation theory. *Sov. J. Nucl. Phys.*, 15:438–450, 1972.

[25] L. N. Lipatov. The parton model and perturbation theory. *Sov. J. Nucl. Phys.*, 20:94–102, 1975.

[26] Guido Altarelli and G. Parisi. Asymptotic Freedom in Parton Language. *Nucl. Phys.*, B126:298, 1977.

[27] Yuri L. Dokshitzer. Calculation of the Structure Functions for Deep Inelastic Scattering and e+ e- Annihilation by Perturbation Theory in Quantum Chromodynamics. *Sov. Phys. JETP*, 46:641–653, 1977.

[28] A. D. Martin, W. J. Stirling, R. S. Thorne, and G. Watt. Parton distributions for the LHC. Jul 2009, 0901.0002.

[29] G. 't Hooft. Dimensional regularization and the renormalization group. *Nuclear Physics B*, 61:455 – 468, 1973.

[30] Steven Weinberg. New approach to the renormalization group. *Phys. Rev.*, D8:3497–3509, 1973.

[31] Torbjorn Sjostrand, Stephen Mrenna, and Peter Skands. PYTHIA 6.4 Physics and Manual. May 2006, hep-ph/0603175.

[32] P. Nason. Recent developments in POWHEG. Jan 2010, 1001.2747.

[33] Simone Alioli, Paolo Nason, Carlo Oleari, and Emanuele Re. NLO vector-boson production matched with shower in POWHEG. *JHEP*, 07:060, 2008, 0805.4802.

[34] Stefano Frixione, Paolo Nason, and Carlo Oleari. Matching NLO QCD computations with Parton Shower simulations: the POWHEG method. *JHEP*, 11:070, 2007, 0709.2092.

[35] Simone Alioli, Paolo Nason, Carlo Oleari, and Emanuele Re. A general framework for implementing NLO calculations in shower Monte Carlo programs: the POWHEG BOX. *JHEP*, 06:043, 2010, 1002.2581.

[36] Paolo Nason. A new method for combining NLO QCD with shower Monte Carlo algorithms. *JHEP*, 11:040, 2004, hep-ph/0409146.

[37] P. Allison et al. Geant4 developments and applications. *IEEE Transactions on Nuclear Science*, 53(1):270–278, February 2006.

[38] S. et al Agostinelli. GEANT4 – a simulation toolkit. *Nuclear Instruments and Methods in Physics Research Section A: Accelerators, Spectrometers, Detectors and Associated Equipment*, 506(3):250–303, July 2003.

[39] R. Adolphi et al. The CMS experiment at the CERN LHC. *JINST*, 3:S08004, 2008.

[40] C. M. S. Collaboration. Cms, the compact muon solenoid: Technical proposal. *CERN/LHCC*, 94-38, 1994.

[41] (ed.) Evans, Lyndon and (ed.) Bryant, Philip. LHC Machine. *JINST*, 3:S08001, 2008.

[42] Giacomo Sguazzoni. Cms inner tracker detector modules. Technical Report CMS-CR-2004-059. CERN-CMS-CR-2004-059, CERN, Geneva, Nov 2004.

[43] S. The Particle Data Group Eidelman and all. Review of Particle Physics. *Physics Letters B*, 592:1+, 2004.

[44] The. Mr Person. Other types of crystals/experiments. *Nature*, 1111:1111, 1111.

[45] CMS: The electromagnetic calorimeter. Technical design report. CERN-LHCC-97-33.

[46] P. Wertelaers et al. ECAL Preshower Engineer Design Review. *CMS ECAL EDR-4*, 2:054, 2000.

[47] *The CMS hadron calorimeter project: Technical Design Report.* Technical Design Report CMS. CERN, Geneva, 1997.

[48] G Baiatian et al. Design, performance, and calibration of cms hadron-barrel calorimeter wedges. Technical Report CMS-NOTE-2006-138. CERN-CMS-NOTE-2006-138, CERN, Geneva, May 2007.

[49] The CMS-HCAL Collaboration. Design, performance, and calibration of cms forward calorimeter wedges. *Eur. Phys. J. C*, 53(1):139–166, 2008.

[50] *The CMS muon project: Technical Design Report.* Technical Design Report CMS. CERN, Geneva, 1997.

[51] F Cavallari, G Franzoni, A Ghezzi, P Govoni, A Meregaglia, and M Obertino. Relative light yield comparison between laboratory and testbeam data for cms ecal pbwo4 crystals. Technical Report CMS-RN-2004-002, CERN, Geneva, Feb 2004.

[52] The CMS Electromagnetic Calorimeter Group. Intercalibration of the barrel electromagnetic calorimeter of the cms experiment at start-up. *Journal of Instrumentation*, 3(10):P10007, 2008.

[53] T. Prisson and P. Mine. H4sim, a geant4 simulation program for the cms ecal supermodule. *Presented at the GEANT4 10^{th} international Conference, Bordeaux, November*, 2005.

[54] Timo Antero Aaltonen et al. Measurement of $d\sigma/dy$ of Drell-Yan e^+e^- pairs in the Z Mass Region from $p\bar{p}$ Collisions at $\sqrt{s} = 1.96$ TeV. *Phys.Lett.*, B692:232–239, 2010, 0908.3914.

[55] R. Brun. ROOT An object oriented data analysis framework. *Nuclear Instruments and Methods in Physics Research Section A: Accelerators, Spectrometers, Detectors and Associated Equipment*, 389(1-2):81–86, April 1997.

[56] M. R. Whalley D. Bourilkov, R. C. Group. Lhapdf: Pdf use from the tevatron to the lhc. arXiv:hep-ph/0605240v2, 2006.

[57] et al. S. Alekhin. The qcd/sm working group: Summary report. arXiv:hep-ph/0204316v1, 2002.

[58] Giulio D'Agostini. *Bayesian reasoning in data analysis : A critical introduction.* World Scientific Publishing, 2003.

Appendix A

Matrix Inversion Method

Given a cluster of energetic crystals in a calorimeter, the energy of the cluster is the sum of the raw energy of each crystal multiplied by a calibration constant.

$$E_{Total} = \sum_{crystals} c_i E_i \tag{A.1}$$

A goodness of agreement is defined as the χ^2 difference of the measured and expected value over all events.

$$\chi^2 = \sum_{Events} \frac{(E_{expected} - E_{measured})^2}{\sigma_E^2} \tag{A.2}$$

When we use the cluster basis we can define the goodness as

$$\chi^2 = \sum_{Events} \frac{(E_{expected} - \sum c_i E_i)^2}{\sigma_E^2} \tag{A.3}$$

The χ^2 can be minimized with respect to each constant $\forall_j$

$$\frac{\partial \chi^2}{\partial c_j} = 0 \tag{A.4}$$

$$\sum_{Events} \frac{(E_{expected} - \sum c_i E_i)}{\sigma_E^2} E_j = 0 \tag{A.5}$$

Then the equation can be balanced on both sides ($\forall_j$ is assumed).

$$\sum_{Events} \frac{E_j E_{expected}}{\sigma_E^2} = \sum_{Events} \frac{E_j \sum c_i E_i}{\sigma_E^2} \tag{A.6}$$

The matrix elements can be defined as

$$R_j = \sum_i c_i A_{ij} \tag{A.7}$$

Where R_j and A_{ij} are defined as

$$R_j = \sum_{Events} \frac{E_j E_{expected}}{\sigma_E^2}, \qquad A_{ij} = \sum_{Events} \frac{E_j E_i}{\sigma_E^2} \tag{A.8}$$

As this is $\forall_j$ we can represent these elements as a matrix equation over j.

$$\mathbf{R} = \mathbf{c} \times \mathbf{A}. \tag{A.9}$$

To obtain the value of the constants the inversion of $\mathbf{A}$ is required.

$$\mathbf{c} = \mathbf{R} \times \mathbf{A^{-1}}. \tag{A.10}$$

One advantage of this approach is the simple two step approach of summing over all the events to get the R_j and A_{ij} elements and then inverting the matrix.

A.1 Matrix Inversion Details

An interative inversion method was utilized using the assumption that the initial constants are relatively close to the final values. Therefore, the calibration can be done for one crystal at a time with the temporary assumption all others are correct.

$$c_j = \left(R_j - \sum_{i \neq j} c_i A_{ij} \right) / A_{jj} \tag{A.11}$$

A goodness of convergence is defined as

$$\Delta R^2 = \sum_j \left(R_j - \sum_i c_i A_{ij} \right)^2 \tag{A.12}$$

The matrix inversion is completed for all calibration constants and then ΔR^2 is computed. The matrix inversion is iterated until the condition $\Delta R^2 < 10^{-12}$ is reached.

Appendix B

HLT Electron Identification

This includes a description of the HLT triggers used in this measurement. As described in Section 6.3 all the HLT triggers used in the measurement had electron identification requirements that were looser than those required offline. Table B.1 summarizes the HLT trigger names, integrated luminosity covered and the type. Using the type from above, the different electron identification variable cuts are tabulated in Table B.2. Here the the default is for EB and EE while the parenthetical values corresponds solely to the EE.

HLT Path	Luminosity	Electron Identification
HLT_SINGLE_ELE15_L1R	3 pb^{-1}	Type A
HLT_SINGLE_TightEID_ELE15_L1R	3 pb^{-1}	Type B
HLT_SINGLE_TightEID_ELE17_L1R	8 pb^{-1}	Type C
HLT_SINGLE_VeryTightEID_ELE17_L1R	22 pb^{-1}	Type D

Table B.1: This table summarizes the HLT electron identification cuts used in this measurement. All the types are looser than the WP80 electron identification cuts.

Type	Ho/E	$\sigma_{i\eta i\eta}$	$\Delta\phi$	$\Delta\eta$
A	0.15	0.014(0.035)	0.08	0.01
B	0.15	0.012(0.032)	0.08	0.01
C	0.15	0.012(0.032)	0.08	0.01
D	0.05	0.011(0.031)	0.10	0.008(0.007)
WP80	0.04(0.025)	0.01	0.6(0,3)	0.004(0.007)

Type	trackIsolation	ecalIsolation	hcalIsolation
A	N/A	N/A	N/A
B	0.125(0.057)	-(0.05)	0.15(0.1)
C	0.125(0.057)	-(0.05)	0.15(0.1)
D	0.125(0.057)	-(0.05)	0.15(0.1)
WP80	0.1(0.025)	0.09(0.04)	0.07(0.05)

Table B.2: This table summarizes the HLT requirements on the electron identification variables. The variables were described in Chapter 6. The WP80 values are shown as a reference and were always tighter or tight as the HLT requirements.

Appendix C

Final Signal and Background Fits

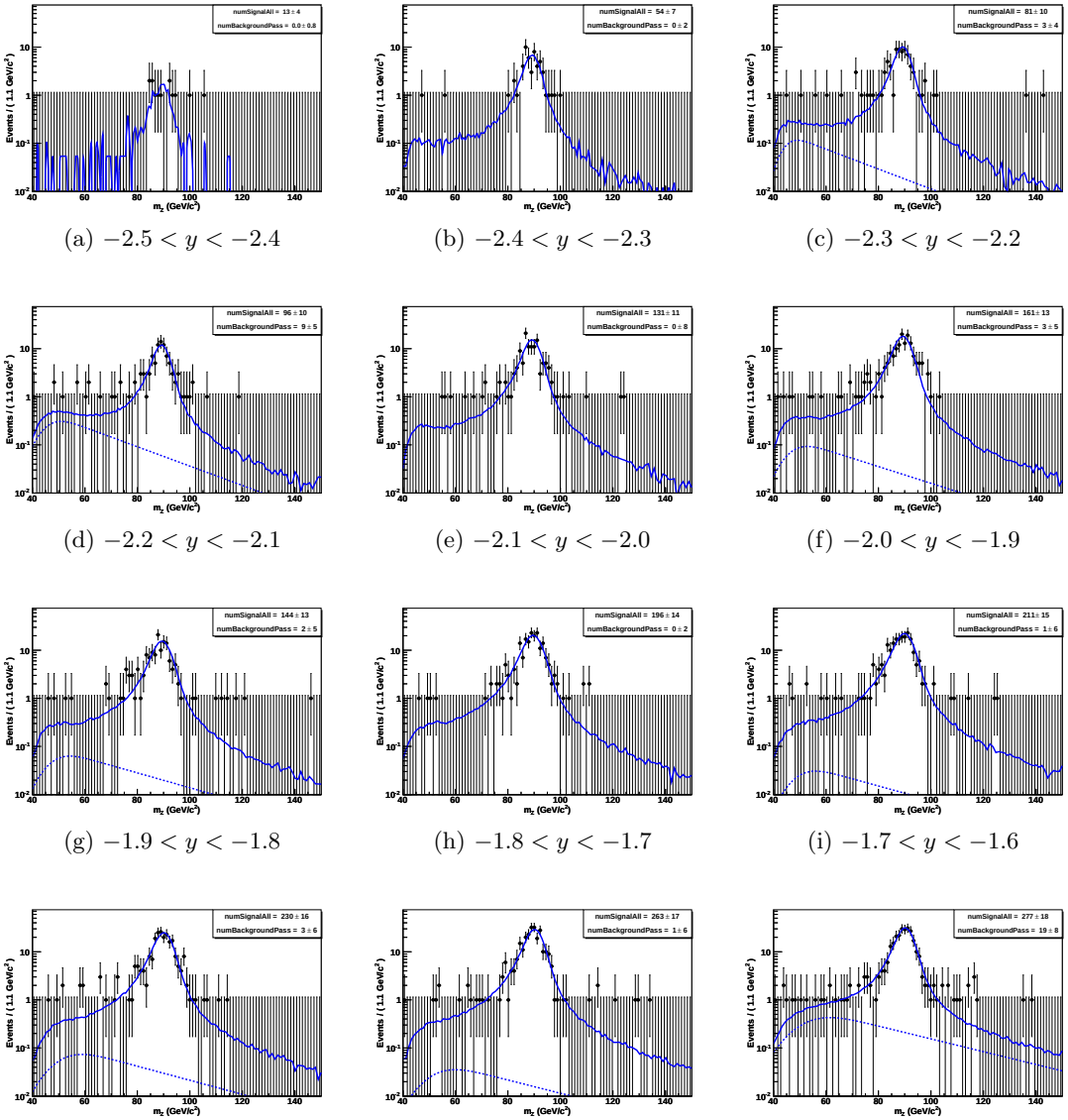

(a) $-2.5 < y < -2.4$ (b) $-2.4 < y < -2.3$ (c) $-2.3 < y < -2.2$

(d) $-2.2 < y < -2.1$ (e) $-2.1 < y < -2.0$ (f) $-2.0 < y < -1.9$

(g) $-1.9 < y < -1.8$ (h) $-1.8 < y < -1.7$ (i) $-1.7 < y < -1.6$

(j) $-1.6 < y < -1.5$ (k) $-1.5 < y < -1.4$ (l) $-1.4 < y < -1.3$

Figure C.1: The ECAL-ECAL final bin-by-bin fits. Data are shown as black points with errors. Signal PDF is shown as a solid blue line, and the background PDF as a dashed blue line.

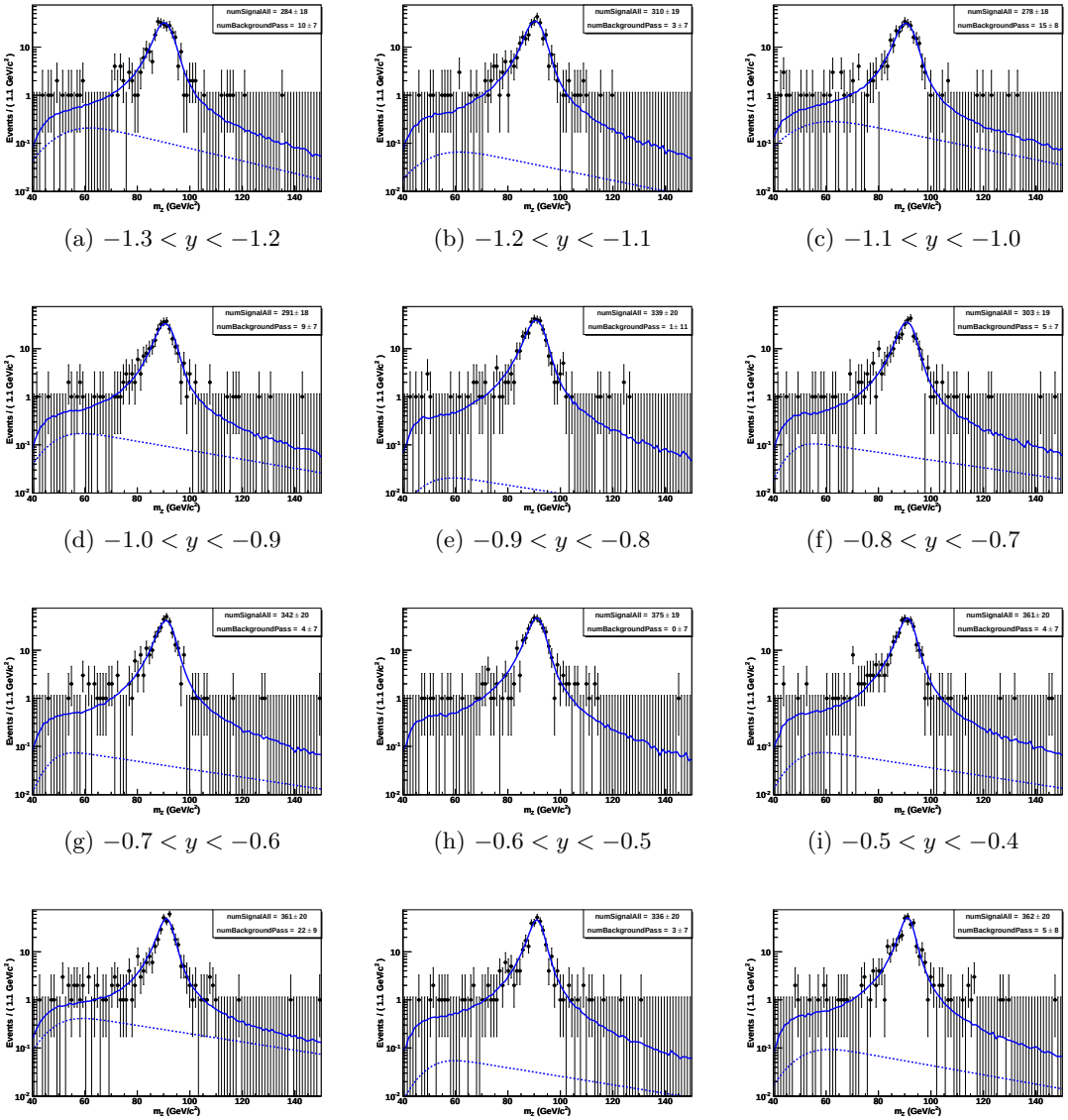

(a) $-1.3 < y < -1.2$ (b) $-1.2 < y < -1.1$ (c) $-1.1 < y < -1.0$

(d) $-1.0 < y < -0.9$ (e) $-0.9 < y < -0.8$ (f) $-0.8 < y < -0.7$

(g) $-0.7 < y < -0.6$ (h) $-0.6 < y < -0.5$ (i) $-0.5 < y < -0.4$

(j) $-0.4 < y < -0.3$ (k) $-0.3 < y < -0.2$ (l) $-0.2 < y < -0.1$

Figure C.2: The ECAL-ECAL final bin-by-bin fits. Data are shown as black points with errors. Signal PDF is shown as a solid blue line, and the background PDF as a dashed blue line.

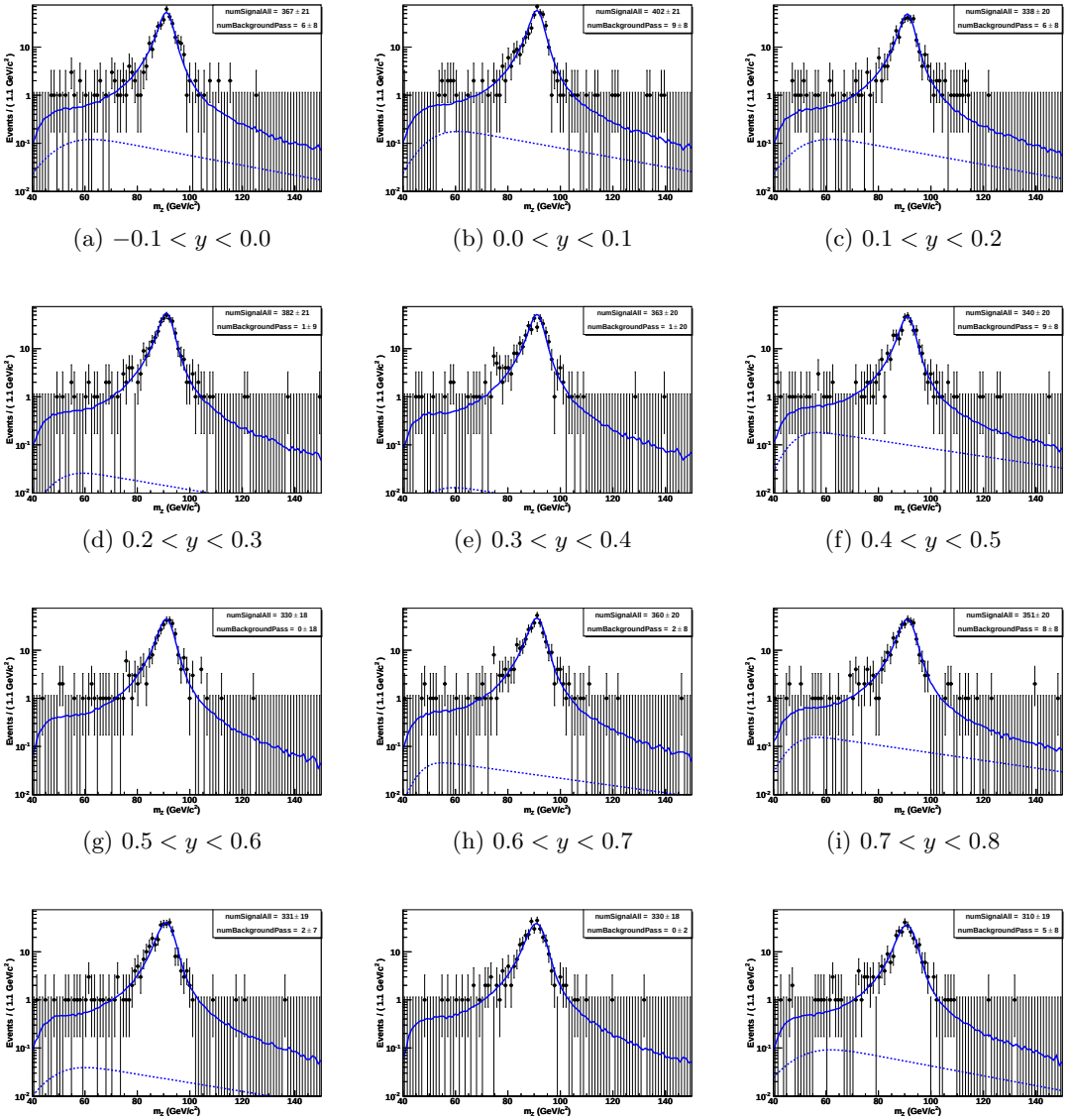

(a) $-0.1 < y < 0.0$ (b) $0.0 < y < 0.1$ (c) $0.1 < y < 0.2$

(d) $0.2 < y < 0.3$ (e) $0.3 < y < 0.4$ (f) $0.4 < y < 0.5$

(g) $0.5 < y < 0.6$ (h) $0.6 < y < 0.7$ (i) $0.7 < y < 0.8$

(j) $0.8 < y < 0.9$ (k) $0.9 < y < 1.0$ (l) $1.0 < y < 1.1$

Figure C.3: The ECAL-ECAL final bin-by-bin fits. Data are shown as black points with errors. Signal PDF is shown as a solid blue line, and the background PDF as a dashed blue line.

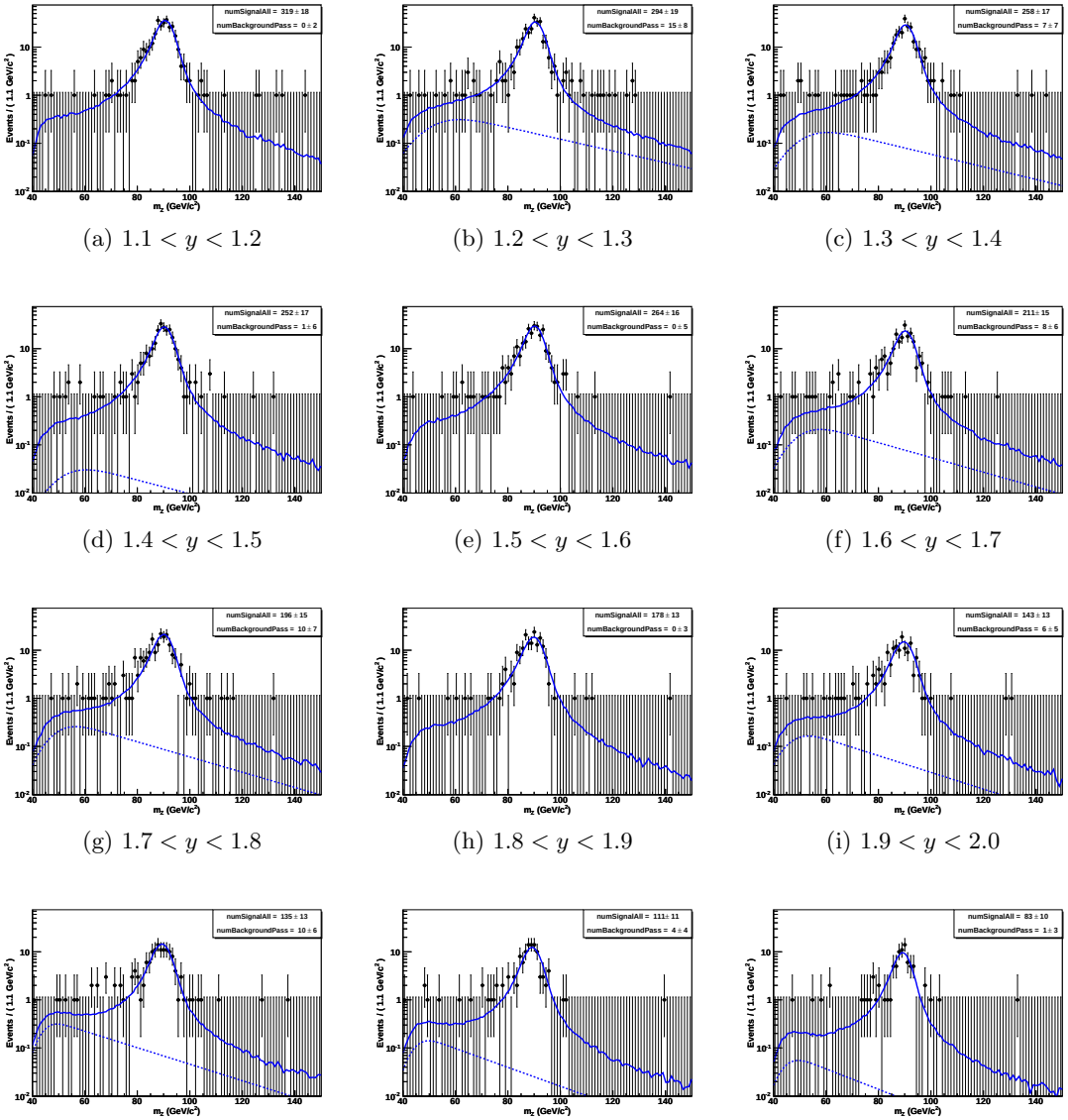

(a) $1.1 < y < 1.2$ (b) $1.2 < y < 1.3$ (c) $1.3 < y < 1.4$

(d) $1.4 < y < 1.5$ (e) $1.5 < y < 1.6$ (f) $1.6 < y < 1.7$

(g) $1.7 < y < 1.8$ (h) $1.8 < y < 1.9$ (i) $1.9 < y < 2.0$

(j) $1.0 < y < 2.1$ (k) $2.1 < y < 2.2$ (l) $2.2 < y < 2.3$

Figure C.4: The ECAL-ECAL final bin-by-bin fits. Data are shown as black points with errors. Signal PDF is shown as a solid blue line, and the background PDF as a dashed blue line.

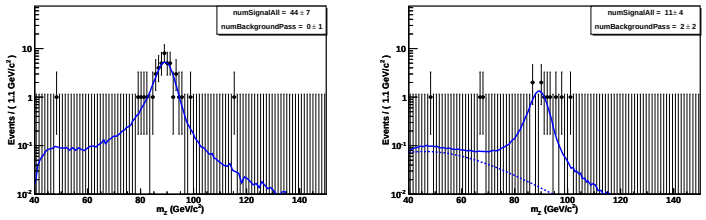

(a) $2.3 < y < 2.4$ (b) $2.4 < y < 2.5$

Figure C.5: The ECAL-ECAL final bin-by-bin fits. Data is shown as black points with errors. Signal PDF is shown as a solid blue line, and the background PDF as a dashed blue line.

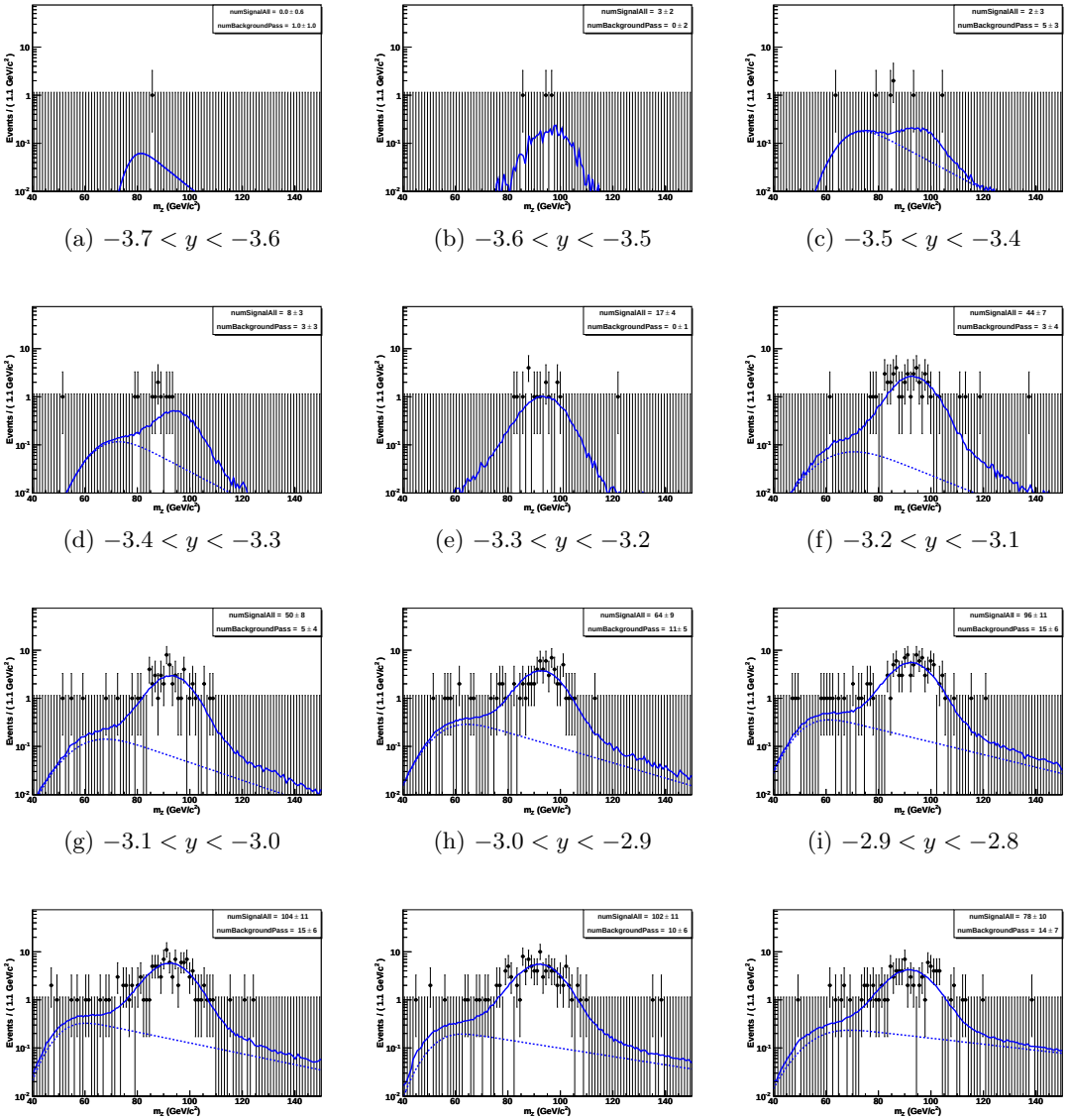

(a) $-3.7 < y < -3.6$ (b) $-3.6 < y < -3.5$ (c) $-3.5 < y < -3.4$

(d) $-3.4 < y < -3.3$ (e) $-3.3 < y < -3.2$ (f) $-3.2 < y < -3.1$

(g) $-3.1 < y < -3.0$ (h) $-3.0 < y < -2.9$ (i) $-2.9 < y < -2.8$

(j) $-2.8 < y < -2.7$ (k) $-2.7 < y < -2.6$ (l) $-2.6 < y < -2.5$

Figure C.6: The ECAL-HF final bin-by-bin fits. Data are shown as black points with errors. Signal PDF is shown as a solid blue line, and the background PDF as a dashed blue line.

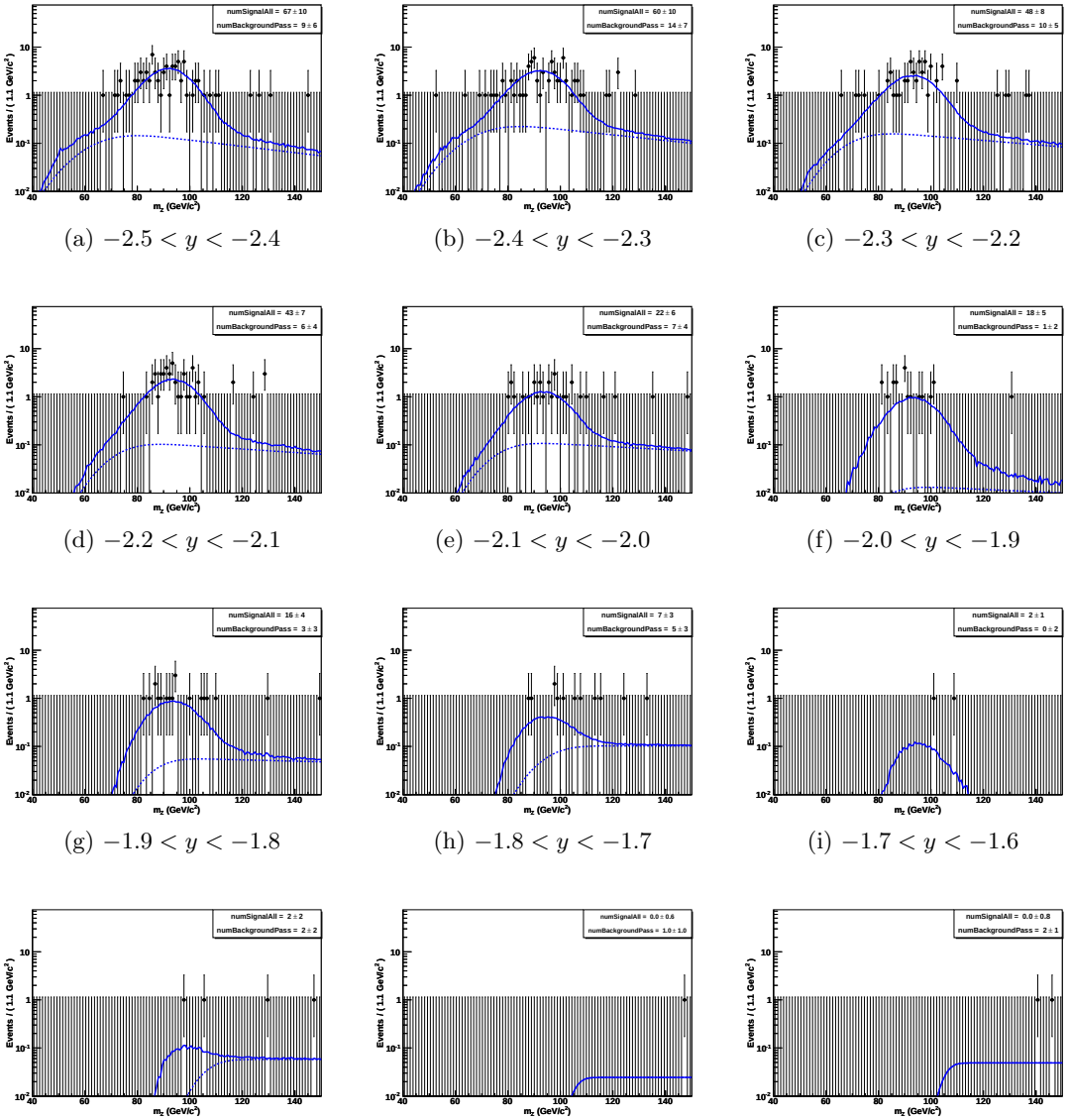

(a) $-2.5 < y < -2.4$ (b) $-2.4 < y < -2.3$ (c) $-2.3 < y < -2.2$

(d) $-2.2 < y < -2.1$ (e) $-2.1 < y < -2.0$ (f) $-2.0 < y < -1.9$

(g) $-1.9 < y < -1.8$ (h) $-1.8 < y < -1.7$ (i) $-1.7 < y < -1.6$

(j) $-1.6 < y < -1.5$ (k) $-1.5 < y < -1.4$ (l) $-1.4 < y < -1.3$

Figure C.7: The ECAL-HF final bin-by-bin fits. Data are shown as black points with errors. Signal PDF is shown as a solid blue line, and the background PDF as a dashed blue line.

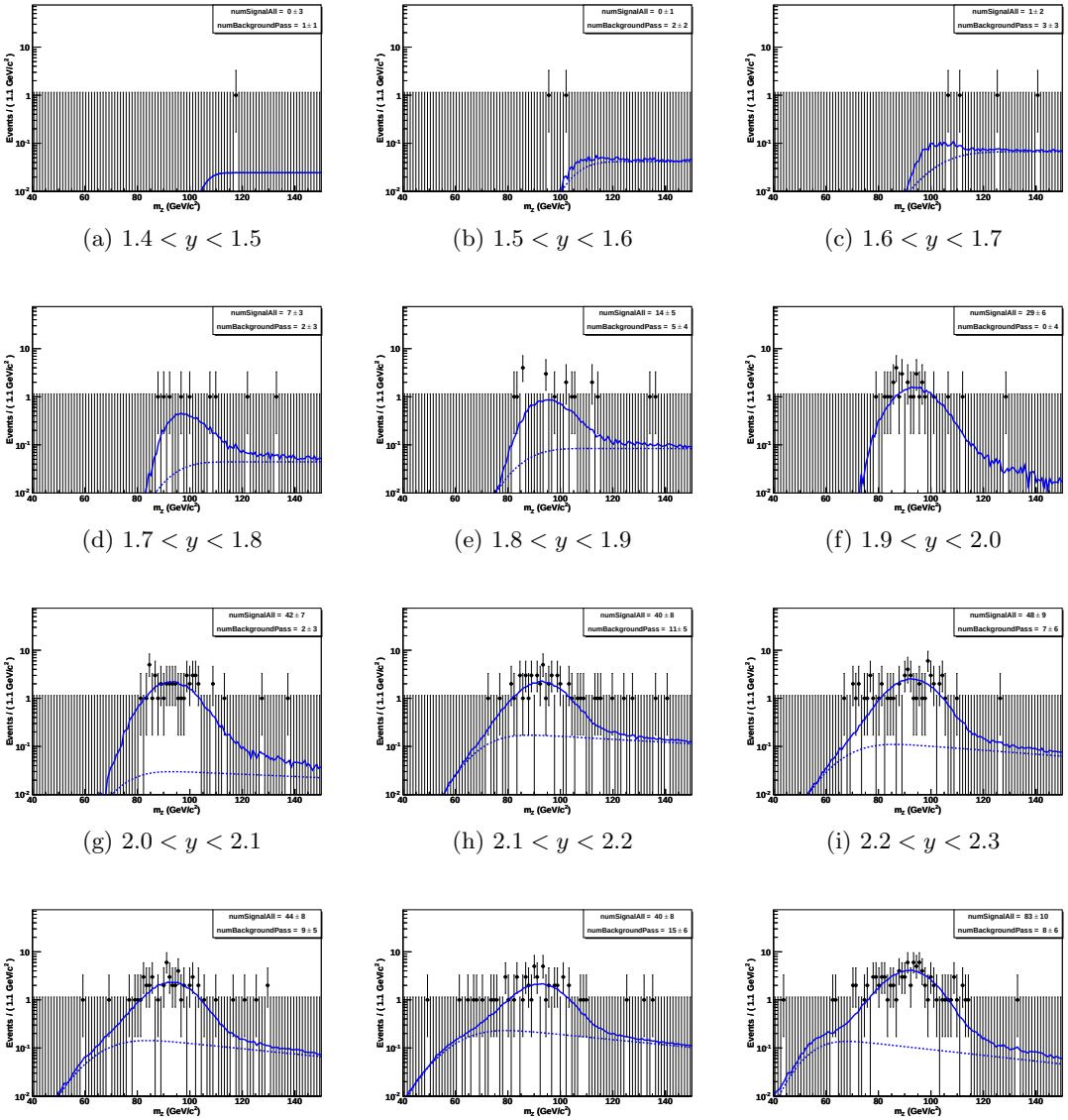

(a) $1.4 < y < 1.5$ (b) $1.5 < y < 1.6$ (c) $1.6 < y < 1.7$

(d) $1.7 < y < 1.8$ (e) $1.8 < y < 1.9$ (f) $1.9 < y < 2.0$

(g) $2.0 < y < 2.1$ (h) $2.1 < y < 2.2$ (i) $2.2 < y < 2.3$

(j) $2.3 < y < 2.4$ (k) $2.4 < y < 2.5$ (l) $2.5 < y < 2.6$

Figure C.8: The ECAL-HF final bin-by-bin fits. Data are shown as black points with errors. Signal PDF is shown as a solid blue line, and the background PDF as a dashed blue line.

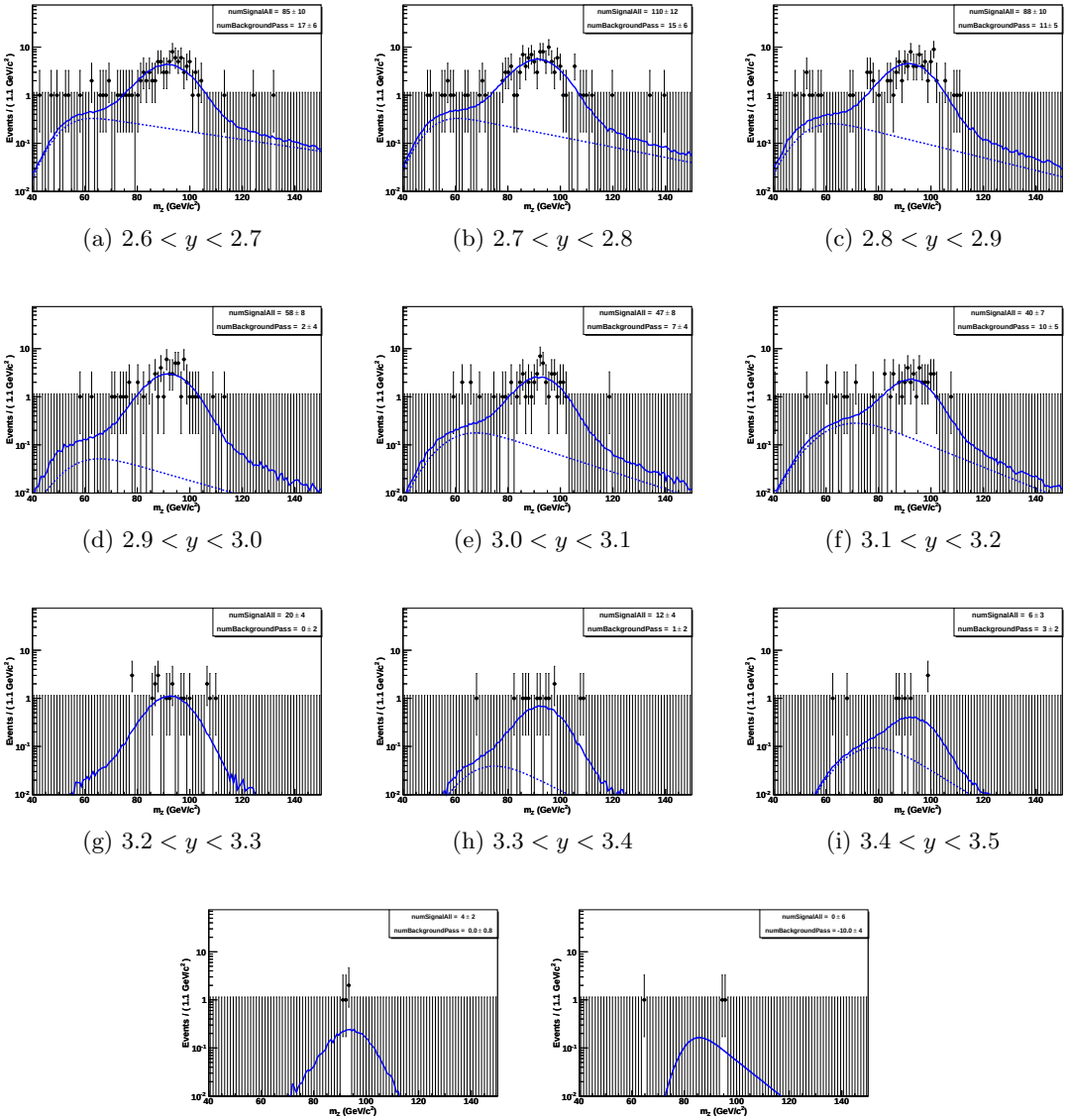

(a) $2.6 < y < 2.7$ (b) $2.7 < y < 2.8$ (c) $2.8 < y < 2.9$

(d) $2.9 < y < 3.0$ (e) $3.0 < y < 3.1$ (f) $3.1 < y < 3.2$

(g) $3.2 < y < 3.3$ (h) $3.3 < y < 3.4$ (i) $3.4 < y < 3.5$

(j) $3.5 < y < 3.6$ (k) $3.6 < y < 3.7$

Figure C.9: The ECAL-HF final bin-by-bin fits. Data are shown as black points with errors. Signal PDF is shown as a solid blue line, and the background PDF as a dashed blue line.

Appendix D

Glossary and Acronyms

Care has been taken in this thesis to minimize the use of jargon and acronyms, but this cannot always be achieved. This appendix defines jargon terms in a glossary, and contains a table of acronyms and their meaning.

D.1 Glossary

- **Bunch Crossing** (**BX**) – The assignment number of a bunch of protons. Each bunch is seperated by 25ns and therefore this can also represent a time assignment or measurement. Typically related to a collision in a given BX.
- **Cosmic-Ray Muon** (**CR** μ) – A muon coming from the abundant energetic particles originating outside of the Earth's atmosphere.
- **Deep Inelastic Scattering** (**DIS**) – Name given to the process of scattering where the internal scructure of a hadron is being probed.
- **Hadron** – QCD color neutral combinations of 3 valance quarks.
- **Missing Energy** ($\not{E}_T$) – Energy and momentum not detected in the detector but is expected due to conservation of energy and momentum.
- **Modified Minimal Subtraction Scheme** ($\overline{MS}$) – Renormalization shcema which absorbes divergences in higher order purtabative corrections.

- **Nuclear Interaction Length** – The average distance a charge particle travels to keep $1/e$ of its energy.
- **Partons** – The quark and gluon constituents of a hadron (from both valance and sea).
- **Radiation Length** (X_o) – The average distance an electron travels to keep $1/e$ of its energy and 7/9th of the mean distance for a photon to pair produce .
- **Sea Quark** – Short-lived quark-antiquark pairs from gluon splitting within a hadron. They usually quickly annihilate back into a gluon.
- **Valance Quark** – A quark from a hadron or meson that contributes to the quantum numbers.

D.2 Acronyms

Table D.1: Acronyms

Acronym	Meaning
ADC	Analog-to-digital converter (counts)
APD	Avalanche Photodiode
BX	Bunch Crossing
CRμ	Cosmic-Ray Muon
CSC	Cathode Strip Chamber
DIS	Deep Inelastic Scattering
DT	Drift Tube
ECAL	Electromagnetic Calorimeter
$\not\!\!E_T$	Missing Transverse Energy
HCAL	Hadronic Calorimeter
HF	Forward Calorimeter
HPD	Hybrid Photodiode
HV	High Voltage

Continued on next page

Table D.1 – continued from previous page

Acronym	Meaning
$\overline{MS}$	Modified Minimal Subtraction Scheme
λ	Nuclear Interaction Length
LO	Leading Order in pertubation calculations
NLO	Next to Leading Order
NNLO	Next to Next Leading Order
PDFs	Parton Distribution Functions
PMT	Photo-Multiplier Tube
RPC	Resitive Plate Chamber
SM	Standard Model or Super Module
VFE	Very Front End
VPT	vacuum phototriode